

# **Experiments on Nonlinear Waves in Homogeneous Flows With Free Upper Surface and Time-Dependent Forcing**

Von der Fakultät für Maschinenbau, Elektro- und Energiesysteme  
der Brandenburgischen Technischen Universität Cottbus-Senftenberg  
zur Erlangung des akademischen Grades eines  
Doktors der Ingenieurwissenschaften

genehmigte Dissertation

vorgelegt von

Diplom-Ingenieur (Dipl. -Ing.)

**Wenchao Xu**

geboren am 10.01.1989 in Shandong (China)

Vorsitzender: Prof. Dr.-Ing. Christoph Egbers (BTU C-S)

Gutachter: Prof. Dr. rer. nat. Uwe Harlander (BTU C-S)

Gutachter: Prof. Dr. rer. nat. Michael Bestehorn (BTU C-S)

Gutachter: Directeur de recherche Dr. Patrice Meunier (IRPHE, CNRS)

Tag der mündlichen Prüfung: 16.11.2020



## Abstract

The linear-theory assumption is a fundamental approach for the study of waves in fluids. The governing equations are linearized by assuming the perturbations are small so that the consequences of nonlinear terms are negligible. Nevertheless, if a wave approaches a critical level, in which the wave amplitude grows so as to create an instability of the background flow, the assumption of linearity may not hold any longer. In this case, the nonlinear terms are required to be taken into consideration.

In this thesis, two experimental setups have been proposed for the study of two scenarios, in which the nonlinear effects become significant and a traditional linear solution is no longer valid.

The first experiment focuses on an inertially oscillating rotating fluid. Rotating fluids frequently show nonlinear wave interactions and turbulence, particularly for non-uniformly rotating systems. One example of such a non-uniform rotating object is the Earth. Due to its fast rotation, it is not exactly spherical. As a result of the interaction with the Sun and Moon, the non-spherical Earth cannot rotate uniformly but shows precession and libration. This has consequences for the fluid enclosed in the outer Earth core. Due to the forcing, it might become turbulent, which is one of the key factors in the present theories explaining the generation of the geomagnetic field.

In the thesis, we present experimental results from a system that is simpler than classical precession experiments but still shows very similar wave interactions and a collapse to turbulence. This system consists of a partly filled rotating annulus that rotates about its symmetry axis slightly tilted with respect to the gravity vector and allows us to explore the Ekman numbers ranging from  $7.9 \times 10^{-6}$  to  $3.2 \times 10^{-5}$ .

In analogy to the more classical precession experiments, we also find a resonant collapse when the forcing frequency corresponds with a resonant frequency of the rotating tank. Two types of instability can be triggered: a parametric triadic instability, in which two free Kelvin modes arise and form a triad with the forced Kelvin mode, and a shear-type instability related to the nonlinearly excited geostrophic flow. The latter instability gives rise to a barotropic mode that interacts with the forced mode and generates secondary modes. We also observed dependency of the mode frequencies on the Ekman number, which can, at least partly, be explained by a Doppler shift due to the mean flow. Finally, we try to connect our data to a low-order dynamical system based on the weakly nonlinear

theory that describes the main features of single triad interaction in precession experiments. Although this model is originally not designed for the multiple triads we observe, it is still useful for a qualitative understanding of mode interactions, e.g. for the mechanism of geostrophic mode excitation.

The second experiment concerns the study of undular bores (or tidal bores). Tidal bores are hydraulic jumps caused by an incoming tidal propagating upstream in the estuarine zone of a river or a narrow bay against the direction of current in the river or the bay. Due to the periodic occurrence, tidal bores have significant impacts on the development of the riverbank, the transport of the sediments and the fishery in the river estuary. The nonlinearity plays an important role in undular bores. The free-surface nonlinearity increases the surface level at the propagating wave crests, thus leads to a greater velocity of propagation in the bore than in the undisturbed fluid. The nonlinearity also results in a steeper wavefront compared to linear theory and concentrates the undulating waves near the front of the bore.

An experiment has been performed in which undular bores are produced in an open circular channel. More specifically, two different cases have been investigated: a single bore case with a rigid boundary setup and a bore colliding case with a periodic lateral boundary setup. Bores are generated by abruptly releasing a barrier that separates fluids with different surface levels. Up to our knowledge, this is the first experimental study of undular bores in a circular channel. For a setup without barriers, this geometry accomplishes in a natural way the periodic lateral boundary conditions, which is very often used in numerical simulations. The experimental results have been compared with the nonlinear numeric simulations and achieved an excellent agreement.



---

## Zusammenfassung

Die Annahme der linearen Theorie ist ein grundlegender Ansatz für die Untersuchung von Wellen in Flüssigkeiten. Die herrschenden Gleichungen werden linearisiert, indem angenommen wird, dass die Störungen klein sind, so dass die Auswirkungen der nichtlinearen Terme vernachlässigbar sind. Wenn sich jedoch eine Welle einem kritischen Niveau nähert, bei dem die Wellenamplitude so zunimmt, dass eine Instabilität der Hintergrundströmung entsteht, kann die Annahme der Linearität möglicherweise nicht mehr zutreffen. In diesem Fall müssen die nichtlinearen Terme berücksichtigt werden.

In dieser Arbeit wurden zwei experimentelle Einrichtungen für die Untersuchung von zwei Szenarien betrachtet, in denen die nichtlinearen Effekte erheblich werden und eine traditionelle lineare Lösung nicht mehr gültig ist.

Das erste Experiment konzentriert sich auf ein trägheitsschwingendes rotierendes Fluid. Rotierende Fluide zeigen häufig nichtlineare Wellenwechselwirkungen und Turbulenzen, insbesondere bei ungleichförmig rotierenden Systemen. Ein Beispiel für ein solches ungleichförmig rotierendes Objekt ist die Erde. Aufgrund ihrer schnellen Rotation ist sie nicht exakt kugelförmig. Infolge der Wechselwirkung mit Sonne und Mond kann sich die nicht kugelförmige Erde nicht gleichförmig drehen, sondern weist Präzession und Libration auf. Dies hat Auswirkungen auf die im äußeren Erdkern eingeschlossene Flüssigkeit und die Flüssigkeit kann turbulent werden. Das ist einer der Schlüsselfaktoren in den gegenwärtigen Theorien zur Erklärung der Erzeugung des geomagnetischen Feldes ist.

In der Dissertation stellen wir experimentelle Ergebnisse aus einem System vor, das einfacher ist als klassische Präzessionsexperimente, aber dennoch sehr ähnliche Wellenwechselwirkungen und auch den Übergang zu Turbulenz zeigt. Dieses System besteht aus einem teilweise gefüllten rotierenden Ring, der sich um seine Symmetrieachse leicht geneigt gegenüber dem Gravitationsvektor dreht. Das Experiment ermöglicht es, die Ekman-Zahl im Bereich von  $7,9 \times 10^{-6}$  bis  $3,2 \times 10^{-5}$  zu untersuchen.

In Analogie zu den klassischen Präzessionsexperimenten finden wir auch einen Resonanzkollaps, wenn die erzwungene Frequenz mit einer Resonanzfrequenz des rotierenden Tanks übereinstimmt. Zwei Arten der Instabilität können ausgelöst werden: eine parametrische triadische Instabilität, bei der zwei freie Kelvinmoden entstehen und mit der erzwungenen Kelvin-Mode eine Triade bilden, und eine Scherungsinstabilität, die mit dem nichtlinear angeregten geostrophischen Fluss zusammenhängt. Die letztere Instabilität führt zu einer barotropen

Schwingungsmode, die mit der direkt angetriebenen Schwingungsmode interagiert und dadurch sekundäre Moden erzeugt. Wir beobachteten auch eine Abhängigkeit der Modenfrequenzen von der Ekman-Zahl, die zumindest teilweise durch eine Dopplerverschiebung aufgrund der mittleren Strömung erklärt werden kann. Schließlich versuchen wir, unsere Daten mit einem schwach nicht-linearen dynamischen System nachzubilden, das die Hauptcharakteristiken der Wechselwirkung einzelner Triaden in Präzessionsexperimenten beschreibt. Obwohl dieses Modell ursprünglich nicht für die von uns beobachteten mehrfachen Triaden ausgelegt ist, ist es dennoch hilfreich für ein qualitatives Verständnis der Modenwechselwirkungen, z.B. für den Mechanismus der Anregung der geostrophischen Mode.

Das zweite Experiment betrifft die Untersuchung von Gezeitenwellen (d.h. ein spezielles Soliton). Gezeitenwellen sind hydraulische Sprünge, die durch eine einströmende Gezeiten verursacht werden, die sich stromaufwärts in der Mündungszone eines Flusses oder einer engen Bucht entgegen der Strömungsrichtung im Fluss oder in der Bucht ausbreiten. Aufgrund des periodischen Auftretens haben Gezeitenwellen erhebliche Auswirkungen auf die Entwicklung des Flussufers, den Transport der Sedimente und die Fischerei im Flussmündungsgebiet. Bei der Gezeitenwellen spielt die Nichtlinearität eine wichtige Rolle. Die Nichtlinearität der freien Oberfläche erhöht das Oberflächenniveau an den sich ausbreitenden Wellenbergen und führt so zu einer größeren Ausbreitungsgeschwindigkeit in den nichtlinearen Gezeitwelle als in der ungestörten Flüssigkeit. Die Nichtlinearität führt auch zu einer steileren Wellenfront im Vergleich zur linearen Theorie und konzentriert die wellenförmigen Wellen in der Nähe der Vorderseite der Welle.

Es wurde ein Experiment durchgeführt, bei dem Gezeitenwellen in einem offenen kreisförmigen Kanal erzeugt werden. Insbesondere wurden zwei verschiedene Fälle untersucht: ein Einzelsoliton mit einer festen Randbedingung und ein Doppelsoliton mit Kollisionen und periodischen Randbedingungen. Gezeitwellen werden durch abruptes Herausziehen einer Barriere erzeugt, welche die Flüssigkeiten mit unterschiedlichen Oberflächenniveaus voneinander trennt. Nach unserem Kenntnisstand ist dies die erste experimentelle Untersuchung von Gezeitenwellen in einem kreisförmigen Kanal. Für einen Aufbau ohne Barrieren erfüllt diese Geometrie auf natürliche Weise die periodischen Randbedingungen, was sehr oft in numerischen Simulationen verwendet wird. Die experimentellen Ergebnisse wurden mit den nichtlinearen numerischen Simulationen verglichen und erzielten eine ausgezeichnete Übereinstimmung.

# Contents

<b>1</b>	<b>Introduction</b>	<b>1</b>
1.1	Motivation and Problem Statement . . . . .	1
1.2	About This Thesis . . . . .	3
<b>2</b>	<b>Theoretical Backgrounds</b>	<b>7</b>
2.1	Equations of Motion in Fluids . . . . .	7
2.2	Taylor-Proudman Theorem . . . . .	8
2.3	Plane Inertial Waves in Uniformly Rotating System . . . . .	9
2.3.1	Dispersion relation . . . . .	10
2.3.2	Phase and group velocity . . . . .	11
2.4	Inertial Modes in a Rotating Annulus . . . . .	13
2.5	The Ekman Layer . . . . .	16
2.6	Resonant Collapse . . . . .	20
2.7	Triadic Instabilities . . . . .	21
2.8	Instabilities Due to Differential Rotation . . . . .	22
<b>3</b>	<b>Experimental Setups</b>	<b>27</b>
3.1	The QBO-Wave Tank . . . . .	27
3.2	MSGWs Tank . . . . .	31
<b>4</b>	<b>Measurement Techniques</b>	<b>35</b>
4.1	Rheoscopic Flow Visualisation . . . . .	35
4.2	Particle Image Velocimetry . . . . .	36
4.2.1	Seeding . . . . .	37
4.2.2	Illumination . . . . .	37
4.2.3	Recording . . . . .	38
4.2.4	Calibration . . . . .	40
4.2.5	Evaluation and post-processing . . . . .	40
4.3	Ultrasonic Sensors . . . . .	44
<b>5</b>	<b>Methods of Data Analysis</b>	<b>47</b>
5.1	Discrete Fourier Transform . . . . .	47
5.2	Short Time Fourier Transform . . . . .	48
5.3	Harmonic Analysis . . . . .	49
5.4	Mode Reconstruction . . . . .	50
5.5	Bispectra Analysis . . . . .	52

<b>6</b>	<b>Instabilities in a Tilted Rotating Annulus</b>	<b>55</b>
6.1	Introduction . . . . .	55
6.2	Experimental Background . . . . .	57
6.3	Forced Kelvin Mode and Wave Breakdown . . . . .	59
6.4	The Geostrophic Mode . . . . .	66
6.4.1	Influence of the wind effect . . . . .	66
6.4.2	Influence of the inclination angle . . . . .	67
6.4.3	Influence of the filling depth . . . . .	69
6.5	Triadic Instability . . . . .	69
6.6	Shear Instability . . . . .	74
6.7	Doppler Shift . . . . .	80
6.8	Mode Amplitude . . . . .	82
6.9	Low-Order Amplitude Equation . . . . .	83
6.10	Discussion and Conclusion . . . . .	87
6.11	Outlook . . . . .	89
<b>7</b>	<b>Undular Bores in a Circular Channel</b>	<b>93</b>
7.1	Introduction . . . . .	93
7.2	Experimental Setups . . . . .	97
7.3	Experimental Results . . . . .	99
7.3.1	Single bore . . . . .	99
7.3.2	Colliding bores . . . . .	103
7.4	Comparisons Between Simulations and Experiments . . . . .	105
7.4.1	Introduction of the numerical model . . . . .	105
7.4.2	Single bore . . . . .	105
7.4.3	Colliding bores . . . . .	106
7.4.4	Influence of the centrifugal force . . . . .	109
7.5	Sloshing Shallow Water . . . . .	110
7.6	Conclusions and Outlook . . . . .	114
<b>8</b>	<b>Summary</b>	<b>117</b>

# List of Figures

2.1	Sketch of the trajectory of an inertially oscillating particle in a rotating fluid that restored by the Coriolis force. . . . .	9
2.2	Schematic sketches showing some properties of inertial waves with (a) low ( $\omega \ll 2\Omega$ ) and (b) high ( $\omega \rightarrow 2\Omega$ ) frequencies. The figures are reprinted from Messio <i>et al.</i> [86] . . . . .	13
2.3	A sketch showing the generation of the Ekman layer on the sea surface due to with wind stress, reprinted from Cushman-Roisin and Beckers [31]. . . . .	17
2.4	The structure of an Ekman layer induced by the wind stress on the surface, reprinted from Cushman-Roisin and Beckers [31]. . . . .	19
2.5	Bottom Ekman layer and Ekman pumping in an abruptly spinning up cylindrical container. . . . .	20
2.6	A sketch showing geometries of a partly filled and tilted rotating annulus. . . . .	23
3.1	Photographs showing the geometries of the QBO-wave tank and the different inner cylinders, reprinted from User Guide of the QBO tank. . . . .	28
3.2	Deviation of inner radius of the outer cylinder for different heights, reprinted from Seelig [104]. . . . .	28
3.3	LabVIEW <sup>®</sup> controlling interface of the QBO-wave tank. . . . .	30
3.4	A photograph of the QBO-wave tank mounted on a vibration absorbing optical table showing the mechanical components of the experimental apparatus. . . . .	31
3.5	Sketch of the mechanical structure of MSGWs tank. . . . .	33
3.6	Photograph of MSGWs tank showing the experimental setup with ultrasonic sensors over the outer ring. . . . .	33
3.7	Calibration of the oscillation frequency of MSGWs tank . . . . .	34
4.1	The schematic sketch and photography of the laboratory apparatus showing the installation of the measuring devices. . . . .	36
4.2	MediaLas <sup>®</sup> Compact line laser kit GREEN 75mW. . . . .	38
4.3	Back-bone modified GoPro Hero 7 Black. . . . .	39
4.4	PIV calibration with a checker board plate. . . . .	41
4.5	Inversed gray monochromic photo shows the displacement of the particles during a time interval $\Delta t = 0.3s$ . . . . .	41

4.6	Example of a discrete cross-correlation by applying a $4 \times 4$ sub-window on an $8 \times 8$ image sample, reprinted from Raffel [99]. . . .	42
4.7	Evaluating the same two images with different final interrogation window sizes: (a) $16 \times 16$ pixels and (b) $32 \times 32$ pixels. . . . .	43
4.8	Comparison of a vector field (a) directly from the evaluation and (b) filtered to remove outliers. . . . .	44
4.9	(a) Microsonic <sup>®</sup> mic+25/IU/TC ultrasonic sensor and (b) its detection zones from <a href="http://www.microsonic.de">www.microsonic.de</a> . . . . .	45
5.1	Removing high frequency noise of data from an ultrasonic sensor by FFT . . . . .	47
5.2	Azimuthal velocity field of frequency $\omega/\Omega = 1.165$ precessed by harmonic method from PIV result for $H = 24\text{cm}$ , $Ek = 1.19 \times 10^{-5}$ , $Fr = 0.09$ , $\alpha \approx 1^\circ$ . . . . .	50
5.3	The procedure for detecting the wavenumber in azimuthal direction using azimuthal velocity. . . . .	51
5.4	Symmetry regions of (a) third-order cumulants and (b) bispectra, reprinted from Nikias and Raghuvver [92]. . . . .	54
6.1	Sketch of the experiment that rotates with $\Omega$ about its axis of symmetry at angle $\alpha$ from the vertical. . . . .	59
6.2	(a) Amplitude spectrum of azimuthal velocity; (b) temporal evolution of amplitude of the forced mode $m_1$ and the geostrophic mode $m_0$ for $h = 1.2$ , $Ek = 2.38 \times 10^{-5}$ , $Fr = 0.02$ , $\alpha \approx 0.1^\circ$ , $z = 0.75h$ ; (c) reconstruction of the forced Kelvin mode based on the azimuthal velocity field from PIV measurement and (d) linear solution of the forced Kelvin mode. . . . .	60
6.3	Structure of the forced Kelvin mode showing by Kalliroscope, PIV measurement and linear solution of the radial velocity field in a vertical section. . . . .	61
6.4	A sequence of photographs of a vertical cross section in the annulus showing the process of the resonant collapse for $Ek = 1.19 \times 10^{-5}$ , $Fr = 0.09$ and water depth $h = 1.2$ . . . . .	62
6.5	Space-time diagrams for experiments with different $h$ and for $Ek = 1.19 \times 10^{-5}$ , $Fr = 0.09$ indicating the resonant collapse for $h = 1.2$ . . . . .	64
6.6	Amplitude of the forced Kelvin mode as a function of fluid depth $h$ for $Ek = 1.19 \times 10^{-5}$ , $Fr = 0.09$ , $\alpha \approx 1^\circ$ and measured at $z = 0.75h$ . . . . .	65
6.7	Light intensity measured in the middle of the gap at $z = 0.75h$ for $Ek = 1.19 \times 10^{-5}$ , $Fr = 0.09$ and $h = 1.2$ . . . . .	66

6.8	Illustration of time averaged non-dimensional azimuthal velocity measured over 200 revolutions at different heights. . . . .	67
6.9	Illustration of time averaged non-dimensional azimuthal velocity in radial direction. . . . .	68
6.10	Mean azimuthal flow profile as a function of radius for different fluid depth $h$ with $Ek = 1.19 \times 10^{-5}$ , $Fr = 0.09$ and measured at $z = 0.75h$ . . . . .	69
6.11	Amplitude spectrum for different Ekman numbers measured at $z = 0.75h$ with $\alpha = 0.1^\circ$ and $h = 1.2$ . Ek are respectively $2.39 \times 10^{-5}$ , $1.19 \times 10^{-5}$ and $7.96 \times 10^{-6}$ for 10, 20, 30 rpm. . . . .	70
6.12	Temporal evolution of amplitudes for $Ek = 1.19 \times 10^{-5}$ , $\alpha = 0.1^\circ$ and $h = 1.2$ . . . . .	71
6.13	Reconstruction of Kelvin modes based on the vorticity field for $h = 1.2$ , $Ek = 1.19 \times 10^{-5}$ , $Fr = 0.09$ , $\alpha \approx 0.1^\circ$ , $z = 0.75h$ . The colour represents the vorticity, where yellow (blue) indicates positive (negative) value of the vorticity. . . . .	71
6.14	Bicoherence spectrum for $\alpha \approx 0.1^\circ$ , $Ek = 1.19 \times 10^{-5}$ , $Fr = 0.09$ and $h = 1.2$ . . . . .	72
6.15	The dispersion relations showing the frequencies $\omega$ and the axial wavenumbers $k$ of two free Kelvin modes for azimuthal wavenumbers $m_9$ and $m_{10}$ . . . . .	73
6.16	Temporal evolution of amplitudes for $Ek = 1.59 \times 10^{-5}$ , $\alpha = 1^\circ$ and $h = 1.2$ . . . . .	74
6.17	Amplitude spectrum for $Ek = 1.19 \times 10^{-5}$ , $\alpha = 1^\circ$ , $h = 1.2$ and $z = 0.8h$ . . . . .	75
6.18	Reconstruction of wave modes based on the velocity field for $h = 1.2$ , $Ek = 1.19 \times 10^{-5}$ , $Fr = 0.09$ , $\alpha \approx 1^\circ$ , $z = 0.8h$ . . . . .	76
6.19	Bicoherence spectrum for $\alpha \approx 1^\circ$ with $Ek = 1.19 \times 10^{-5}$ , $Fr = 0.09$ and $h = 1.2$ . . . . .	76
6.20	Radial velocity field of modes with frequencies 0.159, 1.003 and 1.165 from PIV on a vertical plane for $h = 1.2$ , $Ek = 1.19 \times 10^{-5}$ , $Fr = 0.09$ , $\alpha \approx 1^\circ$ . . . . .	77
6.21	Amplitudes of modes (a) $A_0, A_1, A_3$ and (b) $A_{-2}, A_4$ as a function of Ek measured at different $z$ for $h = 1.2$ and $\alpha \approx 1^\circ$ . . . . .	78
6.22	Reconstruction of wave modes based on the velocity field for $h = 1.2$ , $Ek = 1.19 \times 10^{-5}$ , $Fr = 0.09$ , $\alpha \approx 1^\circ$ , $z = 0.75h$ . . . . .	79

6.23	Azimuthal mean flow profile for differential rotation with $Ek = 1.19 \times 10^{-5}$ , $Fr = 0.09$ and $h = 1.2$ . . . . .	79
6.24	Amplitude spectrum of differential rotation with $Ek = 1.19 \times 10^{-5}$ , $Fr = 0.09$ and $h = 1.2$ . . . . .	80
6.25	Non-dimensional kinetic energy spectrum at different angular velocity measured at $0.8h$ with $\alpha \approx 1^\circ$ . . . . .	81
6.26	Frequency distribution of the respective mode as a function of $Ek$ at $0.75h$ for $h = 1.2$ . (a) measured frequency; (b) frequency corrected by the Doppler effect. . . . .	81
6.27	The mode amplitude as a function of $Ek$ at $0.75h$ , $h = 1.2$ . . . . .	83
6.28	(a) Amplitude of the modes and (b) comparison between $A_0$ and $\chi(A_{10}^2 + A_{-9}^2)$ ( $\chi = 35$ ) as a function of the dimensionless time $t$ for $\alpha = 0.1^\circ$ . . . . .	84
6.29	Amplitude of the modes and ratios between $A_0$ and nonlinear effects of different modes as a function of the dimensionless time $t$ . . . . .	85
6.30	Theoretical prediction of the shear instability in the annulus for $Ek = 1.19 \times 10^{-5}$ and $Fr = 0.09$ . . . . .	88
6.31	(a) Photography of the extended slope bottom and (b) a sketch showing its geometry . . . . .	90
6.32	The first EOF component of light intensity of a $r$ - $z$ plan for (a) the normal annulus and (b) the annulus with the extended slope bottom. On the right hand side of (b) is a numerical ray-tracing result of the wave attractor. . . . .	91
7.1	A photography showing the tidal bore flows upstream on China's Qiantang River by Michael Greshko from National Geographic [48].	93
7.2	Plan view showing the collision of the tidal bore in Arcins channel on 19 October 2013, reprinted from Keevil <i>et al.</i> [58]. . . . .	94
7.3	Simulation results from Bestehorn and Tyvand [13] showing bore generation with different methods. . . . .	95
7.4	Sketch of the idealized model of bore generation by abruptly changing the height of fluids in two regions with different levels. . . . .	96
7.5	Position of ultrasonic sensors for different experimental setups. . . . .	98
7.6	Undular bores excited in the circular channel for two different heights and height level differences: (a) $h_0 = 5$ cm, $\Delta h/h_0 = 0.2$ (b) $h_0 = 16$ cm, $\Delta h/h_0 = 0.125$ . The value 0 on $y$ -axis represents the level of undisturbed water. . . . .	99



7.7	The propagation velocity $v_f$ , the wavelength $\lambda$ and the front height $H_f$ of undular bores as functions of the depth of the undisturbed water layer $h_0$ and difference of surface level $\Delta h$ before removing the barrier. . . . .	100
7.8	The streamwise velocity $u$ as a function of time measured at $h = 60$ mm for a single bore with $h_0 = 75$ mm, $\Delta h = 20$ mm compared with the surface profile of a single bore with $h_0 = 80$ mm, $\Delta h = 20$ mm. . . . .	102
7.9	Signals from the symmetrically positioned sensors S.4 and S.6 for $h_0 = 75$ mm, $\Delta h = 20$ mm verifying the symmetry condition of colliding bores. . . . .	103
7.10	Signals from the sensor S.3 showing the bores before and after the first (a) and third (b) collisions for $h_0 = 75$ mm, $\Delta h = 20$ mm. . . . .	104
7.11	Comparison of experiment and simulation for undular bore generation and reflection, reprinted from Borcia <i>et al.</i> [16]. . . . .	106
7.12	Comparison between experimental data (a) and numerical simulations (b) and (c) in the bore collision region for $h_0 = 75$ mm, $\Delta h = 24$ mm. . . . .	107
7.13	A Hovmöller diagram showing the surface profile of the first six bore collisions . . . . .	108
7.14	A Hovmöller diagram showing the streamwise velocity $u$ as a function of time for a single bore with $h_0 = 75$ mm, $\Delta h = 20$ mm. . . . .	110
7.15	Configuration of the oscillating experiment. . . . .	111
7.16	The response amplitude $h/h_0$ as a function of the forcing frequency $\omega/\omega_r$ . . . . .	113
7.17	The surface elevation as a function of time measured by sensor 3 for $\omega/\omega_r = 1.12$ and $\omega/\omega_r = 1.22$ . . . . .	114



## List of Tables

3.1	Parameters of the QBO tank and the fluid of the experiment. . . . .	29
3.2	Measurements of the accuracy of the cylinder angular velocity. . . . .	32
4.1	Specifications of hollow glass spheres. . . . .	38
4.2	Technical specifications of MediaLas <sup>®</sup> Compact line laser kit GREEN 75mW. . . . .	39
4.3	Technical specification of Microsonic <sup>®</sup> mic+25/IU/TC ultrasonic sensor. . . . .	46
6.1	The eigenfrequency of the inertial modes with azimuthal wavenum- ber $m = 1$ for $h = 1.2$ . . . . .	63
6.2	The eigenfrequency of the inertial modes with azimuthal wavenum- ber $m = 10$ and $-9$ for $h = 1.2$ . . . . .	73
6.3	The ratio of $A_0/\Sigma  A_{free} ^2$ for different Ek from experimental data measured at $0.8h$ and $A_0/\Sigma_{i=1}^2  A_{free} ^2$ from the model by Lagrange <i>et al.</i> [64]. . . . .	86
7.1	The maximal value of the centrifugal acceleration $a_{cf,max}$ and the surface elevation due to the centrifugal force during the bore prop- agation from numerical simulations. . . . .	110



---

# 1 Introduction

## 1.1 Motivation and Problem Statement

Wave motions in fluids are widely recognized as an essential part in the investigation of hydrodynamic stabilities and have important applications in the sciences of meteorology, oceanography and as well in engineering. The study of waves in fluids, more specifically in water, can be traced back to the early works by Sir Isaac Newton. In his Prop. XLV of Principia (1687), he deduced that the frequency of deep-water waves is proportional to the inverse of the square root of the wave length by proposing “a dubious analogy with oscillations in a U-tube” [30].

The most elementary wave theory is the small-amplitude or linear wave theory, where the governing equations are simplified by giving a reasonable approximation of wave characteristics for a wide range of wave parameters. In the late 18th century, Joseph-Louis Lagrange derived the linearized governing equations for small-amplitude waves and solved the equation for long plane waves in shallow water based on a shallow-water approximation. He found that “the speed of propagation of waves will be that which a heavy body would acquire in falling from ... half the height of the water in the canal” (Lagrange 1786), which means the velocity of the wave is proportional to  $(gh)^{1/2}$ , where  $g$  is gravitational acceleration and  $h$  the water depth [30]. The now-standard linear wave theory was first presented by Sir George Biddell Airy for surface gravity waves in his long article “Tides and Waves” for the Encyclopaedia Metropolitana in 1841 [3], [30].

The linear wave theory introduced by Airy is one of the simplest possible case and also the least complicated theory to study waves. The theory utilises a potential flow (or velocity potential) approach to describe the motion of surface gravity waves and is often applied in ocean engineering and coastal engineering to investigate the state of the sea, including shallow water waves, tides and tsunami waves as well as ship waves [45].

Moreover, Linear wave theory provides the approach to study any kind of waves such as acoustic waves, internal gravity waves and inertial waves. In linear theory, the governing equations are linearised by assuming the perturbations are small so that the consequences of nonlinear terms are negligible. One example of the application of the linear-theory assumption is given in section 2.3, where the dispersion relation of plane inertial waves is derived based on the linear theory.

Although the linear theory is only valid for non-breaking waves with small amplitude, it can still be useful and fundamental for understanding higher order

theories and for the analysis of irregular waves. Nevertheless, in a dynamical system, if a wave approaches a critical level, in which the wave amplitude grows so as to create an instability of the background flow, the assumption of linearity may not hold any longer. When dealing with problems of the onset of instabilities, the exponential growth rate of the amplitude of an unstable linear mode can be altered by the nonlinear interactions [36].

In a rotating fluid with the presence of an inertial oscillation forced by a single frequency, the mechanism of instabilities via a parametric triadic resonance has been extensively studied based on the linear theory [59]. Nevertheless, the nonlinear evolution of the instability is still an open question. The nonlinear effects are essential based on the fact that the nonlinear interaction of an inertial mode with itself in the Ekman layers leads to the generation of a geostrophic mode [63]. The geostrophic mode can slow down the solid body rotation and modify the mean flow profile in radial direction, which further influences the dispersion relation and might detune the frequency of the free Kelvin modes [52]. On the other hand, a sufficiently strong geostrophic mode can also interact with the present Kelvin modes, give rise to further modes and lead to instabilities [59], [110]. Nonlinear effects also determine the saturation of the amplitude of a resonant inertial mode together with the viscous damping [64].

For hydraulic jumps, i.e. bores, in an open channel, the nonlinearity has a significant influence as well. Due to the net increase of the surface level at the propagating wave crests, free-surface nonlinearity results in a greater velocity of propagation in the bore than in the undisturbed fluid. Compared to linear theory, nonlinearity leads to a steeper wave front and also concentrates the undulating waves near the bore front [13].

For a more realistic prediction of the development of instabilities as well as the investigation of wave motions in a more unstable regime, the nonlinear terms should be included. One important method for the study of the hydrodynamic instability problem is the weakly nonlinear theory, which is based on the linear theory by treating the leading nonlinear effects of small perturbations. With the origins in the 19<sup>th</sup> century, the weakly nonlinear theory has been intensively developed since 1960s [36]. For a precessing cylinder, a weakly nonlinear model was developed by Lagrange *et al.* [64] by taking into account the influence of a geostrophic mode. The weakly nonlinear model provided a good prediction of the transition from a steady saturated regime to an intermittent flow. Moreover, the model is able to estimate the mean flow inside the cylinder correctly even far from the threshold when the flow is turbulent.

Another approach for the investigation of the nonlinear waves is to describe the wave motions by fully nonlinear equations. However, the fully nonlinear wave equations are more complex for a mathematical analysis and there is no general analytical method to obtain a solution. Thus, each particular wave equation has to be treated individually. Closed-form solutions can be obtained by some advanced methods with a trial-and-error approach, which seeks possible solutions by deducing from the equation form and then attempts whether they satisfy the particular equation or not. Nevertheless, it is more common to solve the nonlinear equations with numerical techniques, such as finite difference, finite volume, finite element, spectral, least squares and many others [49].

Despite the rapid development of the numerical methods in the last decades, laboratory experiments are still reliable and effective to study the fundamentals of instabilities in a fluid where nonlinear effects are significant. The gained experimental data are able to provide a validation for the theoretical and numerical predictions from a weakly nonlinear model or a fully nonlinear numerical simulation.

In this thesis, results of laboratory experiments are presented with two different setups. A series of experiments are performed in a tilted rotating cylindrical annulus, which mimics the classical precession experiment for the study of the instabilities under a resonant condition induced by different mechanisms. The experimental result is connected with the weakly nonlinear model reported in Lagrange *et al.* [64]. The second part of experiments are conducted in a circular channel, in which a single undular bore or two identical and counter-propagating undular bores are generated for the study of bore propagation and collision with a periodic boundary condition. The experimental measurements are compared with the numerical simulation by Bestehorn and Tyvand [13].

## 1.2 About This Thesis

The main aim and object of the thesis are based on two publications (Xu and Harlander [118] and Borcia *et al.* [16]) with respect to the two different experimental setups. The thesis consists of eight chapters and is organized as follows.

Chapter 2 introduces the most relevant theoretical aspects. Fundamental equations of rotating flows including the dispersion relation for inertial waves in a rotating fluid are derived. Several theories that provide the fundamentals to understand experimental observations in the latter chapters, such as the Ekman layer, are presented. The chapter also introduces the concept of resonant collapse and

the two types of instabilities that contributes to the resonant collapse: a parametric triadic instability and a shear instability.

Chapter 3 describes in detail the two experimental setups, including the basic structures, the technical specifications, and the working principles. The calibration data are also presented, which ensure the experimental device running properly.

Chapter 4 depicts the measurement techniques as well as devices applied in both experiments. For the presented investigations, a rheoscopic fluid is used for a qualitative understanding of the rotating flow. The quantitative measurement is realized by particle image velocimetry, which provides the measurement of the velocity field on a 2D section, and ultrasonic sensors, which measures the surface profile by the distance from the sensor to the liquid surface.

Chapter 5 gives a brief introduction to the statistical methods that are used to analyse the experimental data. The Fourier transform and harmonic analysis are the two essential tools in post-processing the data, where the Fourier transform is used in detecting significant frequencies of the time series and the harmonic analysis is able to extract the amplitude and phase information of the known frequencies from the time series. The bispectra analysis enables the qualitative detection of nonlinear wave interactions regardless of lacking data in 3D space.

In chapter 6, the experimental observations of fluids in a tilted rotating annulus with a free surface are presented. This is a setup similar to the classical precessing cylinder experiment but with a simpler configuration. Due to the presence of the tilted rotating axis and the free surface, a Kelvin mode is forced with the same frequency as the rotation rate of the cylinder. For a certain depth, the amplitude of the forced Kelvin mode grows rapidly, breaks down and gives rise to further modes. The experimental result shows that the breakdown is related to two different types of instabilities: a shear-type instability related to the non-zero mean flow and a parametric instability related to the typical triadic resonance. Finally, the experimental results are compared with a low-order dynamic model for classical precessing cylinders.

Chapter 7 presents the investigation of the formation, propagation and collision of undular bores in a circular channel, which belongs to an experimental instrument previously developed for studying rotating baroclinic flows. According to our knowledge, this is the first experimental study of undular bores in a circular channel. For a setup without barriers, this geometry accomplishes in a natural way the periodic lateral boundary conditions, which have been very often used in numerical simulations. The experimental results are compared with



---

numerical simulations and achieved an excellent agreement, especially for the spatio-temporal structure of bores in the first few reflections or collisions. Moreover, a sloshing shallow water setup is carried out, in which the circular channel oscillates longitudinally with a fixed barrier. Hydraulic jumps or cnoidal waves can be generated depending on the excitation frequency.

The last section provides a discussion and summary of the presented work and is given in chapter 8 together with some suggestions of future works.



## 2 Theoretical Backgrounds

### 2.1 Equations of Motion in Fluids

To mathematically describe the motion of fluids, a standard beginning of the story is the Navier-Stokes momentum equation and the continuity equation. For an incompressible viscous flow of constant material properties without rotation, the classical form of the equations is

$$\frac{\partial \mathbf{u}}{\partial t} + (\mathbf{u} \cdot \nabla) \mathbf{u} = -\frac{1}{\rho} \nabla p + \mathbf{g} + \nu \nabla^2 \mathbf{u}, \quad (1)$$

$$\nabla \cdot \mathbf{u} = 0, \quad (2)$$

where  $\mathbf{u}$ ,  $t$ ,  $p$ ,  $\rho$ ,  $\nu$  and  $\mathbf{g}$  are respectively the flow velocity, time, the pressure, the density, the kinetic viscosity and the gravitational force. For the momentum equation (1), the terms on the left hand side are the inertial term, where the first and second term describe the time variation and the convection. On the right hand side are the internal source (pressure), the external source (gravity) and the diffusion term.

The main problem discussed in the thesis is based on a rotating frame, so that the Navier-Stokes equation with rotation becomes

$$\frac{\partial \mathbf{u}}{\partial t} + (\mathbf{u} \cdot \nabla) \mathbf{u} + \boldsymbol{\Omega} \times (\boldsymbol{\Omega} \times \mathbf{x}) = -\frac{1}{\rho} \nabla p + \mathbf{g} + 2\mathbf{u} \times \boldsymbol{\Omega} + \nu \nabla^2 \mathbf{u}, \quad (3)$$

where we have a new term on the each side of the equation representing two fictitious forces, i.e. the centrifugal force  $\boldsymbol{\Omega} \times (\boldsymbol{\Omega} \times \mathbf{x})$  and the Coriolis force  $2\mathbf{u} \times \boldsymbol{\Omega}$ . Since the centrifugal term is irrotational, there is

$$\boldsymbol{\Omega} \times (\boldsymbol{\Omega} \times \mathbf{x}) = -\nabla \left[ \frac{1}{2} (\boldsymbol{\Omega} \times \mathbf{x})^2 \right] = -\nabla \varphi_c, \quad (4)$$

where  $\varphi_c$  is a potential function of the centrifugal force.

In the usual case, the external field, i.e.  $\mathbf{g}$ , is conservative and there is  $\mathbf{g} = -\nabla \varphi_g$ , where  $\varphi_g$  is a potential term of gravity.

Replacing the centrifugal force term of (3) with (4) and sending it to the right hand side of (3), we will get the term  $-\nabla (p/\rho + \varphi_g - \varphi_c)$  on the right hand side. For a simplified expression, the term  $(p/\rho + \varphi_g - \varphi_c)$  is replaced by a single term  $p$ , which is referred as reduced pressure. Neglecting the viscosity, the equation of

motion (3) is thus simplified to

$$\frac{\partial \mathbf{u}}{\partial t} + (\mathbf{u} \cdot \nabla) \mathbf{u} = -\nabla p + 2\mathbf{u} \times \boldsymbol{\Omega}. \quad (5)$$

The term  $p$  in this equation, as well as the equations in following sections, is the reduced pressure. The equation (5) is known as the Euler equation.

## 2.2 Taylor-Proudman Theorem

In a rotating fluid, if  $L$  is a typical scale of the motion and  $U$  is the characteristic velocity, the ratio of the inertial force to the Coriolis force is given by the dimensionless number: the Rossby number ( $\text{Ro}$ ), which is defined as  $\text{Ro} = \frac{U}{fL}$ , where  $f = 2\Omega \sin(\phi)$  is the Coriolis frequency with  $\Omega$  being the angular frequency of a planetary rotation and  $\phi$  the latitude. In a rotating cylinder, the Coriolis frequency  $f = 2\Omega$  and the Rossby number is simply  $\text{Ro} = \frac{U}{2\Omega L}$ .

Considering the inviscid fluid in a rapidly and uniformly rotating system with constant angular velocity  $\boldsymbol{\Omega}$  so that  $\text{Ro} \ll 1$  and  $\partial \boldsymbol{\Omega} / \partial t = 0$ , the convection term  $(\mathbf{u} \cdot \nabla) \mathbf{u}$  is sufficiently smaller than the Coriolis force and the Euler equation (5) can be linearized as

$$\frac{\partial \mathbf{u}}{\partial t} = 2\mathbf{u} \times \boldsymbol{\Omega} - \nabla p. \quad (6)$$

Taking the curl of both side, we have

$$\frac{\partial(\nabla \times \mathbf{u})}{\partial t} = 2(\boldsymbol{\Omega} \cdot \nabla) \mathbf{u}, \quad (7)$$

If the flow is close to geostrophy, i.e. the fluid is in a steady-state and the pressure gradient force is balanced by the Coriolis effect, there is  $\partial(\nabla \times \mathbf{u}) / \partial t = 0$  and we obtain

$$(\boldsymbol{\Omega} \cdot \nabla) \mathbf{u} = 0, \quad (8)$$

which gives

$$\frac{\partial \mathbf{u}}{\partial z} = 0. \quad (9)$$

This equation states that in an inviscid, rapidly rotating and slowly varying fluid, the velocity components  $u, v, w$  cannot vary in the direction of  $\boldsymbol{\Omega}$ . This implies that if one velocity component is zero somewhere in the fluid layer it must be zero everywhere, hence the flow is 2D. This is called Taylor-Proudman theorem.

## 2.3 Plane Inertial Waves in Uniformly Rotating System

As a fictitious force, the Coriolis force cannot do work on the fluid ( $(2\mathbf{u} \times \boldsymbol{\Omega}) \cdot \mathbf{u} = 0$ ) but tends to deflect a particle in a direction perpendicular to its instantaneous velocity  $\mathbf{u}$ . This property in fact support the motion of inertial waves.

An inertial wave, which has been studied since developed in the late 19th century, is a type of wave in a rotating fluid with the Coriolis force being the restoring force [111]. Inertial waves exist commonly in geophysical fluid from the surface of a planet, such as flow in the oceans, to deep inside of a planet, e.g. flow in the Earth's liquid core. Moreover, inertial waves also play an important role in industrial problems, such as fuel tanks in a spinning rocket [105].

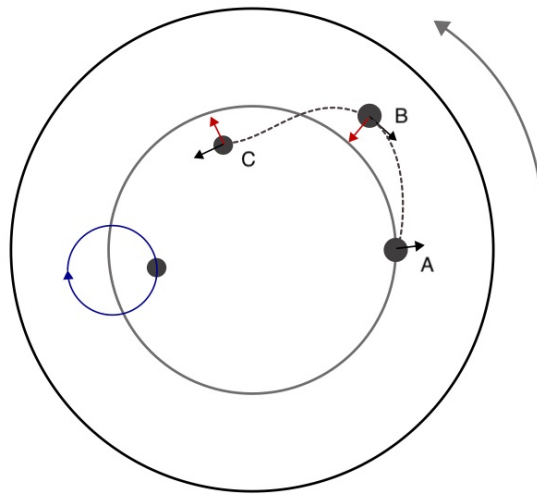


**Figure 2.1:** Sketch of the trajectory of an inertially oscillating particle in a rotating fluid that restored by the Coriolis force. The black arrows indicate the relative velocity in the rotating frame and the red arrows indicate the Coriolis force.

The mechanism of the inertial wave is illustrated in fig. 2.1, which shows the inertial oscillation of a particle in a counter-clockwise rotating fluid. The black arrows on the sketch indicate the relative velocity in the rotating frame and the red arrows indicate the Coriolis force. Given an initial velocity at position A by a perturbation, the fluid particle moves towards the outer circle of the rotating frame. Since the angular momentum of the fluid particle ( $rv$ ) is conserved, the fluid particle has a relatively lower azimuthal velocity compared to the rotating frame ( $r\Omega$ ) at position B, so that the particle is forced back towards the inner circle by the Coriolis force, i.e. moves towards its original rotating orbit. When the particle overshoots into the inner region, e.g. at position C in the sketch, the Coriolis force forces the particle in turn to the outer circle. This repeating process thus results in the trajectory of an inertially oscillating particle as the dashed curve on

fig. 2.1 in the non-rotating frame of reference. In the rotating frame of reference, on the other hand, the path of the particle is remarked the blue circle on fig. 2.1. When the initial perturbation is induced by periodic forcing, such as a librating body in the rotating fluid, steady inertial waves can be excited.

### 2.3.1 Dispersion relation

For a mathematical description of inertial waves, we assume an inviscid homogeneous fluid with uniform rotation ( $(\partial\boldsymbol{\Omega}/\partial t) \times \mathbf{r} = 0$ ). The fluid motion is assumed to be slightly departed from the rigid body rotation so that the nonlinear term  $(\mathbf{u} \cdot \nabla)\mathbf{u}$  in the Euler equation (5) can be neglected. Thus we have the momentum and the conservation equation with respect to the rotating reference frame:

$$\frac{\partial \mathbf{u}}{\partial t} + 2\boldsymbol{\Omega} \times \mathbf{u} = -\nabla p \quad (10)$$

$$\nabla \cdot \mathbf{u} = 0. \quad (11)$$

In a Cartesian coordinate system with the rotation axis being parallel to the  $z$ -direction, where  $\mathbf{u} = (u, v, w)^T$  and  $\boldsymbol{\Omega} = (0, 0, \Omega)^T$ , equation (10) and (11) can be written as

$$\begin{aligned} \frac{\partial u}{\partial t} - fv &= -\frac{\partial p}{\partial x}, \\ \frac{\partial v}{\partial t} + fu &= -\frac{\partial p}{\partial y}, \\ \frac{\partial w}{\partial t} &= -\frac{\partial p}{\partial z}, \\ \frac{\partial u}{\partial x} + \frac{\partial v}{\partial y} + \frac{\partial w}{\partial z} &= 0, \end{aligned} \quad (12)$$

where  $f = 2\Omega$ . This equation set is assumed to have wavelike solutions  $(u, v, w, p) = (u_0, v_0, w_0, p_0)e^{i(\mathbf{k} \cdot \mathbf{x} - \omega t)}$ , where  $\mathbf{k}$  is the wave vector with wavenumber components  $(k_x, k_y, k_z)$  in the  $(x, y, z)$  direction.

Introducing the solutions to (12), we get the expression of  $(u_0, v_0, w_0)$  as a function of  $p_0$ , that

$$\begin{aligned} u_0 &= p_0 \frac{\omega k_x + \mathbf{i}f k_y}{\omega^2 - f^2}, \\ v_0 &= p_0 \frac{\omega k_y - \mathbf{i}f k_x}{\omega^2 - f^2}, \\ w_0 &= p_0 \frac{k_z}{\omega}. \end{aligned} \quad (13)$$

Taking (13) into the conservation equation in (12), we finally get

$$\omega^2 = \frac{k_z^2}{k_x^2 + k_y^2 + k_z^2} f^2 = \frac{k_z^2}{k_x^2 + k_y^2 + k_z^2} (2\Omega)^2. \quad (14)$$

The equation can be further written as

$$\omega = \pm 2\Omega \cdot \frac{\mathbf{k}}{|\mathbf{k}|} = \pm 2\Omega \cos \theta, \quad (15)$$

where  $\mathbf{k} = (k_x, k_y, k_z)$  is the wave vector perpendicular to the wave phase and  $\theta$  is the angle of the wave vector with respect to the rotation axis. The equation (15) is the so-called dispersion relation that describes the dependency of the wave frequency on the wave vector/wavenumber. The dispersion relation implies that the frequency of inertial waves is always lower than the Coriolis frequency  $2\Omega$  and the magnitude of the frequency does not depend on the magnitude of the wave vector but on the propagating direction.

### 2.3.2 Phase and group velocity

The phase velocity  $\mathbf{c}_p$ , which describes the speed of a given phase of a wave travelling through space, is defined as

$$\begin{aligned} \mathbf{c}_p &= \frac{\omega}{|\mathbf{k}|} \frac{\mathbf{k}}{|\mathbf{k}|} = \pm 2\Omega \cos \theta \frac{\mathbf{k}}{|\mathbf{k}|^2}, \\ &= \left( \frac{2\Omega k_x k_z}{(k_x^2 + k_y^2 + k_z^2)^{3/2}}, \frac{2\Omega k_y k_z}{(k_x^2 + k_y^2 + k_z^2)^{3/2}}, \frac{2\Omega k_z^2}{(k_x^2 + k_y^2 + k_z^2)^{3/2}} \right). \end{aligned} \quad (16)$$

The equation indicates that inertial waves are dispersive and anisotropic, i.e. the phase velocity is dependent on the wave vector and its direction. The magnitude of the phase velocity is inversely proportional to the magnitude of the wave vector. Longer waves (waves with smaller wavenumbers) propagate faster and shorter waves propagate slower [47]. This is in contrast to the common non-dispersive waves, such as acoustic waves, in which the phase velocity depends only on the properties of the medium the waves pass through.

It is noted that the phase travels in the same direction of the wave vector, but  $\mathbf{c}_p$  does not equal a vector formed by phase speed components in three directions,

i.e.

$$\begin{aligned} (c_x, c_y, c_z) &= \left( \frac{\omega}{k_x}, \frac{\omega}{k_y}, \frac{\omega}{k_z} \right) \\ &= \left( \frac{2\Omega k_z}{k_x \sqrt{k_x^2 + k_y^2 + k_z^2}}, \frac{2\Omega k_z}{k_y \sqrt{k_x^2 + k_y^2 + k_z^2}}, \frac{2\Omega}{\sqrt{k_x^2 + k_y^2 + k_z^2}} \right) \neq \mathbf{c}_p. \end{aligned} \quad (17)$$

The group velocity  $\mathbf{c}_g$  describes the speed of the overall shape of a modulated wave and also represents the velocity of energy propagation. This is defined by  $\mathbf{c}_g = \nabla_{k\omega}(\mathbf{k}) = \left( \frac{\partial\omega}{\partial k_x}, \frac{\partial\omega}{\partial k_y}, \frac{\partial\omega}{\partial k_z} \right)$  [47]. For inertial waves, the group velocity yields

$$\begin{aligned} \mathbf{c}_g &= \frac{\Omega}{|\mathbf{k}|} - \mathbf{c}_p = \pm \frac{2}{|\mathbf{k}|^3} \mathbf{k} \times (\Omega \times \mathbf{k}) = \pm 2\Omega \sin \theta \frac{\mathbf{k}}{|\mathbf{k}|^2} \\ &= \left( \frac{-2\Omega k_x k_z}{(k_x^2 + k_y^2 + k_z^2)^{3/2}}, \frac{-2\Omega k_y k_z}{(k_x^2 + k_y^2 + k_z^2)^{3/2}}, \frac{2\Omega(k_x^2 + k_y^2)}{(k_x^2 + k_y^2 + k_z^2)^{3/2}} \right). \end{aligned} \quad (18)$$

Comparing to (16), the direction of the group velocity is perpendicular to the phase velocity, i.e. the energy of an inertial wave transports  $90^\circ$  with respect to the phase propagating direction.

Some properties of inertial waves are schematically shown in fig. 2.2. An inertial wave beam excited by an oscillating body travels in the direction with an angle of  $\theta_g = 90^\circ - \theta$  with respect to the rotating axis, whereas the phase propagates in the direction of the wave vector and perpendicular to the group velocity. The shear layers created by the inertial wave beam forms a double cone propagating upwards and downwards symmetrically from the source of the wave and only the upper half cone is plotted on fig. 2.2. The thick lines represent the conical surface formed by constant phase and the distance between two parallel lines denotes the thickness of the conical wavepacket. The conical surface of a constant phase travels with the phase velocity  $\mathbf{c}_p$  across the conical wavepacket from the outer boundary to the inner.

As is known from (15) to (18), the propagation of an inertial wave is depending on its frequency. For a low-frequency inertial wave, the shear layers form a sharp cone shape, whereas the cone is dull for high frequencies. Since the frequency of an inertial wave ranges between 0 and  $2\Omega$ , two limit cases should be considered.

For an inertial wave with the frequency much lower than the Coriolis frequency, i.e.  $\omega \ll 2\Omega$ ,  $\theta = \arccos(\omega/(2\Omega)) \rightarrow 90^\circ$  and  $\theta_g \rightarrow 0^\circ$  so that the inertial wave propagates energy almost parallel to the rotation axis and the phase propagate nearly horizontally, see fig. 2.2(a). In this case, the inertial waves are in fact Taylor columns since they have 2D structures invariant with respect to the rota-



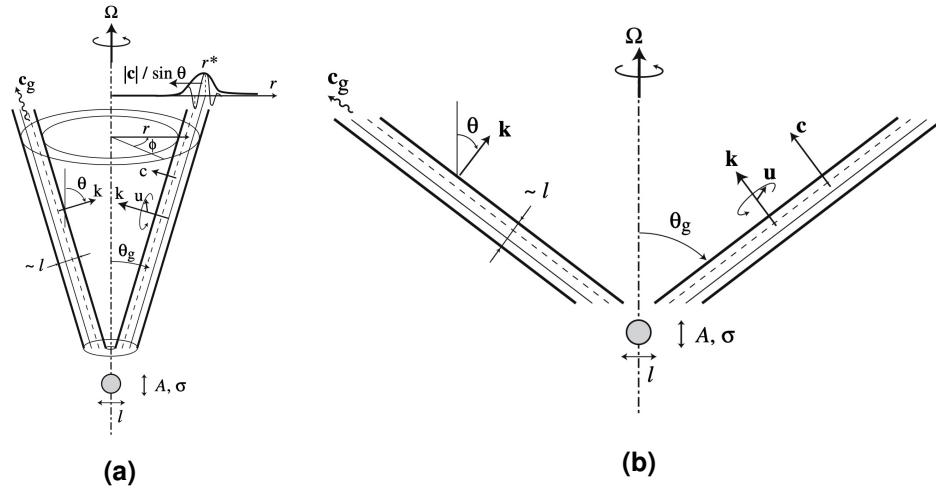


**Figure 2.2:** Schematic sketches showing some properties of inertial waves with (a) low ( $\omega \ll 2\Omega$ ) and (b) high ( $\omega \rightarrow 2\Omega$ ) frequencies. The figures are reprinted from Messio *et al.* [86]

tion axis. Such inertial waves, which are produced due to large scale geophysical motions, commonly exist in geophysical fluids.

For higher frequency inertial waves ( $\omega \rightarrow 2\Omega$ ), there is  $\theta = \arccos(\omega/(2\Omega)) \rightarrow 0^\circ$  and  $\theta_g \rightarrow 90^\circ$ , the shear layers excited by the inertial wave becomes almost horizontal, as is depicted in fig. 2.2(b). In this case, the inertial wave propagates energy horizontally. An inertial wave with frequency  $\omega = 2\Omega$  does not exist, because the group velocity vanishes due to  $k_x = k_y = 0$  for  $\omega = 2\Omega$ .

## 2.4 Inertial Modes in a Rotating Annulus

Being trapped in a closed container, inertial waves can be restricted to a set of discrete possible frequencies, and the corresponding spatial patterns are called inertial modes or Kelvin modes. In this section, we follow here the papers by Borcia and Harlander [17] and Lin *et al.* [72], in which the dispersion relation of Kelvin modes in an annulus has been derived.

Assuming a rotating annulus with inner and outer radius  $R_i$  and  $R_o$ , it is typical to employ the radius  $R_o$  as the length scale, the rotation period  $\Omega^{-1}$  as the time scale, so that the typical velocity and pressure are expressed as  $U = \Omega R_o$  and  $P = \rho\Omega^2 R_o^2$ . The dimensional variables (marked by \*) in the system are then characterised by the following transformation:

$$t^* \rightarrow \Omega^{-1}t, \mathbf{r}^* \rightarrow R_o\mathbf{r}, \mathbf{u}^* \rightarrow (\Omega R_o)\mathbf{u}, p^* \rightarrow (\rho\Omega^2 R_o^2)p.$$

Then the linearised equation (10) becomes

$$\frac{\partial \mathbf{u}}{\partial t} + 2\hat{\mathbf{z}} \times \mathbf{u} = -\nabla p, \quad (19)$$

together with the mass conservation equation

$$\nabla \cdot \mathbf{u} = 0, \quad (20)$$

where  $\hat{\mathbf{z}}$  is the unit vector in a cylindrical coordinate  $(r, \theta, z)$ . The boundary condition is defined as

$$\hat{\mathbf{n}} \cdot \mathbf{u} = 0 \quad (21)$$

at the bounding surface  $\mathcal{S}$ , where  $\hat{\mathbf{n}}$  is the unit normal vector to the surface.

To solve equation (19) and (20), it is mathematically convenient to eliminate the velocity  $\mathbf{u}$  and express the problem as a function of the pressure  $p$ . For this purpose, we first assume that (19) has solutions in the form  $\mathbf{u}(\mathbf{r}, t) = \mathbf{u}(\mathbf{r})e^{i\omega t}$  and  $p(\mathbf{r}, t) = p(\mathbf{r})e^{i\omega t}$ , the equation is then transformed into

$$i\omega \mathbf{u}(\mathbf{r}) + 2\hat{\mathbf{z}} \times \mathbf{u}(\mathbf{r}) + \nabla p(\mathbf{r}) = 0. \quad (22)$$

Taking  $\hat{\mathbf{z}} \cdot (22)$  and  $\hat{\mathbf{z}} \times (22)$ , there is

$$i\omega \hat{\mathbf{z}} \cdot \mathbf{u}(\mathbf{r}) + \hat{\mathbf{z}} \cdot \nabla p(\mathbf{r}) = 0 \quad (23)$$

and

$$i\omega \hat{\mathbf{z}} \times \mathbf{u}(\mathbf{r}) + 2\hat{\mathbf{z}}(\hat{\mathbf{z}} \cdot \mathbf{u}(\mathbf{r})) - 2\mathbf{u}(\mathbf{r}) + \hat{\mathbf{z}} \times \nabla p(\mathbf{r}) = 0. \quad (24)$$

Combining (23) and (24), we have the expression of  $\hat{\mathbf{z}} \times \mathbf{u}(\mathbf{r})$ :

$$\hat{\mathbf{z}} \times \mathbf{u}(\mathbf{r}) = \frac{1}{\omega} \left[ -2i\mathbf{u}(\mathbf{r}) - \frac{2}{\omega} \hat{\mathbf{z}}(\hat{\mathbf{z}} \cdot \nabla p(\mathbf{r})) + i\hat{\mathbf{z}} \times \nabla p(\mathbf{r}) \right]. \quad (25)$$

Finally, we substitute (25) into the divergence of (22), which yields

$$2\nabla \cdot (\hat{\mathbf{z}} \times \mathbf{u}(\mathbf{r})) + \nabla^2 p(\mathbf{r}) = 0, \quad (26)$$

and get

$$\nabla^2 p(\mathbf{r}) - \frac{4}{\omega^2} (\hat{\mathbf{z}} \cdot \nabla)^2 p(\mathbf{r}) = 0. \quad (27)$$

This equation is known as the Poincaré equation. Solving the Poincaré equation gives a set of plane inertial waves. Using the same method, we can get  $\mathbf{u}(\mathbf{r})$  ex-

pressed as a function of  $p(\mathbf{r})$  by substituting (25) into (22) so that

$$\mathbf{u}(\mathbf{r}) = \frac{4\mathbf{i}}{\omega(4-\omega^2)} \left[ \hat{\mathbf{z}}(\hat{\mathbf{z}} \cdot \nabla p(\mathbf{r})) - \frac{\omega^2}{4} \nabla p(\mathbf{r}) - \mathbf{i} \frac{\omega}{2} \hat{\mathbf{z}} \times \nabla p(\mathbf{r}) \right]. \quad (28)$$

In a closed container, the boundary condition  $\hat{\mathbf{n}} \cdot \mathbf{u} = 0$  can be imposed in (28) and the equation is expressed in terms of the pressure  $p(\mathbf{r})$ :

$$(\hat{\mathbf{n}} \cdot \hat{\mathbf{z}})(\hat{\mathbf{z}} \cdot \nabla p(\mathbf{r})) - \frac{\omega^2}{4} \hat{\mathbf{n}} \cdot \nabla p(\mathbf{r}) - \mathbf{i} \frac{\omega}{2} (\hat{\mathbf{n}} \times \hat{\mathbf{z}}) \cdot \nabla p(\mathbf{r}) = 0. \quad (29)$$

Assuming  $p \sim e^{i(m\theta + k\pi z/h)}$ , in a cylindrical annulus, the Poincaré equation (27) is supposed to have the general solution

$$p(r, z, \theta) = [C_{mk}^1 J_m(\xi r) + C_{mk}^2 Y_m(\xi r)] \cos\left(\frac{k\pi z}{h}\right) e^{im\theta}, \quad m = 0, 1, 2, \dots, k = 1, 2, 3, \dots, \quad (30)$$

where  $C_{mk}^1, C_{mk}^2$  are constants and  $J_m, Y_m$  are the first and second kind of Bessel function for integer order  $m$ .  $m$  and  $k$  indicate the azimuthal and vertical wave number.  $\xi$  is radial wave number determined from the boundary conditions.

To satisfy the boundary condition in radial direction at the inner and outer wall of the annulus, according to (29) there is  $\omega \frac{\partial p}{\partial r} - \mathbf{i} \frac{2}{r} \frac{\partial p}{\partial \theta} = 0$  for  $r = r_i$  and 1, where  $r_i$  is the nondimensional radius at the bound of the inner cylinder. So that for the solution there is

$$\begin{aligned} [\omega \xi J'_m(\xi) + 2m J_m(\xi)] C_{mk}^1 + [\omega \xi Y'_m(\xi) + 2m Y_m(\xi)] C_{mk}^2 &= 0, \\ [r_i \omega \xi J'_m(r_i \xi) + 2m J_m(r_i \xi)] C_{mk}^1 + [r_i \omega \xi Y'_m(r_i \xi) + 2m Y_m(r_i \xi)] C_{mk}^2 &= 0. \end{aligned} \quad (31)$$

To ensure the equations have non-trivial solution, the constant  $C_{mk}^1$  and  $C_{mk}^2$  should not be equal to zero, therefore the determinant of (31) should be zero, i.e.

$$\begin{vmatrix} \omega \xi J'_m(\xi) + 2m J_m(\xi) & \omega \xi Y'_m(\xi) + 2m Y_m(\xi) \\ r_i \omega \xi J'_m(r_i \xi) + 2m J_m(r_i \xi) & r_i \omega \xi Y'_m(r_i \xi) + 2m Y_m(r_i \xi) \end{vmatrix} = 0 \quad (32)$$

With some algebra we have

$$r_i \xi^2 (P_{m+1} + P_{m-1}) - 2r_i \frac{\xi^2}{\omega} (P_{m+1} - P_{m-1}) + 2 \frac{4 - \omega^2}{\omega^2} m^2 P_m = 0, \quad (33)$$

where  $P_m = J_m(\xi) Y_m(r_i \xi) - J_m(r_i \xi) Y_m(\xi)$ . For each given mode with frequency  $\omega$ , integer azimuthal wavenumber  $m$  and axial wavenumber  $k$ , solving equation (33) gives a series of ascending sequenced positive solution  $\xi$  that  $0 < \xi_{m1k} <$

$\xi_{m2k} < \dots < \xi_{mnk} < \dots$ , where  $n$  is the  $n$ -th solution and also the wavenumber in radial direction.

To finally solve the eigenmode problem, the dispersion relation is required, which is obtained by substituting (30) into the Poincaré equation (27):

$$\omega_{mnk}^2 = \frac{4k^2\pi^2}{(\xi_{mnk}h)^2 + (k\pi)^2}. \quad (34)$$

Combing (33) and (34), we are able to solve the eigenfrequency of a given mode with wavenumber  $(m, n, k)$ .

Assuming positive wavenumbers, a positive  $\omega_{mnk}$  represents a retrograde mode and negative  $\omega_{mnk}$  a prograde mode. Imposing the pressure  $p$  given by (30) into (28), we are able to calculate the velocity components of the inertial modes as

$$\begin{aligned} \hat{\mathbf{r}} \cdot \hat{\mathbf{u}}_{mnk} = & -\mathbf{i} \left[ \omega_{mnk} \xi_{mnk} (C_{mnk}^1 J_{m-1}(\xi_{mnk}r) + C_{mnk}^2 Y_{m-1}(\xi_{mnk}r)) \right. \\ & \left. + \frac{m(2 - \omega_{mnk})}{r} (C_{mnk}^1 J_m(\xi_{mnk}r) + C_{mnk}^2 Y_m(\xi_{mnk}r)) \right] \\ & \times \left( \frac{1}{4 - \omega_{mnk}^2} \right) \cos(k\pi z/h) e^{\mathbf{i}m\theta}, \end{aligned} \quad (35)$$

$$\begin{aligned} \hat{\theta} \cdot \hat{\mathbf{u}}_{mnk} = & \left[ 2\xi_{mnk} (C_{mnk}^1 J_{m-1}(\xi_{mnk}r) + C_{mnk}^2 Y_{m-1}(\xi_{mnk}r)) \right. \\ & \left. + \frac{m(2 - \omega_{mnk})}{r} (C_{mnk}^1 J_m(\xi_{mnk}r) + C_{mnk}^2 Y_m(\xi_{mnk}r)) \right] \\ & \times \left( \frac{1}{4 - \omega_{mnk}^2} \right) \cos(k\pi z/h) e^{\mathbf{i}m\theta}, \end{aligned} \quad (36)$$

$$\hat{\mathbf{z}} \cdot \hat{\mathbf{u}}_{mnk} = \frac{-\mathbf{i}n\pi}{h\omega_{mnk}} [C_{mnk}^1 J_m(\xi_{mnk}r) + C_{mnk}^2 Y_m(\xi_{mnk}r)] \sin(k\pi z/h) e^{\mathbf{i}m\theta}. \quad (37)$$

## 2.5 The Ekman Layer

Ekman layers are boundary layers in which there is a balance between the viscous force and the Coriolis acceleration. An Ekman layer plays an essential role in geophysical fluid systems and occurs wherever there is horizontal frictional stress in a rotating fluid, such as in the ocean along the surface, where waters are subject to wind stress, or at the bottom of the sea, where the frictional stress works against the flow. The Ekman layer has been first examined in the doctoral thesis by Vagn Walfrid Ekman after Fridtjof Nansen had noticed during his cruises to northern

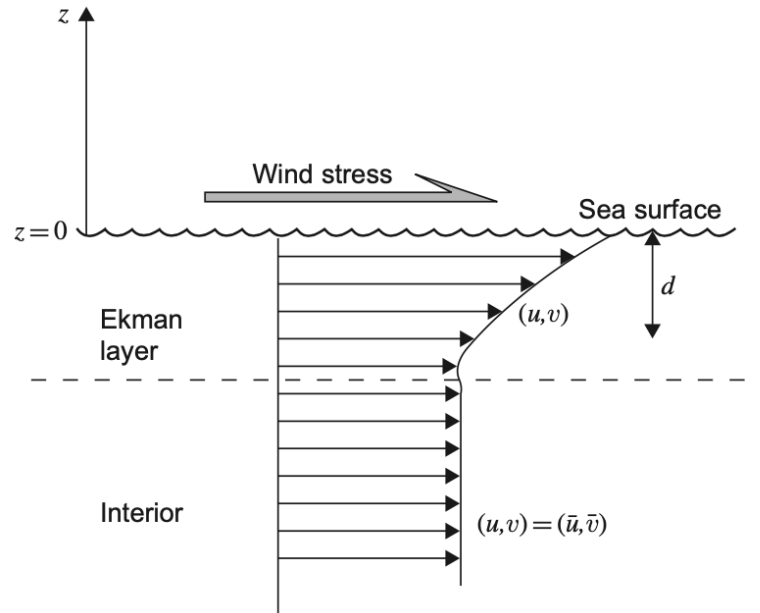


**Figure 2.3:** A sketch showing the generation of the Ekman layer on the sea surface due to with wind stress, reprinted from Cushman-Roisin and Beckers [31].

latitudes that icebergs drift not downwind but systematically at an angle of  $20^\circ$  -  $40^\circ$  to the right of the prevailing wind [31].

The mathematical description of an Ekman layer on the surface of the ocean induced by the wind stress, such as plotted in fig. 2.3, can be derived based on the following assumption: (1) steady conditions, (2) a homogeneous fluid and (3) a geostrophic interior with velocity  $(\bar{u}, \bar{v})$  subjected to the wind stress. Thus for the flow field  $(u, v)$  in the surface Ekman layer there is

$$-f(v - \bar{v}) = \nu_E \frac{\partial^2 u}{\partial z^2}, \quad (38)$$

$$+f(u - \bar{u}) = \nu_E \frac{\partial^2 v}{\partial z^2}, \quad (39)$$

with boundary conditions

$$\rho \nu_E \frac{\partial u}{\partial z} = \tau^x, \quad \rho \nu_E \frac{\partial v}{\partial z} = \tau^y \text{ at the surface } (z = 0), \quad (40)$$

$$u = \bar{u}, \quad v = \bar{v} \text{ in the interior } (z \rightarrow -\infty), \quad (41)$$

where  $\tau^x$  and  $\tau^y$  are wind stresses and  $\nu_E$  is the eddy viscosity. The eddy viscosity is a parameterized term adopted in the atmospheric and oceanic contexts

to analogy the momentum transference due to the near-random motion of small parcels of fluid in turbulent flows, which might be orders of magnitude larger than the momentum transference due to the molecular viscosity. In laboratorial context, on the other hand, a molecular viscosity is usually used for Ekman layer problems [113].

The solution of the equations is

$$u = \bar{u} + \frac{\sqrt{2}}{\rho_0 f d} e^{z/d} \left[ \tau^x \cos\left(\frac{z}{d} - \frac{\pi}{4}\right) - \tau^y \sin\left(\frac{z}{d} - \frac{\pi}{4}\right) \right], \quad (42)$$

$$v = \bar{v} + \frac{\sqrt{2}}{\rho_0 f d} e^{z/d} \left[ \tau^x \sin\left(\frac{z}{d} - \frac{\pi}{4}\right) + \tau^y \cos\left(\frac{z}{d} - \frac{\pi}{4}\right) \right], \quad (43)$$

where  $d$  is the Ekman layer thickness and  $d = \sqrt{\nu_E/\Omega} = E_\nu^{1/2} H$ .  $E_\nu^{1/2}$  is the eddy Ekman number defined as  $E_\nu = \nu_E/(\Omega H^2)$  and  $H$  is the depth scale of the motion (the total thickness if the fluid is homogeneous).

Obviously, the solution shows that the velocity departed from the interior flow is induced by the wind stress and does not depend on the interior flow. The magnitude of the departure decreases when the distance to the surface increases, meanwhile it is inversely proportional to the Ekman layer depth. For a flow with small viscosity, i.e. a thin Ekman layer, large drift velocities can be driven by the wind stress.

The wind-driven horizontal transport in the surface Ekman layer has components given by

$$\mathbf{U} = \int_{-\infty}^0 (u - \bar{u}) dz = \frac{1}{\rho_0 f} \tau^y, \quad (44)$$

$$\mathbf{V} = \int_{-\infty}^0 (v - \bar{v}) dz = \frac{-1}{\rho_0 f} \tau^x. \quad (45)$$

According to this result, the wind stress induces the horizontal transportation oriented perpendicular to the wind stress (fig. 2.4). Influenced by the Coriolis frequency, the transportation orients to the right in the northern hemisphere and to the left in the southern hemisphere. This fact explains the observation by Fridtjof Nansen that the icebergs drift to the right of the wind in the North Atlantic. To satisfy the mass conservation in the Ekman boundary layer, a vertical flux of fluid out of the boundary layer into the geostrophic region. This vertical

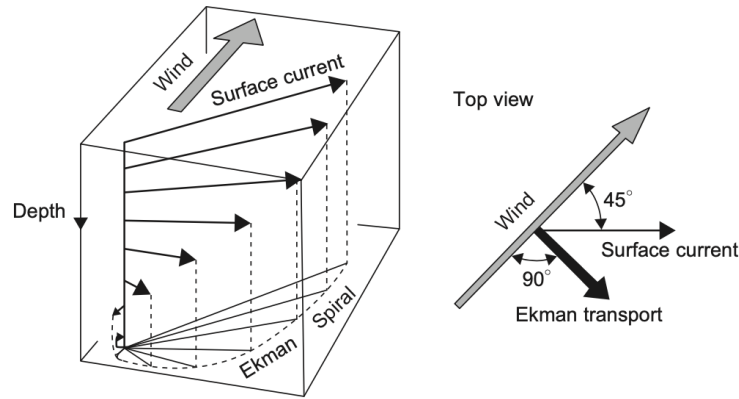


**Figure 2.4:** The structure of an Ekman layer induced by the wind stress on the surface, reprinted from Cushman-Roisin and Beckers [31].

velocity throughout the interior is given by

$$\begin{aligned}\bar{w} &= + \int_{-\infty}^0 \left( \frac{\partial u}{\partial x} + \frac{\partial v}{\partial y} \right) dz \\ &= \frac{1}{\rho_0} \left[ \frac{\partial}{\partial x} \left( \frac{\tau^y}{f} \right) - \frac{\partial}{\partial y} \left( \frac{\tau^x}{f} \right) \right],\end{aligned}\tag{46}$$

which is known as Ekman pumping or Ekman suction depending on the direction of the induced interior vertical velocity, where the Ekman pumping (suction) causes a downwelling (upwelling) interior flow perpendicular at the boundaries. Although the induced velocity is quite small comparing with the free stream velocities parallel to the boundary, it can largely influence geostrophic flows.

The Ekman layer and the closely related Ekman transport are very effective mechanisms in the ocean, by which winds drive subsurface ocean currents. In laboratory rotating spin-up experiments, Ekman pumping is the mechanism that accelerates the interior of the fluid to the rotation rate of the container. When a cylinder containing a fluid spins up abruptly from stationary or a solid-body rotation, see fig. 2.5, the fluid at the bottom forms an Ekman layer with the thickness of order  $O(\text{Ek}^{1/2})$  and moves with the cylinder while the bulk of the fluid remains unchanged. The fluid in the bottom Ekman layer is propelled radially outwards by the Coriolis force and leads to a secondary flow circulation along with the boundary layers and downward in the interior of the cylinder.

Besides the Ekman layer on the horizontal direction, a boundary layer in the vertical direction, which is known as the Stewartson layer, is established to satisfy the non-slip boundary condition on the vertical side-wall. The Stewartson layer has a double-layer structure, which consists of a thickness of order  $O(\text{Ek}^{1/4})$  to

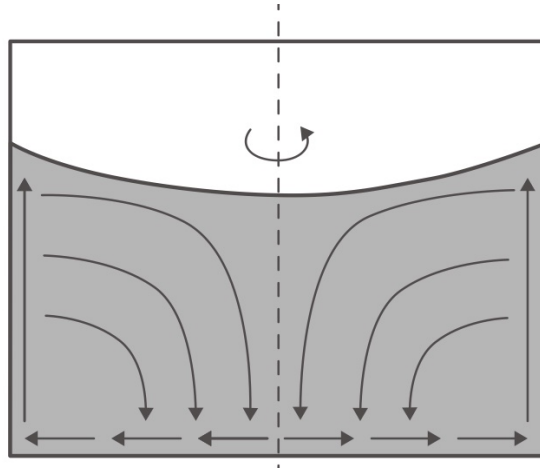


**Figure 2.5:** Bottom Ekman layer and Ekman pumping in an abruptly spinning up cylindrical container.

satisfy the non-slip condition for azimuthal flow and a thickness of order  $O(Ek^{1/3})$  for vertical flow [96]. In a nonlinear spin-up, the Stewartson layer might have considerable influences in the interior fluid motion [10].

## 2.6 Resonant Collapse

The rotating fluids with the presence of Kelvin modes become unstable for large Reynolds numbers. The Kelvin modes can be excited with different types of periodic forcing, such as precessional forcing (Lagrange *et al.* [63], [64], Manasseh [78] and Meunier *et al.* [88]), elliptical deformation (Le Bars *et al.* [68], Malkus [76] and Malkus and Waleffe [77]) and longitudinal libration (Borcia *et al.* [15], Busse [22] and Klein *et al.* [60]).

Using a slightly inclined paddle oscillating in a fully filled axially rotating cylinder to produce Kelvin modes with particular frequencies, McEwanc [84] first showed that a Kelvin mode can become resonant if its wavelength matches the height of the cylinder. He referred to the phenomenon as “resonant collapse” where the inertial mode breaks down and degenerates into a small scale disordered flow. The occurrence of the resonant collapse is predictable and quite consistent for the same forcing parameters.

Manasseh [78] performed a series of experiments with a fully filled precessing cylinder and explored the resonant collapse for widely varied parameters. With the use of visualisation techniques, he reported the presence of different breakdown regimes and categorized them with forcing frequencies, breakdown times and nutation angles. His observation shows that the resonant collapse is not at-



tributed to a single model.

In our experiment, we investigated the resonant collapse resulted from two kinds of instabilities: a parametric triadic instability and a shear-type instability.

## 2.7 Triadic Instabilities

In rotating flow, the low-amplitude periodic forcing plays as a conveyor that extracts energy from the background flow and transfers into motions of the fluid. Triadic resonance is a generic mechanism that increases the efficiency of this process [74]. In a typical scenario that a forced Kelvin mode has angular frequency  $\omega_f$ , azimuthal wavenumber  $m_f$  and axial wavenumber  $k_f$ , the two free mode components in a triadic resonance with the forced mode must satisfy

$$\begin{aligned} |\omega_1 \pm \omega_2| &= \omega_f, \\ |m_1 \pm m_2| &= m_f, \\ |k_1 \pm k_2| &= k_f. \end{aligned} \tag{47}$$

These conditions ensure that the Fourier component of mode 1 ( $\mathbf{u}_1, p_1$ ) is the same as the one of the nonlinear interaction between mode 2 ( $\mathbf{u}_2, p_2$ ) and the forced mode ( $\mathbf{u}_f, p_f$ ) [64]. The frequencies of the two free modes are able to be predicted by the dispersion relation based on linear inviscid theory. Although strict constraint on the radial wavenumbers is not necessary, two free modes with the same radial wavenumbers have much larger growth rates than different wavenumbers [37].

Triadic resonance gives rise to instabilities is a popular idea for elucidating the mechanism of the breakdown of laminar rotating flow with the presence of a resonant forcing. One year after McEwan reported his experimental observation of the resonant collapse in a rotating fluid with the presence of Kelvin waves in 1970, he proposed that the resonant collapse of the inertial modes is caused by nonlinear interactions of wave triads and experimentally confirmed by exciting internal gravity waves in a linearly stratified fluid [85].

A physical mechanism has been proposed by Kerswell [59] that a triadic resonance can be triggered by a given Kelvin mode with two other free Kelvin modes and leads to an instability. In this situation, the nonlinear terms of the disturbance can lock the free Kelvin modes and enable the transfer of the energy from the forced mode into the free modes. As suggested by Kerswell, the Kelvin modes arising from the triadic resonance are unstable and could lead to secondary insta-

bilities. This process might continue and eventually lead to a tertiary turbulence. Such a transition to a sustained chaotic flow has been presented numerically by Lopez and Marques [74].

## 2.8 Instabilities Due to Differential Rotation

In a rotating system, a stationary non-zero mean flow in azimuthal direction can be induced by forced oscillations in the fluid, such as precession, elliptical oscillation or rotation about an inclined rotating axis. The laminar azimuthal mean flow can become unstable with a sufficiently strong amplitude. This type of instability is usually related to two basic mechanisms.

One of the mechanisms is the famous Rayleigh's criterion for instability, which distinguishes between stable and unstable distributions of the angular velocity  $u_\theta = r\Omega(r)$  in an inviscid axisymmetric swirling flow. A flow is stable to all axisymmetric perturbations only if everywhere

$$\frac{d}{dr}(r^2 u_\theta^2) > 0. \quad (48)$$

Since the centrifugal force plays an essential role in creating or suppressing the instability, this type of instability is categorized as centrifugal instability. A typical example of the centrifugal instability is Taylor vortices in a circular Couette flow.

The second mechanism is shear-type instability that is related to the instability of parallel shear flow in a non-rotating system. In this case, the flow can be destabilized even if the Rayleigh's criterion is not violated. This instability was studied by Busse [21] in 1968. Later in 1970 Thompson [110] proposed the theoretical prediction of shear instabilities in a partly filled and tilted rotating cylinder and achieved a good agreement with laboratory experiments. Following Thompson's method, we derived the equation of shear instability bounds for annular geometry.

For an annulus with aspect ratio  $H/R$  and  $r_i = R_i/R_o$ , see fig. 2.6, the governing equations are given in (19) and (20) in Sec. 2.4. Due to the presence of the free surface and the inclination angle, different boundary conditions are defined as

$$\frac{\partial p}{\partial z} = 0 \quad \text{at} \quad z = 0, \quad (49)$$

$$\frac{\partial p}{\partial r} + \frac{2p}{r} = 0 \quad \text{at} \quad r = r_i \text{ or } 1, \quad (50)$$

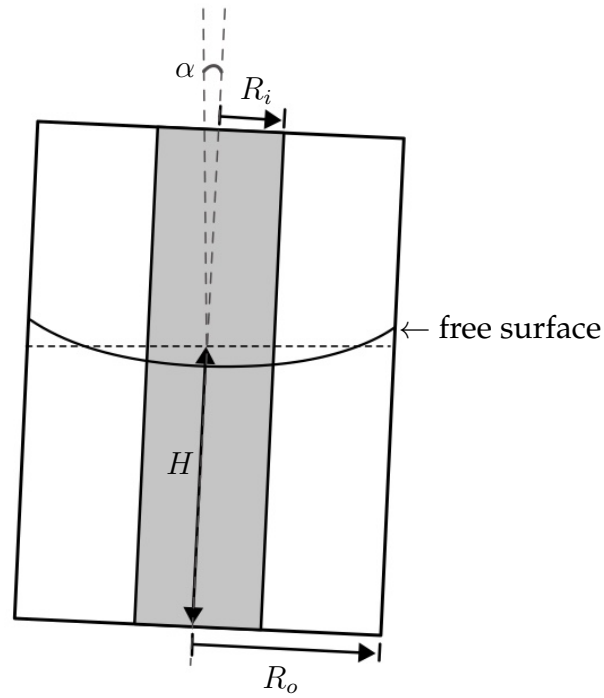


**Figure 2.6:** A sketch showing geometries of a partly filled and tilted rotating annulus.

$$\frac{\partial p}{\partial z} = \alpha r + \frac{p \text{Fr}}{3} - \frac{r \text{Fr}}{3} \frac{\partial p}{\partial r} \quad \text{at} \quad z = \frac{1}{4} \text{Fr} (2r^2 - 1) + H/R, \quad (51)$$

where  $\text{Fr} = \Omega^2 R/g$  is the Froude number that compares the centrifugal force to the gravitational force. The inviscid interior solution in the order of the forcing mode is given as

$$\frac{\partial^2 p}{\partial r^2} + \frac{1}{r} \frac{\partial p}{\partial r} - \frac{p}{r^2} - 3 \frac{\partial^2 p}{\partial z^2} = 0. \quad (52)$$

Using separation of variables, the solution of the (52) is of the form

$$p = \sum_{n=1}^{\infty} A_n \cos\left(\frac{\lambda_n z}{\sqrt{3}}\right) [C_1 J_1(\lambda_n r) + C_2 Y_1(\lambda_n r)]. \quad (53)$$

To fulfil the boundary condition (50), there is

$$r_i \lambda [C_1 J_1'(r_i \lambda) + C_2 Y_1'(r_i \lambda)] + 2 [C_1 J_1(r_i \lambda) + C_2 Y_1(r_i \lambda)] = 0, \quad (54)$$

$$\lambda [C_1 J_1'(\lambda) + C_2 Y_1'(\lambda)] + 2 [C_1 J_1(\lambda) + C_2 Y_1(\lambda)] = 0. \quad (55)$$

Similar to (31), nontrivial solutions require the determinant of the coefficient ma-

trix of  $C_1$  and  $C_2$  to be equal to zero, this gives

$$[r_i \lambda J_1'(r_i \lambda) + 2J_1(r_i \lambda)] [\lambda Y_1'(\lambda) + 2Y_1(\lambda)] = [\lambda J_1'(\lambda) + 2J_1(\lambda)] [r_i \lambda Y_1'(r_i \lambda) + 2Y_1(r_i \lambda)]. \quad (56)$$

Let  $\lambda_n (n \in N)$  be the solutions of this equation and  $C_1$  in (53) equal to one, the solution of  $p$  is

$$p = \sum_{n=1}^{\infty} A_n \cos\left(\frac{\lambda_n z}{\sqrt{3}}\right) \left[ J_1(\lambda_n r) - \frac{\lambda_n J_1'(\lambda_n) + 2J_1(\lambda_n)}{\lambda_n Y_1'(\lambda_n) + 2Y_1(\lambda_n)} Y_1(\lambda_n r) \right], \quad (57)$$

where the amplitudes  $A_n$  are still unknown. They can be determined via the surface boundary condition. For  $\text{Fr} \ll 1$ , the surface boundary condition (51) can be modified by using Taylor expansion in  $\text{Fr}$  so that

$$\frac{\partial p}{\partial z} + \frac{\text{Fr}}{4} (2r^2 - 1) \frac{\partial^2 p}{\partial z^2} = r + \frac{p \text{Fr}}{3} - \frac{1}{3} r \text{Fr} \frac{\partial p}{\partial r} + O(\text{Fr}^2) \quad \text{at} \quad z = H/R. \quad (58)$$

Taking (57) into (58) we get

$$\sum_{n=1}^{\infty} A_n \left[ -\frac{\lambda_n}{\sqrt{3}} B_n(r) \sin\left(\frac{\lambda_n H}{\sqrt{3} R}\right) - \frac{\text{Fr}}{12} (2r^2 - 1) \lambda_n^2 B_n(r) \cos\left(\frac{\lambda_n H}{\sqrt{3} R}\right) - \frac{\text{Fr}}{3} B_n(r) \cos\left(\frac{\lambda_n H}{\sqrt{3} R}\right) + \frac{1}{3} r \text{Fr} \frac{\partial B_n(r)}{\partial r} \cos\left(\frac{\lambda_n H}{\sqrt{3} R}\right) \right] = r, \quad (59)$$

where

$$B_n(r) = J_1(\lambda_n r) - \frac{\lambda_n J_1'(\lambda_n) + 2J_1(\lambda_n)}{\lambda_n Y_1'(\lambda_n) + 2Y_1(\lambda_n)} Y_1(\lambda_n r). \quad (60)$$

Multiplying each side by  $r B_n(r)$  to make the error of the surface boundary condition orthogonal to the function  $B_n(r)$  in radial direction and integrating from the inner boundary  $r = r_i$  to the outer boundary  $r = 1$ , we get the linear system that determines the unknown  $A_n$ . This linear system can be numerically solved as a function of  $\text{Fr}$ ,  $S_n$ ,  $C_n$ , where  $S_n = \sin\left(\frac{\lambda_n H}{\sqrt{3} R}\right)$ ,  $C_n = \cos\left(\frac{\lambda_n H}{\sqrt{3} R}\right)$ . For the given  $r_i$ , the solution of the first resonance is

$$A_1 = \frac{0.298}{S_1 + 0.387 \text{Fr} C_1}, \quad (61)$$

so that the first resonant depth is then

$$H/R = 1.199 - 0.141 * \text{Fr}. \quad (62)$$

The maximum amplitude of the mean motion is limited by the zero-order bound-

ary solution. Although the viscosity is ignored in the interior for small Ekman number, the boundary layer should be considered as viscous.

The possible barotropic shear instability, according to Thompson [110], is relevant to the “Rayleigh” stability equation given by Busse [21]. The instability bound of the inclination  $\alpha$  is given as

$$\alpha = \left( \frac{3.41}{|V_0| m_n^* R} \right)^{\frac{1}{2}} \frac{\text{Ek}^{\frac{1}{4}}}{A_n}, \quad (63)$$

where  $|V_0|$  is the mean amplitude that we know experimentally and  $m_n^* = 2\pi/(R/n)$  is the dimensional wavenumber for the  $n$ -th resonance. Using the amplitude  $A_n$  from (61), the bounds of instabilities are able to be predicted.



### 3 Experimental Setups

The laboratory experiments presented in this thesis have been performed using two experimental apparatus. This chapter will give some details of the experimental setups.

#### 3.1 The QBO-Wave Tank

The QBO-wave tank, which is built in the years 2011/2012 at the Brandenburg University of Technology Cottbus - Senftenberg (BTU CS), is originally designed to study the mechanism of the quasi-biennial oscillation (QBO) of the zonal wind in the equatorial stratosphere with a variable period averaging 28 months.

The tank consists of two coaxial and independently rotating cylinders. As is shown in fig. 3.1, the container has an outer cylinder made of borosilicate glass with a radius  $R_o = 200$  mm and a replaceable inner cylinder of different geometries (see the right side of fig. 3.1) made of anodized aluminium. The optional inner cylinders include a normal straight cylinder with a radius  $R_i = 75$  mm and a frustum with the radius ranging from 100 mm at the bottom to 50 mm at the top, which is designed to capture features of a spherical shell. For the experiments discussed in the thesis, only the straight inner cylinder was employed. The height of the interior is 500 mm and thus the total volume of the interior is 54 Litres. The inner and outer cylinder are driven by two individual motors and therefore are able to rotate independently. Being attached with the outer cylinder, the anodized aluminium bottom rotates simultaneously with the outer cylinder. An acrylic glass transparent top plate constrained with the outer cylinder is available when a closed container is required. To reduce the reflection when using a laser device for measurement, the surfaces of the aluminium bodies, including the inner cylinder and the bottom plate, are painted in black. Meanwhile, the transparent outer cylinder and the top lid allow optical measurements from the side or above.

The roundness of the outer cylinder has been examined with a dial test indicator at three different heights, see fig. 3.2. Due to imperfections in production, out-of-roundness irregularities exist in the tank wall with a maximum magnitude of 1.8 mm, less than 1% of the inner radius of the outer cylinder. The out-of-roundness is worse close to the bottom.

Beside the independently regulated constant rotation rate of the two cylinders, the controlling system also allows the cylinders rotating with periodical oscilla-

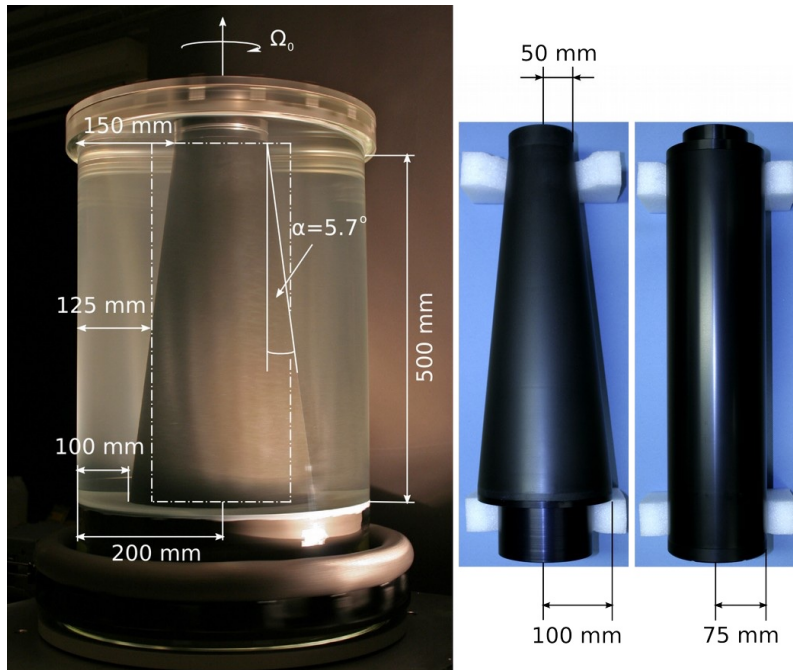


**Figure 3.1:** Photographs showing the geometries of the QBO-wave tank and the different inner cylinders, reprinted from User Guide of the QBO tank.

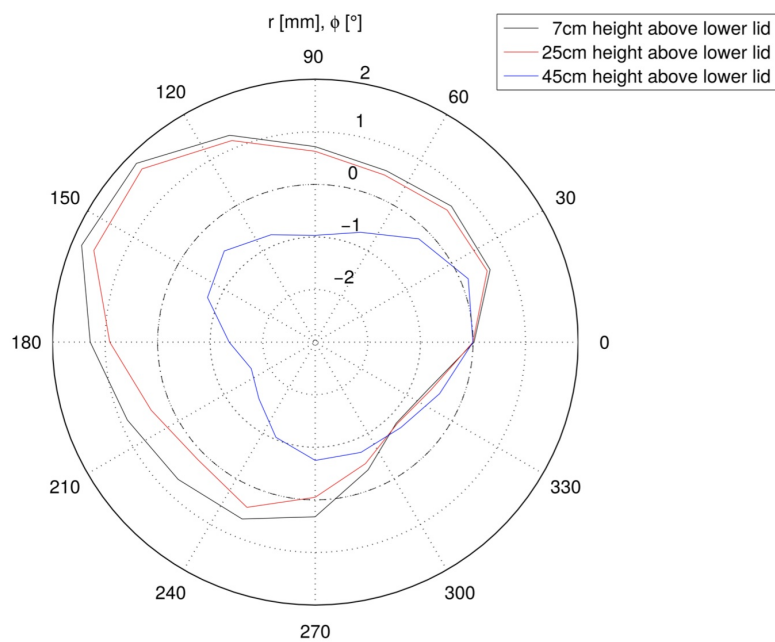


**Figure 3.2:** Deviation of inner radius of the outer cylinder for different heights, reprinted from Seelig [104].



**Table 3.1:** Parameters of the QBO tank and the fluid of the experiment.

<b>Geometrical parameters</b>			
inner cylinder radius	$R_i$	75	mm
outer cylinder radius	$R_o$	200	mm
gap width	$d$	125	mm
radius ratio	$a = R_i/R_o$	0.375	
maximum inner rotation rate	$\Omega_{i,max}$	50	rpm
maximum inner rotation rate	$\Omega_{i,max}$	50	rpm
Ekman number	$Ek = \frac{\nu}{\Omega_o R_o^2}$	$\geq 4.26 \times 10^{-6}$	
<b>Working fluid properties</b>			
working fluid		distilled water	
density (20°C)	$\rho$	998.2	$kg/m^3$
kinematic viscosity (20°C)	$\nu$	$1.004 \times 10^{-6}$	$m^2/s$

tions, so that the angular velocity of each cylinder can be configured as

$$\Omega_{in,out} = \Omega_0[1 + \epsilon \cdot \sin(\omega t)], \quad (64)$$

where  $\epsilon$  is the oscillation amplitude with  $0 < \epsilon < 0.49$  and  $\omega$  is the forcing frequency normalized by  $\Omega_0$ .

The motors that drive the cylinders are controlled by the software LabVIEW® and the user interface is shown in fig. 3.3 as an example. The driving signals for the motors are transferred to the controlling unit via an SCB-68 digital I/O interface device by National Instruments that converts the digital signal to a control voltage. Output signals from the I/O device will be inputted in the frequency inverters by Stöber Antriebstechnik GmbH that directly control the rotation rate of the two three-phase alternating current (AC) motors, which are also products from Stöber Antriebstechnik GmbH.

The entire experimental apparatus, including the cylinders, motors and transmission gears, is mounted on a vibration absorbing optical table. To reduce additional vibrations, the two motors are mounted on the table to the left and right side of the experiment cell and drive the cylinders via gear belts. Between the base plates and the motors, 5 mm robber gaskets are used to inhibit additional vibrations.

The motors together with bevel gears are surrounded with external tables and protective grids for safety reasons. The outer cylinder motor has the power of 2.2 kW, speed of 1455 rpm and a rated torque of 14.4 Nm and the inner cylinder motor with the power of 0.55 kW, speed of 1400 rpm and a rated torque of 3.8 Nm. Both motors are connected to a power transmission gear unit with a transmission

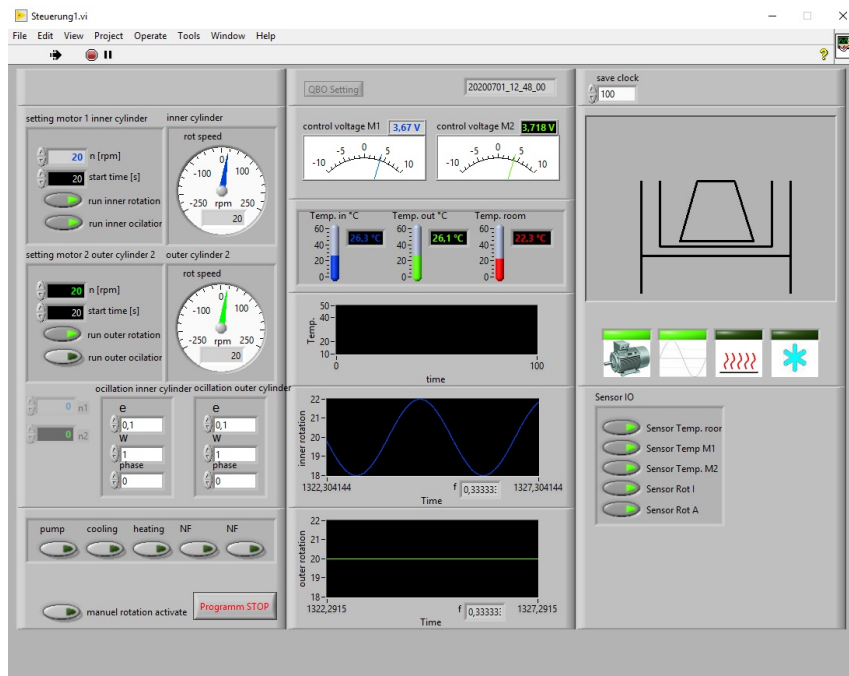


**Figure 3.3:** LabVIEW® controlling interface of the QBO-wave tank. The left block controls the rotation rate including azimuthal oscillations of the inner and outer cylinders. The middle and right blocks monitor the current status of the apparatus.

ratio of 3569 : 128 (outer) and 1261 : 50 (inner). With this setup, the transmission gears are able to provide highly accurate rotation rate for 5 – 50 rpm. For higher speeds ( $50 \text{ rpm} < \Omega < 150 \text{ rpm}$ ), optional transmission gears are also available with transmission ratios of 1520 : 273 and 43 : 8 for the outer and inner motors respectively.

The working status of the motors are monitored by additional temperature sensors (LM19-CIZ) from National Instruments to avoid an overheating of the motors during long-time experiments. The LM19-CIZ temperature sensor is a precision analog output complementary metal-oxide-semiconductor (CMOS) integrated-circuit temperature sensor that operates over a temperature range from  $-55^{\circ}\text{C}$  to  $+130^{\circ}\text{C}$  with a maximum error of  $\pm 3.8^{\circ}\text{C}$ , which is sufficient to monitor the working temperature of motors. The temperature sensors are also connected to the digital I/O interface and their measures are displayed on the LabVIEW® controlling interface (see fig. 3.3).

To ensure the cylinders rotating with accurate angular velocities, rotation rates of the inner and outer cylinder have been measured with a tachometer for clockwise rotation with different set-values from 5 to 45 rpm. For each set-value of the rotation rate, the measurement is repeated for 5 times by starting the rotation and then completely stopping. According to the result listed in tab.3.2, the rotation

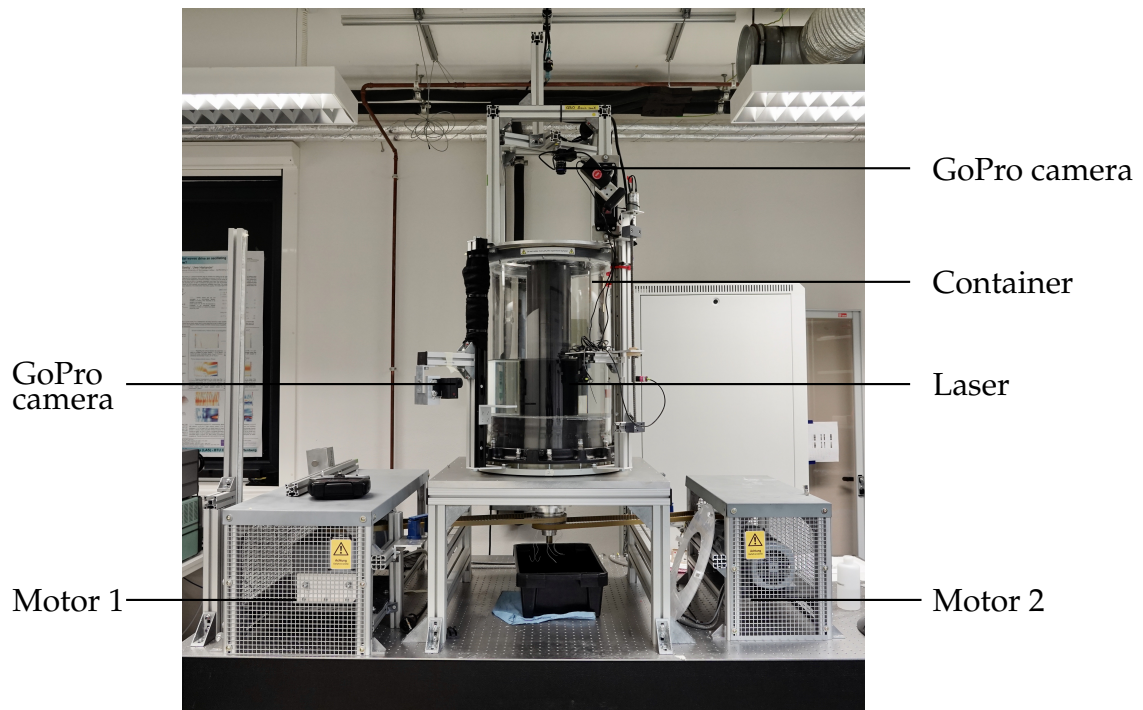


**Figure 3.4:** A photograph of the QBO-wave tank mounted on a vibration absorbing optical table showing the mechanical components of the experimental apparatus. Motor 1 drives the inner cylinder and motor 2 drives the outer.

rate of the outer cylinder is very precise with a maximum relative error of 0.40%. Repeating the test by completely restarting the rotation shows that the measured rotation rates are very consistent. The accuracy of the inner cylinder, although not as good as the outer cylinder, is still acceptable. For lower rotation rate the relative error is rather high, in particular at 10 rpm, where the relative error is as high as 1.5% and repeating the tests gives inconsistent measurements with a deviation of 0.11 rpm. However, for higher rotation rate the inner cylinder works more accurately.

### 3.2 MSGWs Tank

The Multi-Scale Gravity Waves (MSGWs) tank is an experimental apparatus built in 2016 at BTU CS and designed to investigate inertial gravity waves under a shallow water configuration, where the aspect ratio, i.e. the ratio between the depth and the radius, is smaller than one. This is a classical setup of a rotating experiment with its mechanical structure shown in fig. 3.5 and the main parts marked with numbers.

The whole apparatus is build on a metallic base (1), which supports a synchronous servomotor with a helical-bevel gear unit (2) and rotary index table (3).

**Table 3.2:** Measurements of the accuracy of the cylinder angular velocity.

Set value (rpm)	inner cylinder			outer cylinder		
	average (rpm)	relative error (%)	deviation (rpm)	average (rpm)	relative error (%)	deviation (rpm)
5	4.93	1.40	0.03	5.02	0.40	0.00
10	10.15	1.50	0.11	10.01	0.10	0.00
15	15.09	0.60	0.06	14.99	0.07	0.01
20	20.06	0.30	0.03	19.99	0.05	0.01
25	25.07	0.28	0.02	24.98	0.08	0.01
30	30.03	0.10	0.01	30.00	0	0.00
35	35.04	0.11	0.01	35.03	0.09	0.00
40	40.05	0.13	0.01	40.03	0.08	0.00
45	45.03	0.07	0.00	45.05	0.11	0.00

The motor (model CMPZ100S) and the helical-bevel gear unit (KAF57) are from SEW-EURODRIVE. The motor has a maximum speed of 3000 rpm and a two-stage gear system provides a high degree of efficiency of over 90% in both torque directions and at all input speeds. The rotary index table from AUTOROTOR Srl transmits the rotation of the inlet shaft to the rotation of an output disk positioned on top. The rotating disk directly connects to eight metallic arms (4), which is built to fix the tank (5) to the rotating disk. The tank consists of three concentric cylindrical gaps enclosed by four side walls made of acrylic glass. The material was chosen due to its high light transfer of 92% and low density of 1.19 g/cm<sup>3</sup> so that invasive measurement techniques such as PIV and infrared thermography are possible.

The tank is controlled with software provided by the motor's manufacturer SEW-EURODRIVE, which controls the tank rotating with a constant angular velocity as well as a ramp function that allows to set constant acceleration for spin-up/spin-down. Richer motion control is also available with the use of an additional digital I/O device from National Instruments and LabVIEW. The digital I/O device outputs voltage signals to the controlling unit of the motor to regulate the rotation rate of the motor, which allows the tank rotating with a time-dependent motion function, such as sinusoidal oscillation.

With the LabVIEW control system, the oscillation frequency has been calibrated with ultrasonic sensors. The sensors have been mounted on the oscillating platform and detected the distance to a surface which is stationary relative to the laboratory frame. As is shown in fig. 3.7, the tank oscillates slower than the set values, the relation between the real oscillation rate and the set rate follows  $\Omega_{real} = 0.962\Omega_{set}$ .

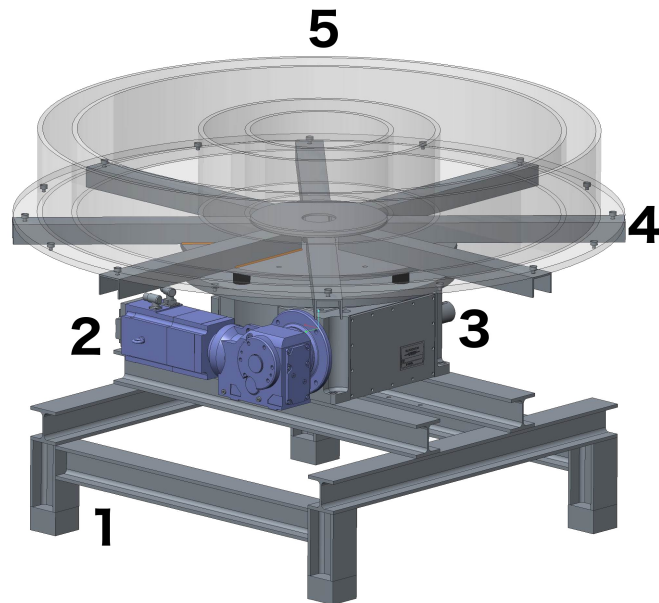


**Figure 3.5:** Sketch of the mechanical structure of MSGWs tank. The numbers on the sketch mark the main components of the tank and detailed descriptions are given in the text. The figure is reprinted from Rodda [100].

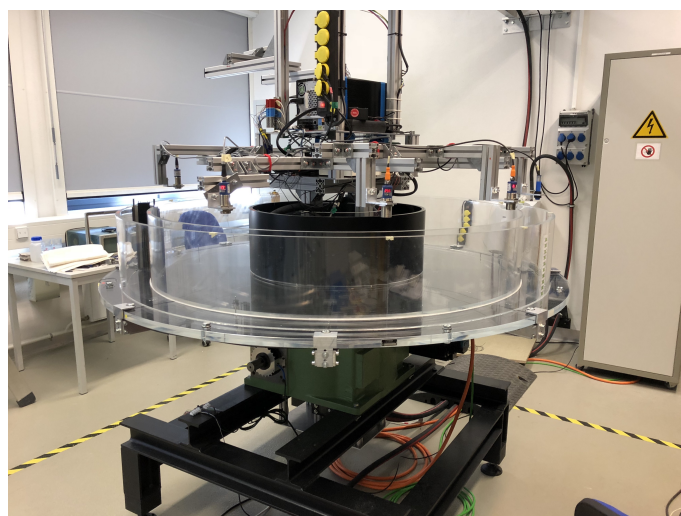


**Figure 3.6:** Photograph of MSGWs tank showing the experimental setup with ultrasonic sensors over the outer ring.

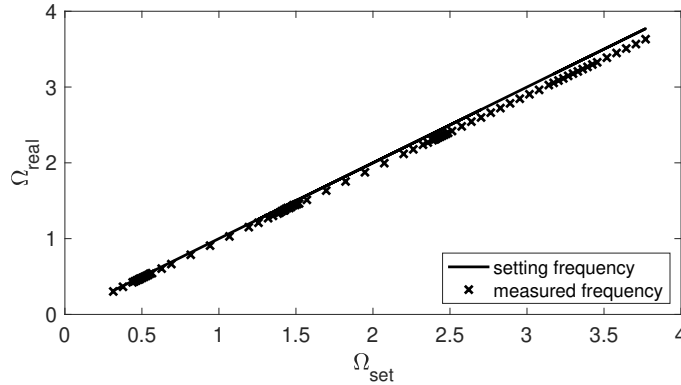


**Figure 3.7:** Calibration of the oscillation frequency of MSGWs tank, the line represents the nominal oscillation rate and the crosses represent the actual value.

To study inertial gravity waves, the three cylindrical channels are designed in a way that the middle channel is filled with working fluid meanwhile the inner and outer channels are filled with cold and warm water respectively to cooling down or heating up the working fluid in the middle channel. A number of auxiliary devices are required to ensure the functionality of MSGWs tank, such as a refrigerating device for cooling down the water in outer channel, a heating device for warming up the water in the inner channel as well as two pumps for the cooling/heating circulations in both channels. The tank is designed and built with a rather large size, the four circular walls that compose the three channels have the radius 815 mm, 700 mm, 350 mm and 335 mm respectively from outside to inside. The rotation rate of the tank ranges from 0.01 rpm up to 20 rpm with a precise increment of 0.01 rpm.

Nevertheless, for the experimental setup in the thesis, as shown in fig. 3.6, only the outer gap is required and acts as a circular channel. To measure the propagation of the bores in this circular channel, multiple ultrasonic sensors have been mounted along the central line of the outer gap above the tank with a certain distance from each sensor. The ultrasonic sensors measure the distance from the sensor to the fluid surface and thus reveal the motion of bores. The data from the ultrasonic sensors are collected and recorded by the computer on the platform in the middle of the tank via a digital I/O device from National Instruments.

## 4 Measurement Techniques

Plenty of measurement techniques have been developed for measuring the motions of the fluids. Choosing an appropriate measurement technique is an essential step for laboratory experiments. To measure the flow motions without introducing extra disturbances, a non-intrusive measurement technique are usually preferred.

For the experiments presented in the thesis, several measurement techniques have been applied for different purposes: rheoscopic flow visualisation, particle image velocimetry, and supersonic sensors. These techniques will be explained in the following sections.

### 4.1 Rheoscopic Flow Visualisation

The rheoscopic flow visualisation is a classical but still commonly used technique for qualitatively visualising the spatial flow structures by seeding the working fluid with rheoscopic fluid. The rheoscopic fluid, which means “current showing” fluid, is composed of microscopic, anisotropic and reflective flakes that can suspend in the working fluid. Due to the anisotropy, the flakes align preferentially with the shear planes in the flow for pure shear flows and reflect differing intensities of light under appropriate illumination, which makes the movement of the currents visible [18].

The early application of the rheoscopic fluids can date back to 1785 when Wilcke used burnt lime particles to visualise the breakdown of the vortex in the fluid under stirring [115]. Since then, many well-known experiments in fluid mechanics have been done with the use of rheoscopic fluids, such as the visualisation of the convection patterns in heated fluid layers by Bénard [116], the visualisation of the flow around a solid body by Prandtl [99] and the visualisation of the wavy vortex structure of Taylor-Couette flow by Schultz-Grunow [103].

Variations of seeding materials have been used as rheoscopic fluid, such as mica, metallic flakes, or fish scales in suspension in a fluid. One of the most popular rheoscopic fluids is Kalliroscope, which is based on suspensions of crystalline guanine extracted from fish scales and invented by the artist Paul Matisse in 1966 for creating kinetic sculptures. The name “Kalliroscope” comes from the Greek words “Kalos”, “Rheos” and “Skopien” meaning Beauty, Flow and Seeing [82]. A number of properties contribute to the prevalence of Kalliroscope. Due to its small platelet size ( $6 \times 30 \times 0.07 \mu\text{m}$ ) and relatively low density ( $1.62 \text{ g/cm}^3$ ), Kalliroscope flakes have a low sedimentation velocity ( $\approx 0.1 \text{ cm/h}$  in water) com-

paring to other materials and the spin-up time in most laboratory experiments. Kalliroscope also has a high refractive index (1.85) and a transparent body, which makes it effective in visualising the current structure with the help of external illumination, such as a laser beam [83].

Although Kalliroscope is a powerful tool in flow visualisation, the Kalliroscope Corporation stopped the production of Kalliroscope because of the scarcity of raw materials in 2014. Finding a perfect alternative is still an issue for many researchers [18].

## 4.2 Particle Image Velocimetry

The particle image velocimetry (PIV) is an indirect and non-intrusive optical measurement technique that uses particles and their images to deliver the velocity field of the fluid throughout a region quantitatively. The velocity of the flow is acquired by measuring the displacement of the ensembles of tracer particles between two images captured at two instants of time. The basic working principle of PIV includes seeding, illumination, recording, calibration, evaluation and post-processing [99]. The schematic sketch in fig. 4.1(a) shows the planar PIV or 2D2C PIV (two-dimensional velocity field and two velocity components) for the present laboratory experiment.

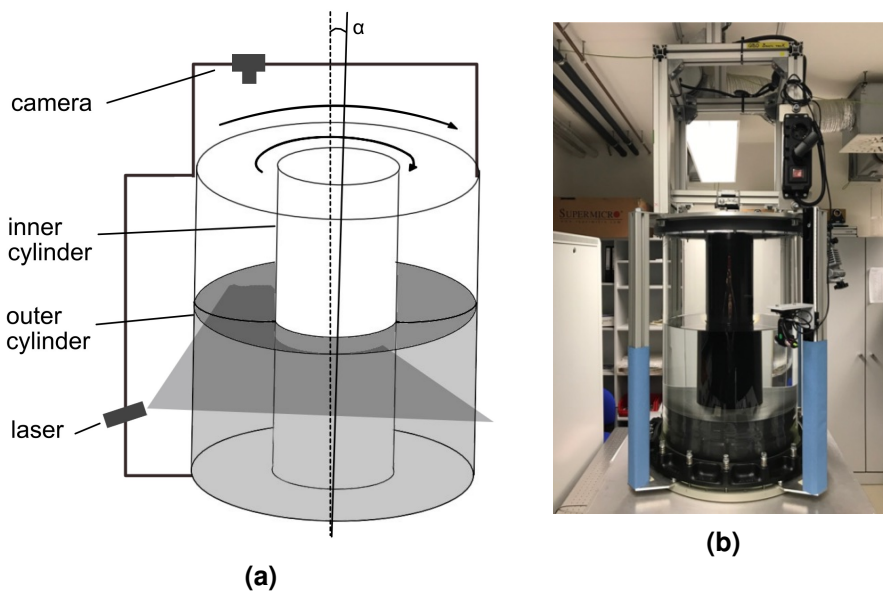


**Figure 4.1:** (a) The schematic sketch and (b) photography of the laboratory apparatus showing the installation of the measuring devices.



### 4.2.1 Seeding

In most applications in laboratory experiments, extended tracer particles are required to be added to the flow so that the motion of the particles can be used to estimate the kinematics of the local fluid. As an indirect measurement technique, PIV measures the velocity field by the displacement of the tracers instead of the fluid. In order to avoid significant discrepancies between fluid and particle motion, the interaction of the particles and the surrounding fluid has to be examined.

An estimation for the velocity lag  $U_s$  of a spherical particle in a continuously accelerating fluid, or the particle's behavior under acceleration, can be derived from Stokes's drag law:

$$U_s = d_p^2 \frac{\rho_p - \rho}{19\mu} a, \quad (65)$$

where  $\rho_p$  and  $\rho$  denote the density of the particle and the fluid,  $d_p$  is the diameter of the particle,  $\mu$  is the dynamic viscosity of the fluid and  $a$  is the acceleration. In the flow with relatively low velocity accelerations, e.g. the experiments discussed in the thesis, the lag is induced by the gravitational force, which yields

$$U_g = d_p^2 \frac{\rho_p - \rho}{19\mu} g. \quad (66)$$

Apparently, both  $U_g$  and  $U_s$  can be avoided if the density of the particles matches the fluid, i.e. neutrally buoyancy [99]. Therefore, the particles are chosen to be near neutrally buoyant to reduce the drag lag and also the sedimentation. In addition, the particles are required to efficiently scatter light for better visualisation.

In the present experiment, the water is seeded with hollow glass spheres (HGS) from Dantec Dynamics<sup>®</sup>, see table 4.1, which have the mean particle diameter of  $10 \mu\text{m}$  and the density of  $1.1 \text{ g/cm}^3$ . The tracer gives the gravitationally induced velocity  $U_g$  in the order  $10^{-6} \text{ m/s}$  and  $U_s$  is even smaller than  $U_g$ . Hence the lag of the particles can be neglected and the motion of the tracers matches the current.

### 4.2.2 Illumination

A laser device is a commonly used solution for the illumination in PIV. Because the laser has monochromatic light with high energy density, laser devices can be easily modified with additional optical lens to bundle the laser beams into thin light sheets for illuminating and recording the trace of the particles without chromatic aberrations [99].

According to the operating mode, a laser device can be classified as either continuous laser or pulsed laser, depending on whether the power output is continuous

**Table 4.1:** Specifications of hollow glass spheres. Source: [www.dantecdynamics.com](http://www.dantecdynamics.com).

	Unit	Hollow glass spheres	Silver-coated hollow glass spheres
Mean particle size	$\mu\text{m}$	10	10
Size distribution	$\mu\text{m}$	2-20	2-20
Particle shape		spherical	spherical
Density	$\text{g}/\text{cm}^3$	1.1	1.4
Melting point	$^{\circ}\text{C}$	740	740
Refractive index		1.52	-
Material		Borosilicate glass	Borosilicate glass

over time. A pulsed laser device usually emits laser with higher energy density than the continuous laser device and hence can more effectively freeze the images of tracer particles moving at high speed. On the other hand, the PIV system with a pulsed laser is generally more complex than a continuous laser system since the synchronisation between the laser pulse and the camera must be taken into consideration.

**Figure 4.2:** MediaLas® Compact line laser kit GREEN 75mW. Source: [www.medialas.de](http://www.medialas.de).

For the present experiments, due to the relative small velocities, a continuous laser is already able to fulfil the requirement of the illumination and meanwhile keeps the measurement system as simple as possible. For this purpose, a green Diode-pumped solid-state (DPSS) laser from MediaLas®, see fig. 4.2, has been applied. The laser device has a build-in line generating optic that bundles the laser beam into a laser sheet with  $110^{\circ}$  projection angle. The compact body size and lightweight also reduce the possible influence on the rotating container. The detailed technical specifications are listed in table 4.2.

### 4.2.3 Recording

With the development of the digital camera and CMOS technology, the application of an unconventional camera in PIV becomes possible. Comparing with a

**Table 4.2:** Technical specifications of MediaLas® Compact line laser kit GREEN 75mW.

Laser power:	75 mW
Wavelength/Color:	532 nm GREEN
Projection angle:	110 deg
Line length:	3 m @ 1 m distance, 6 m @ 2 m distance, ...
Divergence:	typ. < 1 mrad
Power supply:	24 V DC / < 200mA
Connector:	Flying leads
Length of wires:	Ca. 1 m
Laser class:	Class 1/2
Dimensions:	18 × 75 mm
Temperature range	+10°C - +30°C
Operating time:	8-12h per day
Typical lifetime:	typically >8000 h

scientific high-speed camera, a mobile phone camera is able to provide a reasonable result even under a relatively high sampling rate (240 Hz) with a significantly lower cost [29].

In our experimental setup, we use a GoPro Hero 7 black for recording, which runs at 30 or 60 frames per second (FPS) sampling frequency and 1920×1080 pixels resolution. To achieve a better video quality, the GoPro camera is modified by replacing the original ultra-wide-angle lens with a C-Mount, so that the camera is compatible with an extended C-Mount lens, which provides an obviously better optical quality and smaller optical distortion. In practice, a 12mm f1.6 and an 8mm f1.4 lens are used depending on the distance from the camera to the laser sheet. Powered by a Lithium-ion battery and controlled by a mobile phone, the GoPro camera can work wirelessly.

**Figure 4.3:** Back-bone modified GoPro Hero 7 Black. Source: [www.back-bone.ca](http://www.back-bone.ca).

During the PIV measurement, the condition of illumination is limited by the

power of the laser device. For an optimum recording quality, settings of the Go-Pro camera should be properly configured, as a result, the settings are a balance of ISO, lens aperture and shutter speed.

The ISO represents the light sensitivity of a digital image sensor. A high ISO indicates the sensor more sensitive to the light and meanwhile usually having a higher noise level on the outputted image. Limited by the size and capability of the CMOS imaging sensor of the GoPro camera, the ISO should not exceed 6400 for a lower noise level.

The aperture of the lens controls the amount of light received by the sensor in unit time. A larger aperture allows more light to reach the camera sensor. Meanwhile, the aperture size also relates to the depth of field or the focus range. A larger aperture has a shallower depth of field, which only gives a clear view of particles on the plane laser sheet, when focused properly, and blurs particles not on the laser plane but still visible due to the refracted or reflected lights. On the other hand, a shallower depth of field requires the focus to be very accurate to keep the image sharp.

The shutter speed regulates the total time for the sensor receiving lights. A longer shutter speed increases the brightness of the image but might not be able to capture a rapidly moving particle clearly. It also needs to be noticed that the shutter speed should be faster than the sampling rate, e.g. for a video with 60 FPS, the shutter speed should not longer than  $1/60$  second.

#### 4.2.4 Calibration

From the camera, the displacement of the particles is recorded in the image plane in pixel units. Calibration is necessary in order to convert the displacement in pixel to the physical world. For the planar PIV, a calibration target, e.g. a plate with a regular pattern, is used by placing the plate into the measurement plane. In the experiment, we use a checker board with  $2 \times 2$  cm grid size cut into an annular form as the calibration target and place the board into the fluid at the position of the laser sheet, see fig. 4.4. Depending on the distance from the camera to the measurement plane, the relation of the digital scale to the physical scale ranges from 35 to 40 pixels/cm.

#### 4.2.5 Evaluation and post-processing

The evaluation and the post-processing are performed in MATLAB<sup>®</sup> with a free open-source PIV toolbox called MatPIV, which is developed by the Department of

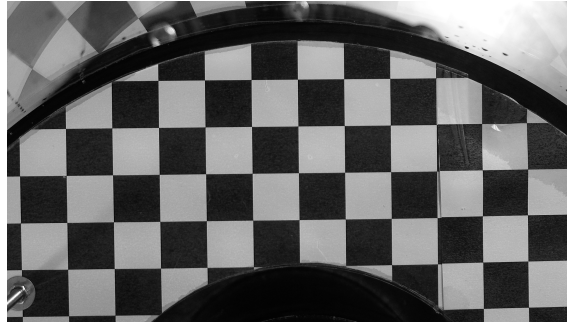


**Figure 4.4:** PIV calibration with a checker board plate.

Mathematics of University of Oslo [108]. Although there are multiple algorithms in PIV evaluation, the basic principle relies on pattern matching between two images with cross-correlation.

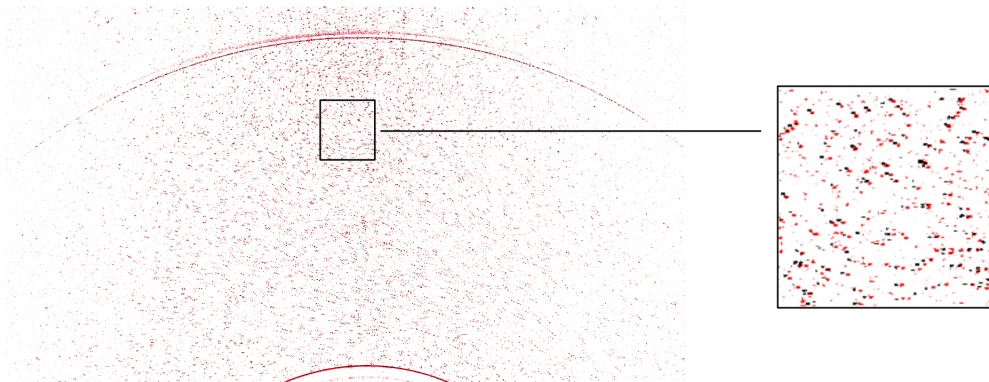


**Figure 4.5:** Inversed gray monochromatic photo shows the displacement of the particles during a time interval  $\Delta t = 0.3s$ . The black and red colour represent particles of different images. The dots beyond the upper arc are reflections on the outer cylinder.

Assuming two images separated by a time distance of  $\Delta t$ , e.g. fig. 4.5. Figure 4.5 is the superposition of two images from the camera, each of them is processed by converting the colour space from colour into greyscale and inverting the colour to turn the black background into white. The second image is plotted by replacing the black colour with red so that particles with different colour indicate positions at different time.

For further processing, the images are subsequently divided into smaller regions, also referred as sub-windows or interrogation-windows, see fig. 4.6. Each sub-window in the first image is compared with the corresponding sub-window in the second image. Denoting the  $(i, j)$  sub-window of the two images as  $I_1^{i,j}$  and  $I_2^{i,j}$ , where  $I_1$  and  $I_2$  are the samples (e.g. intensity values) extracted from the images, the best matched sub-window between the two images can be found

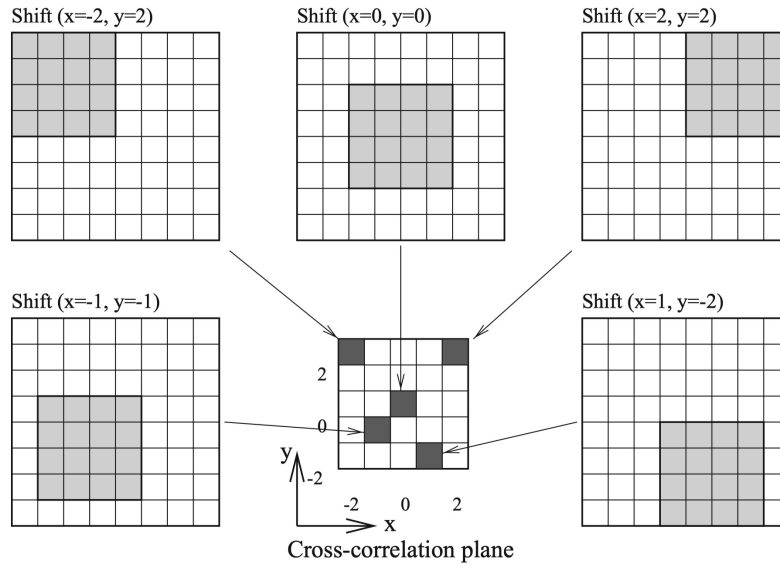


**Figure 4.6:** Example of a discrete cross-correlation by applying a  $4 \times 4$  sub-window on an  $8 \times 8$  image sample, reprinted from Raffel [99].

statistically with the use of discrete cross-correlation, which is defined as

$$R(x, y) = \sum_{m=-M}^M \sum_{n=-N}^N I_1^{i,j}(m, n) \cdot I_2^{i,j}(m + x, n + y). \quad (67)$$

The maximum value of  $R(x, y)$  represents the best match and the respective  $(x, y)$  gives the shift, i.e. the displacement, in pixels in two directions.

During this step, two parameters need to be noticed: sub-window size and windows overlap.

The parameter sub-window size is usually a base-2 dimension (e.g. 16, 32, 64 or 128) depending on the displacement of the particles and can be quadratic or non-quadratic. The reason for the base-2 dimension is that some PIV evaluating algorithms use FFT to perform correlation in the frequency domain and runs faster with a base-2 dimension. The maximum recoverable displacement range is limited to the half of the sub-window size. However, increasing displacements will decrease possible particle matches and thus reduce the signal strength of the correlation peak [99]. In practice, we follow the so-called one-quarter rule that choosing the sub-window size so that the maximum displacement does not exceed  $1/4$  of the sub-window size [57]. Nevertheless, this requirement is only needed to be satisfied with the first iteration when using iterative evaluation techniques with window-shifting.

The windows overlap is a number between 0 and 1 denoting the overlap of the

interrogation regions (subwindows). Usually this parameter is set to 0.5 or 0.75 which means 50% or 75% overlap of the interrogation windows.

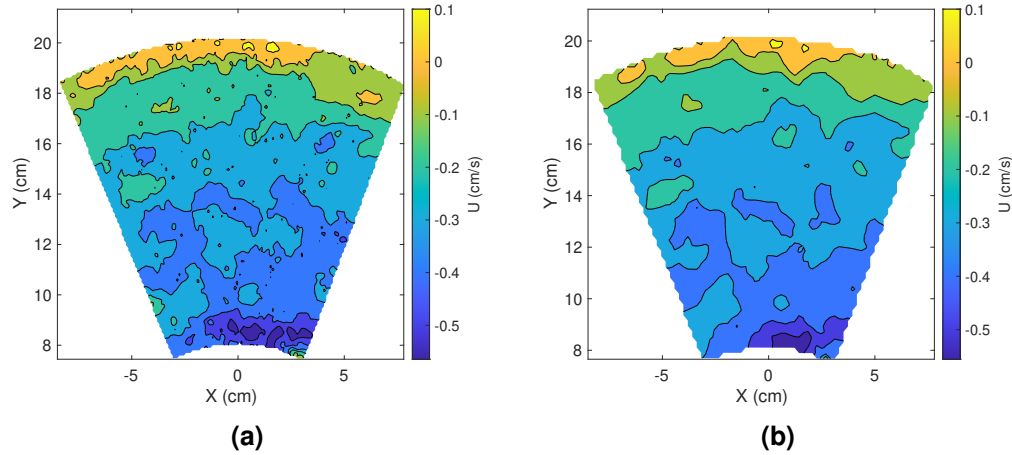


**Figure 4.7:** Evaluating the same two images with different final interrogation window sizes: (a)  $16 \times 16$  pixels and (b)  $32 \times 32$  pixels.

A comparison of different interrogation window sizes is shown in fig. 4.7 for sub-window sizes with  $16 \times 16$  and  $32 \times 32$  pixels. With a  $1920 \times 1080$  pixels image size and a 50% overlap, the evaluation with a  $16 \times 16$  ( $32 \times 32$ ) sub-window size gives the result in the form of a 2D vector array indicating displacements between two images with the size of  $238 \times 132$  ( $119 \times 66$ ).

A smaller size sub-window, such as  $16 \times 16$  in fig. 4.7(a), provides a higher resolution in the flow field than a larger sub-window ( $32 \times 32$  in fig. 4.7(b)). On the other hand, a  $16 \times 16$  sub-window leads to a dramatic increase in the time consumption for the PIV processing and the storage size of the final data by as high as 4 times compared with a  $32 \times 32$  sub-window size. By post-processing, such as performing a harmonic analysis, a larger size array also requires a more powerful computer. For the convenience of post-processing, we use an iterative evaluation technique with the final sub-window size of  $32 \times 32$  and overlap of 50%.

A 2D vector field directly from the evaluation, as shown in fig. 4.8(a), usually has some imperfections, such as abnormal vectors in fig. 4.8(a) or high-frequency noises. Therefore it is common to applying a series of filters to enhance the final result. Such filters include a peak height filter that removes enormous vectors from the vector field, a Signal-To-Noise ratio filter that removes high-frequency noises, a global filter that removes vectors significantly larger or smaller than a majority of the vectors, and a local filter that filters velocities based on the squared difference between individual velocity vectors and the median or the mean of

their surrounding neighbours. The removed spurious vectors will be replaced by interpolations of the neighbouring vectors [109]. A filtered vector field is shown in fig. 4.8(b), where the outliers have been removed and the field is obviously smoother.

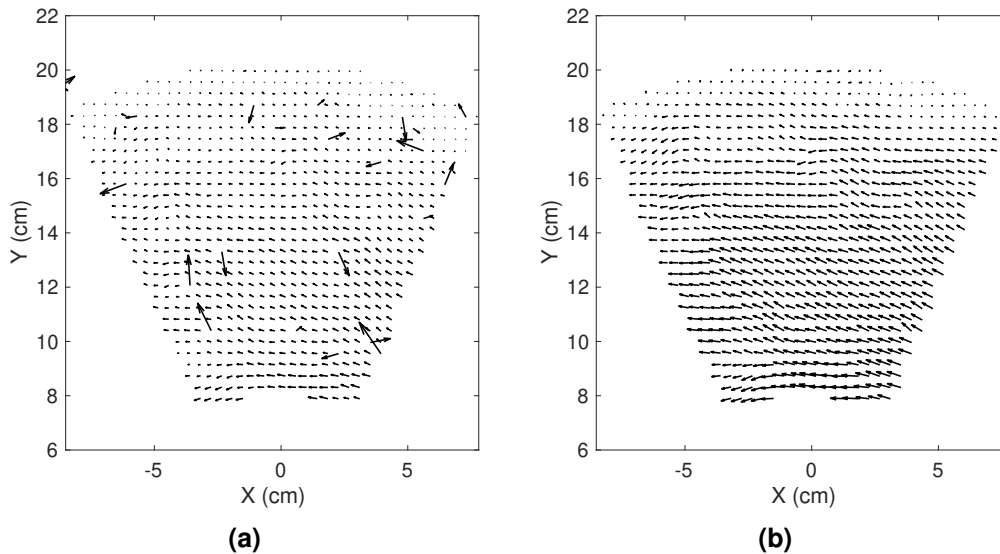


**Figure 4.8:** Comparison of a vector field (a) directly from the evaluation and (b) filtered to remove outliers.

### 4.3 Ultrasonic Sensors

An ultrasonic sensor is a contactless measuring instrument that measures the distance from the sensor to an object using ultrasonic sound waves. The sensor uses a transducer, which acts as a microphone, to emit sound waves at a frequency above the range of human hearing, receive the echoes reflected from the surface of the measured body and convert the reflected sound into an electrical signal. By measuring time lapses between the sending and receiving of the ultrasonic pulse, the distance to the target is thus determined.

Ultrasonic sensors are used primarily as proximity sensors in automatic systems, such as automobile self-parking systems, anti-collision safety systems and robotic obstacle detection systems, as well as level sensors to detect, monitor, and regulate liquid levels in closed containers.

Ultrasonic sensors are practical instruments for measuring liquid levels due to their high accuracy and short response time. In our experiment, we used ultrasonic sensors mic+25/IU/TC from microsonic<sup>®</sup>, see fig. 4.9, with its detailed technical specifications listed in table 4.3. Figure 4.9(b) shows the detection zone of the ultrasonic sensor, where the red color indicates the zone in which the sensor



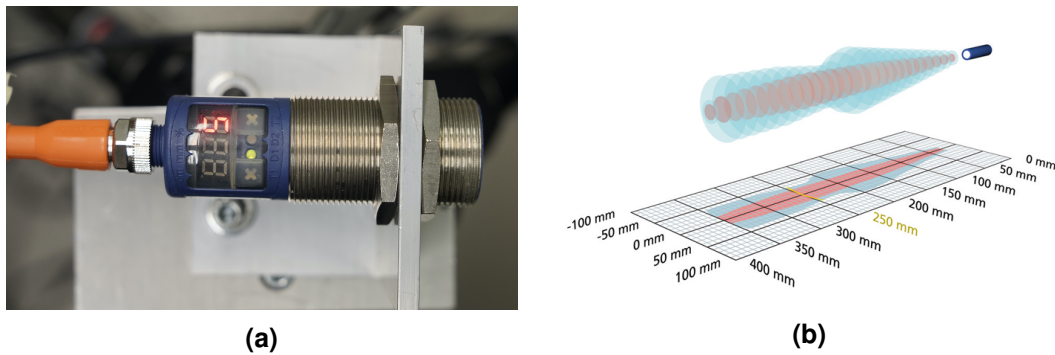


**Figure 4.9:** (a) Microsonic<sup>®</sup> mic+25/IU/TC ultrasonic sensor and (b) its detection zones from [www.microsonic.de](http://www.microsonic.de).

is able to detect the distance to a small body-size target (with 27 mm diameter). For an accurate measurement, the sensors are fixed perpendicular to the fluid surface with an optimized distance about 250 mm. Co-operating with the digital I/O device, the ultrasonic sensor works with a sampling rate at 100 Hz, which is sufficient in tracking the variation of the fluid surface due to surface gravity waves.

**Table 4.3:** Technical specification of Microsonic® mic+25/IU/TC ultrasonic sensor.

measuring range	30 - 350 mm
design	cylindrical M30
operating mode	analogue distance measurements
ultrasonic-specific	
means of measurement	echo propagation time measurement
transducer frequency	320 kHz
blind zone	30 mm
operating range	250 mm
maximum range	350 mm
resolution/sampling rate	0.025 - 0.10 mm
reproducibility	± 0.15 %
accuracy	± 1 % (temperature drift internally compensated)
electrical data	
operating voltage	9 - 30 V d.c., reverse polarity protection
voltage ripple	± 10 %
no-load current consumption	≤ 80 mA
type of connection	5-pin M12 initiator plug
output	analogue output current: 4-20 mA / voltage: 0-10 V
response time	32 ms
delay prior to availability	<300 ms

## 5 Methods of Data Analysis

In this chapter, the methods for analysing the velocity field from PIV data are briefly introduced. For more detailed information the reader might be referred to the textbooks such as Emery and Thomson [38] and Wilks [117].

### 5.1 Discrete Fourier Transform

Fourier analysis is one of the most popular methods in data analysis that transforms the time or spatial data series into signals in frequency or wavenumber domain or in the other way around. This technique is commonly used for identifying periodic components in a long time-series data, determining prominently appearing frequencies and the respective amplitudes in a signal, removing random and aperiodic fluctuations from periodic data, filtering high/low frequency signals from time series (see fig. 5.1), etc. The basic premise of Fourier analysis is that any periodic time series  $x(t)$  with  $t \in [0, T]$  can be reproduced with a linear summation of cosines and sines that

$$x(t) = \overline{x(t)} + \sum_p [A_p \cos(\omega_p t) + B_p \sin(\omega_p t)], \quad p = 1, 2, \dots \quad (68)$$

where  $\overline{x(t)}$  is the mean value of the time series,  $A_p$  and  $B_p$  are constants called Fourier coefficients and the specified angular frequencies  $\omega_p$  are integer  $p$  multiples of the fundamental frequency  $\omega_1 = 2\pi/T$ . The decomposition process that transforms time series into a function of frequency is named as Fourier transformation.

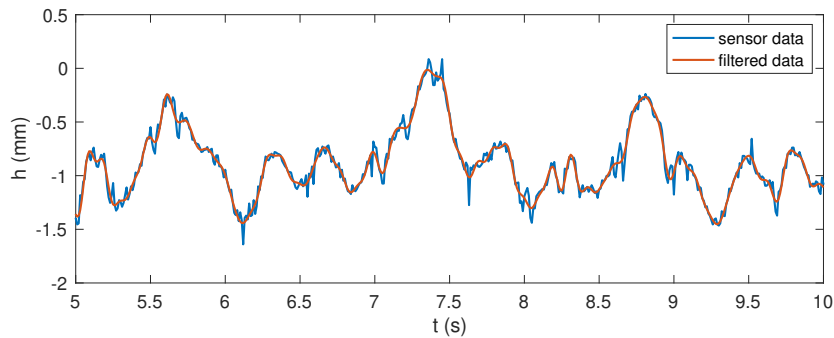


**Figure 5.1:** Removing high frequency noise of data from an ultrasonic sensor by FFT

In practical situations, most of the experimental data are collected and stored in digital form as non-periodic time-discrete data series, such as velocity fields from

PIV. To deal with the discrete data, we need to use the discrete Fourier transform (DFT). For a finite length data set with size  $N$ , there is

$$X_n = \sum_{k=0}^{N-1} x_k e^{-i2\pi n \frac{k}{N}} \text{ for } k = 0, 1, \dots, N-1. \quad (69)$$

The DFT is usually computed with the algorithm fast Fourier transform (FFT), which reduces the complexity of DFT computation from  $O(N^2)$  to  $O(N \log N)$  and largely improved the data processing efficiency.

## 5.2 Short Time Fourier Transform

Short-Time Fourier Transform (STFT) (or short-term Fourier transform) is a simple but effective tool for analysing time-frequency distributions. STFT provides time-localized information of frequency components of a signal whose spectra changes over time, whereas the standard Fourier transform provides information in frequency domain averaged over the entire signal time interval. Due to its ability that decomposes frequency and time information, STFT is widely used in sound processing such as audio feature extraction [90]. In geophysical fluid dynamics, STFT has also been used to reveal the slowly varying energy cascade as a function of time [20].

The fundamental concept of STFT is partitioning the signal in time-domain into a sequence of disjointed or overlapped blocks of shorter duration by multiplying the signal with a window function, and applying a sequence of Fourier transforms over the windowed signals.

The amplitude temporal evolution is derived by applying a short-time Fourier transform over the velocity as follows:

$$A(t, \omega) = \left| \int_{-\infty}^{+\infty} u(\tau) h_w(\tau - t) e^{-i\omega\tau} d\tau \right| / \int_{-\infty}^{+\infty} h_w(\tau - t) d\tau, \quad (70)$$

where  $h_w$  stands for the function of a smoothing Hamming window [9].

Since STFT uses FFT calculating the spectra for each signal block, it is usually very efficient. The size and type of the window is the most concerned parameter when performing STFT, since there exists a trade-off between time and frequency resolution in STFT. A narrow-width window provides a better resolution in the time domain but leads to a poor resolution in the frequency domain, and vice versa. Due to the relatively low frequency of the Kelvin modes and the slow-changing amplitude in terms of the time, a wide window function has been ap-

plied in processing the experimental data.

In practice, the computation of STFT is performed with the help of the Time-Frequency Toolbox for MATLAB<sup>®</sup> developed by CNRS (France) and Rice University (USA) [9].

### 5.3 Harmonic Analysis

Standard Fourier analysis computes amplitudes in full frequency domain  $f_1, f_2, f_3, \dots, f_N$  ( $f_1$  is the fundamental frequency and  $f_N$  is Nyquist frequency). However, standard Fourier analysis does not allow to analyse data in terms of predetermined frequencies that often occurs in cases of wave motions. To solve this problem, we use a signal demodulation method called harmonic analysis, in which we are able to examine wave motions of predetermined frequencies.

Similar to Fourier analysis (68), the discrete time series  $x(t_n)$ ,  $n = 1, 2, \dots, N$  can be expressed as

$$x(t_n) = \bar{x} + \sum_{q=1}^M [A_q \cos(2\pi f_q t_n) + B_q \sin(2\pi f_q t_n)] + x_r(t_n) \text{ for } q = 0, 1, \dots, M. \quad (71)$$

where  $\bar{x}$  is the mean value of the data set,  $M$  is the number of prescribed frequencies  $[f_1, f_2, \dots, f_M]$  to be analysed,  $A_q$  and  $B_q$  are harmonic coefficients and  $x_r(t_n)$  is the residual part of the data set.  $A_0$  is the temporal mean of the time series and  $B_0 = 0$ . The amplitude  $C_q$  and phase  $\phi_q$  of a specified harmonic component of frequency  $f_q$  is determined by harmonic coefficients  $A_q$  and  $B_q$  that

$$C_q = (A_q^2 + B_q^2)^{1/2}, \quad (72)$$

$$\phi_q = \tan^{-1}(B_q/A_q). \quad (73)$$

The aim of harmonic analysis is to determine the coefficients  $A_q$  and  $B_q$  in (71) for the  $M$  prescribed frequencies. For this purpose, the variance  $e^2$  of the residual term  $x_r(t_n)$  in (71) is introduced and defined as

$$e^2 = \sum_{n=1}^N x_r^2(t_n) = \sum_{n=1}^N \left\{ x(t_n) - \left[ \bar{x} + \sum_{q=1}^M [A_q \cos(2\pi f_q t_n) + B_q \sin(2\pi f_q t_n)] \right] \right\}^2. \quad (74)$$

Further a least square method is employed to find the particular  $A_q$  and  $B_q$  that minimises the variance  $e^2$ . The  $A_q$  and  $B_q$  are then the coefficients with the best

fit for (71).

## 5.4 Mode Reconstruction

In the current experimental setup, due to the presence of the non-transparent inner cylinder, a PIV measurement on the full horizontal annulus cross-section with a single camera is not available. Limited by the view angle of the measuring camera, the measurement of the PIV only gives an annular sector of the full annulus with a view angle of about  $50^\circ$ , as shown in fig. 5.2. To obtain the wavenumber of a mode in the azimuthal direction, a reconstruction of the mode for the complete annulus gap is required.

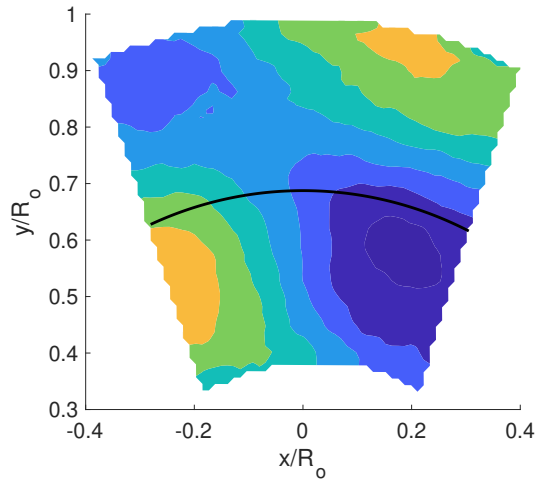


**Figure 5.2:** Azimuthal velocity field of frequency  $\omega/\Omega = 1.165$  preprocessed by harmonic method from PIV result for  $H = 24\text{cm}$ ,  $\text{Ek} = 1.19 \times 10^{-5}$ ,  $\text{Fr} = 0.09$ ,  $\alpha \approx 1^\circ$ .

For this purpose, we first extract the velocity field of a particular mode with the help of harmonic analysis, such as the azimuthal velocity field of the mode with frequency  $\omega/\Omega = 1.165$  (see fig. 5.2). The next step is to decide a particular radius for detecting the wavenumber, e.g. the black arc in fig. 5.2 with  $r = (R_i + R_o)/2$ . Since the velocity field of the mode is periodic, the evolution of azimuthal velocity for grids of  $r = (R_i + R_o)/2$  can be plotted as a function of time over several periods, see fig. 5.3(a).

Considering the mode is continuous and periodic in the azimuthal direction, the propagation of the wave can be predicted by expanding the contour in fig. 5.3(a) along the wave propagating direction on the  $\theta - t$  plane. Following this procedure for all times, we will obtain the temporal velocity evolution for the complete circumference, as shown in fig. 5.3(b). The azimuthal wavenumber is

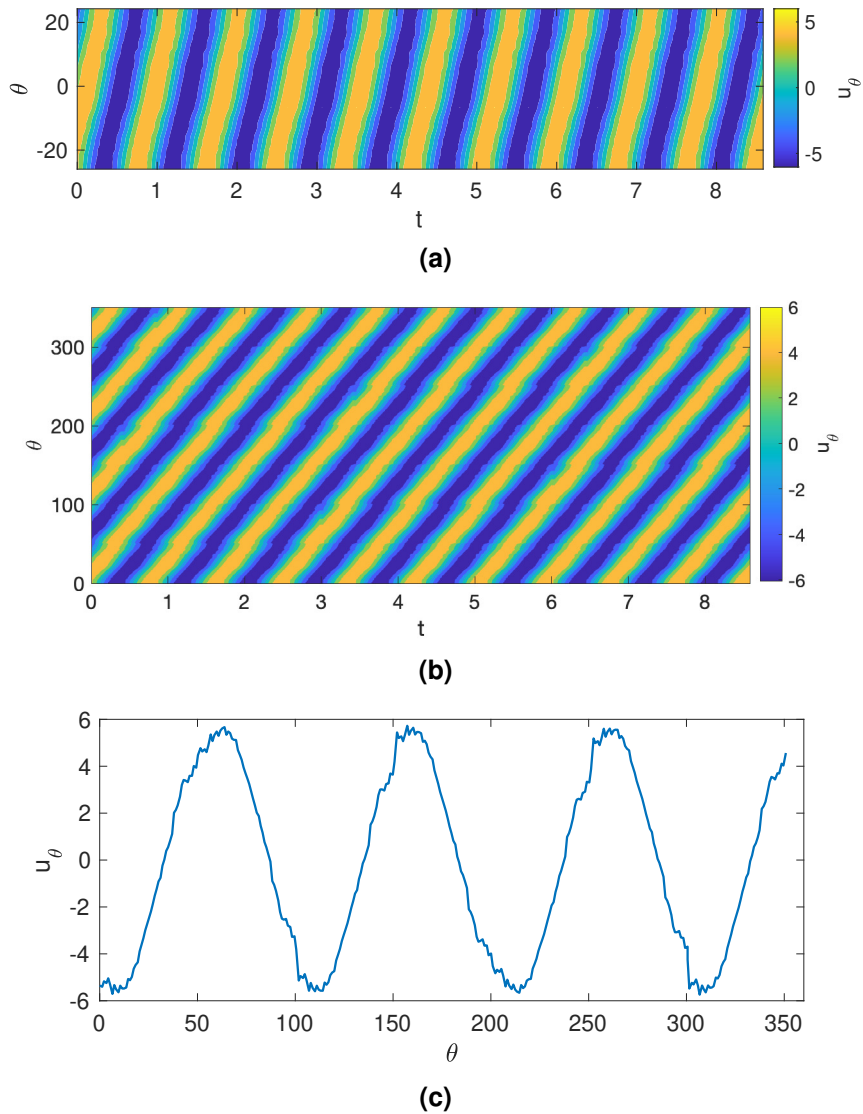


**Figure 5.3:** The procedure for detecting the wavenumber in azimuthal direction using azimuthal velocity. The angle  $\theta$  is given in degrees. (a) A Hovmöller diagram shows the time evolution of azimuthal velocity profiles for  $\theta = -24^\circ - +24^\circ$ ; (b) a Hovmöller diagram expanded from (a) shows the time evolution of azimuthal velocity profiles for the full circumference; (c) the azimuthal velocity  $u_\theta$  as a function of  $\theta$  for  $t = 1.3$  shows the distribution of  $u_\theta$  on the circumference for  $r = (r_i + r_o)/2$ .

easily obtained by simply counting the number of stripes with the same color for  $\theta = 0 - 360^\circ$  at a certain time in fig. 5.3(b), or by plotting the azimuthal velocity  $u_\theta$  as the function of  $\theta$  for an arbitrary time, see fig. 5.3(c). In practice, such a  $u_\theta - \theta$  diagram as fig. 5.3(c), which shows the wave structure on the full circumference, might not always give an integral wavenumber. In this case, a close integer will be taken as the azimuthal wavenumber.

## 5.5 Bispectra Analysis

Bispectra analysis is part of higher-order spectral analysis (HOSA), which is a tool for analysing the nonlinearity of a system under a random input. Higher-order spectra (HOS), which refers to one order greater than two, are defined by higher-order cumulants of data. Compared to standard Fourier analysis, HOSA provides several advantages in processing stochastic non-Gaussian signals, e.g. HOS preserve the phase information of non-Gaussian parametric signals that are not contained in traditional Fourier analysis and HOSA is able to detect and characterize the nonlinear interactions in a system via phase relations of the harmonic components. In practice, the analysis is performed with the help of the HOSA MATLAB<sup>®</sup> toolbox [92].

Since HOS have an order greater than two, a third-order spectrum is called as bispectrum. Fundamentals of the bispectrum are introduced as follows.

For a real, stationary, zero-mean random data set  $x(t)$ , the first-, second- and third-order cumulants are defined as

$$\begin{aligned} C_1 &= E\{x(t)\}, \\ C_2(\tau_1) &= E\{x(t)x(t + \tau_1)\}, \\ C_3(\tau_1, \tau_2) &= E\{x(t)x(t + \tau_1)x(t + \tau_2)\}, \end{aligned} \tag{75}$$

where  $E$  is the expectation and  $\tau_1, \tau_2$  are lags in cumulants. The first-order cumulant  $C_1$  is equal to the mean value of the data set, which is usually subtracted from the data set if  $\overline{x(t)} \neq 0$  so that  $C_1 = 0$ . The second-order cumulant  $C_2(\tau_1)$  is identical to an autocorrelation function, which provides a measure of how the sequence is correlated with itself at different time points. A Fourier transform of the second-order cumulant gives the traditional power spectrum. Applying Fourier transform to the third-order cumulant  $C_3(\tau_1, \tau_2)$ , we get the bispectrum,



which can be expressed in the form

$$\begin{aligned} B(\omega_1, \omega_2) &= \sum_{\tau_1=-\infty}^{+\infty} \sum_{\tau_2=-\infty}^{+\infty} C_3(\tau_1, \tau_2) \exp\{-i(\omega_1\tau_1 + \omega_2\tau_2)\} \\ &= X(\omega_1) X(\omega_2) X^*(\omega_1 + \omega_2) \end{aligned} \quad (76)$$

where  $|\omega_1| \leq \pi$ ,  $|\omega_2| \leq \pi$ ,  $|\omega_1 + \omega_2| \leq \pi$ ,  $X(\omega)$  is the Fourier transform of time series  $x(t)$  and  $*$  denotes the complex conjugate.

The definition of the third-order cumulant (75) and the bispectrum (76) reveals some important properties of third-order spectra analysis:

1. The bispectrum  $B(\omega_1, \omega_2)$  is a product of three Fourier components, in which the frequency of one component equals the linear summation of the other two components. This product can be used to detect and quantify the quadratic phase couplings of these frequencies.

2.  $B(\omega_1, \omega_2)$  is generally complex and has magnitude and phase:

$$B(\omega_1, \omega_2) = |B(\omega_1, \omega_2)| \exp(i\phi_B(\omega_1, \omega_2)). \quad (77)$$

3. According to (75), the third-order cumulant  $C_3(\tau_1, \tau_2)$  has symmetry conditions in temporal domain that

$$\begin{aligned} C_3(\tau_1, \tau_2) &= C_3(\tau_2, \tau_1) \\ &= C_3(-\tau_2, \tau_1 - \tau_2) \\ &= C_3(\tau_2 - \tau_1, -\tau_1) \\ &= C_3(\tau_1 - \tau_2, -\tau_2) \\ &= C_3(-\tau_1, \tau_2 - \tau_1). \end{aligned} \quad (78)$$

The symmetry conditions can be expressed on the coordinate diagram on fig. 5.4(a), which shows the six symmetric sections of  $C_3(\tau_1, \tau_2)$ .

4. Similar to  $C_3(\tau_1, \tau_2)$ , the bispectrum also has symmetry properties in frequency domain:

$$\begin{aligned} B(\omega_1, \omega_2) &= B(\omega_2, \omega_1) = B^*(-\omega_2, -\omega_1) \\ &= B^*(-\omega_1, -\omega_2) = B(-\omega_1 - \omega_2, \omega_2) \\ &= B(\omega_1, -\omega_1 - \omega_2) = B(-\omega_1 - \omega_2, \omega_1) \\ &= B(\omega_2, -\omega_1 - \omega_2), \end{aligned} \quad (79)$$

and the symmetric sections are plotted on fig. 5.4(b).

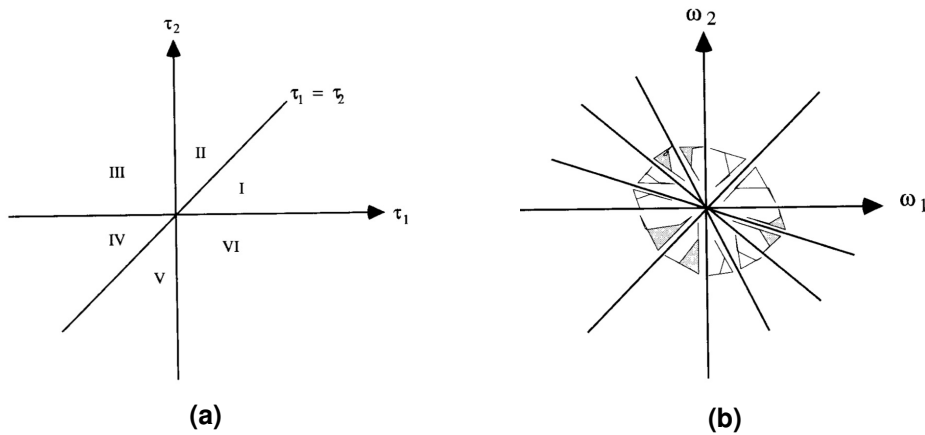


**Figure 5.4:** Symmetry regions of (a) third-order cumulants and (b) bispectra, reprinted from Nikias and Raghuveer [92].

5.  $C_3(\tau_1, \tau_2) = 0$  for all  $(\tau_1, \tau_2)$  of a stationary zero-mean pure Gaussian process and the respective  $B(\omega_1, \omega_2)$  also equals zero.

6.  $B(\omega_1, \omega_2)$  suppresses linear phase information in a way that for time series  $y(t) = x(t + n)$ ,  $n$  is a constant integer, there is  $B_y(\omega_1, \omega_2) = B_x(\omega_1, \omega_2)$ .

To quantify the quadratic nonlinearities in time series, the bispectrum can be normalised by the magnitudes that

$$b(\omega_1, \omega_2) = \frac{X(\omega_1)X(\omega_2)X^*(\omega_1 + \omega_2)}{\sqrt{|X(\omega_1)|^2|X(\omega_2)|^2|X^*(\omega_1 + \omega_2)|^2}}. \quad (80)$$

This is the so-called bicoherence, which gives a statistical measure of quadratic phase coupling. The magnitude of bicoherence ranges from 0 to 1, where 1 represents perfect phase coupling and 0 means no coupling. With the help of bicoherence, we have quantitative information about the existence of phase coupling from the PIV data.

---

## 6 Instabilities in a Tilted Rotating Annulus

### 6.1 Introduction

The instabilities of the flow in a rotating container have been studied for a long time. Lord Kelvin (William Thomson) [111] linearised and solved the Euler equations including rotation by assuming time harmonic perturbations. This solution is composed by a sum of so-called normal Kelvin modes (i.e. inertial modes), where the Coriolis force plays the role of the restoring force. The frequency of each mode is less than two times the solid-body rotation frequency. These modes are damped when viscosity is added, unless external forcing provides the energy for their excitation.

Different experimental configurations have been used to excite Kelvin modes in a rotating container. McEwan [84] performed experiments with a slightly inclined top end in a fully filled axially rotating cylinder. Thompson [110] excited this periodic motions in a partly filled and slightly tilted rotating cylinder. Malkus [76], Malkus and Waleffe [77] and Le Bars *et al.* [68] used a rotating deformable elastic cylinder, which produces inertial modes with azimuthal wavenumber 2 or 3, depending on the deformation. Precession and libration are also common methods for exciting Kelvin modes. Experiments in a precessing cylinder were performed e.g. by Manasseh [78], Meunier *et al.* [88], and Lagrange *et al.* [63], [64] and in a longitudinal librating cylinder by Busse [22], Borcia *et al.* [15] and Klein *et al.* [60]. The container can also have different shapes, e.g. spherical, rather than a cylindrical (Aldridge and Toomre [6], Hoff *et al.* [53], [54]).

When the frequency of the excited Kelvin mode differs from the resonant frequency, the fluid response can be predicted by linear inviscid theory [47]. In contrast, when the forced Kelvin mode has the same frequency as one of the resonance frequencies of the rotating fluid, the Kelvin mode becomes unstable above a threshold amplitude. The instability leads to strong nonlinear effects and results in a sudden breakdown of the flow into small scale disorder, which was referred to as “resonant collapse” by McEwan [84]. Later, in 1971 McEwan [85] suggested that the phenomenon can be explained with a triad resonance model, where two free modes form a triad in second-order resonant interaction with the forced mode. Exchanging energy with the forced mode, these free modes can lead to momentum mixing in localized regions, thus resulting in a breakdown of the inertial wave, and eventually in the resonant collapse. The breakdown regimes at various Ekman numbers, precession angles and frequencies were studied and

characterised by Manasseh [78]. At certain conditions, McEwan [85] and Manasseh [78] observed a relaminarization of the chaotic flow field after the breakdown and the rotating flow went into a breakdown-relaminarization cycle.

A series of studies by Lopez and Marques [73], [74], [80], Meunier *et al.* [63], [64], [88] investigated triadic resonance in a precessing cylinder. Marques and Lopez [80] numerically studied the bifurcation of different states of triadic resonance under detailed parametric control and revealed the complex dynamics associated with weak precessional forcing. They [73] numerically investigated the influence of the nutation angle  $\alpha$  to the flow in a precessionally-forced rotating cylinder and their work reveals strong nonlinear and detuning effects depending on  $\alpha$ . With increasing  $\alpha$ , the system goes through different regimes, from a constant state to a tuned triadic resonance state, and subsequently follows a sequence of well-characterized bifurcations associated with triadic resonance. In their simulation, they observed that a mean flow (mode  $m = 0$ ) arises with increasing  $\alpha$ . Since the energy of the mean flow is provided by nonlinearity, a more inclined rotating cylinder with a stronger nonlinearity generates a stronger mean flow. We will see that the same is true for our setup. Meunier *et al.* [88] and Lagrange *et al.* [64] used linear stability theory to predict the spatial structure and the threshold for instability due to triadic resonance. They further developed a viscous and weakly nonlinear model to predict the resonant state and derive low-order amplitude equations by coupling the forced Kelvin mode with the two free modes and the geostrophic mode.

For the rotating cylinder with a non-zero background flow, a barotropic shear instability, similar to a parallel shear flow instability in a non-rotating system, might be induced giving rise to an oscillating barotropic shear mode [21]. Thompson [110] has given the analytical prediction of the shear instability for a partly filled and slightly tilted rotating cylinder. Thompson further verified his theory experimentally and achieved good agreement. However, the velocity field was not analysed qualitatively.

In the present research we experimentally study mode interactions in an inclined rotating annulus with a free surface. This is a setup of particular interest since it is simpler than the precessing cylinder but in fact mimics aspects of rotating fluids forced by precession. This type of forcing is relevant for the dynamics of planetary bodies but also in the context of vortex dynamics: a rotating mid-latitude low-pressure system is forced by precession too since it rotates with the Earth [64]. The excitation and interaction of inertial waves in our study is similar to the partly filled rotating cylinder experiment by Thompson [110].

In our experiment, we investigate the dominant features of the free surface configuration and compare them with the bounded precession counterpart. More generally, our study is also of interest in the context of the energy cascade in rotating fluids. The breakdown of the forced large scale mode transfers energy upscale to the balanced geostrophic mode but also downscale to other free Kelvin modes. Such interactions are hence relevant for the still poorly understood energy transfer in geophysical flows.

Our research is also related to an engineering background. Instabilities could be induced due to the resonant effect in a spin-stabilized projectile with liquid payloads, which therefore could further disturb the flight stability. To avoid the resonance, a solution is to include a central rod in the cylindrical container and therefore to change the eigenfrequency. In this situation the model, as discussed in Selmi and Herbert [105], can be considered as a spinning and nutating cylindrical annulus, sharing similar features with our experimental configuration.

Finally, the study is also of interest in the context of unwanted Kelvin mode excitation [14], e.g. Rodda *et al.* [101] performed experiments with a differentially heated rotating annulus to study baroclinic waves. A global Kelvin mode was observed with a frequency equal to the annulus rotation, which was very likely driven by a slight inclination of the rotation axis.

This chapter is structured in the following way: Section 6.2 describes the theoretical background of the experiment; Section 6.3 introduces the Kelvin mode forced due to the inclination of the cylinder and its resonant breakdown; In Sec. 6.4 we discuss the geostrophic mode of the flow and several factors that influence the mean velocity profile, such as the tilt angle, the wind effect on the free surface and the filling depth; Section 6.5 and 6.6 discuss two types of instabilities, i.e. a triadic instability and a shear instability, in the tilted rotating annulus; Section 6.7 shows a dependency of the mode frequency on Ekman number due to the Doppler effect; Section 6.8 discusses the mode amplitude as a function of the Ekman number and Sec. 6.9 compares the mode amplitude with a low-order dynamic model for classical precessing cylinders. Finally, conclusions and outlooks are given in Sec. 6.10 and 6.11.

## 6.2 Experimental Background

In more classical precession experiments with circular cylinders with radius  $R$ , the cylinder is completely filled with fluid and rotates around its symmetry axis  $\hat{z}$  with angular velocity  $\Omega$ . In addition, the cylinder rotates with  $\Omega_p$  around an axis

that is inclined about an angle  $\alpha$  with respect to the cylinder's rotation axis. In this setup the direction of gravity does not play a role, and no other modes besides Kelvin modes can be excited. As is discussed in Zhang and Liao [119], for small Poincaré number  $0 < \text{Po} = \Omega_p/\Omega \ll 1$  and Ekman number  $\text{Ek} = \nu/(\Omega R^2) \ll 1$ , and further, a small amplitude of the fluid velocity in the cylinder,  $|\mathbf{u}| = \epsilon \ll 1$ , the non-dimensional governing equations in the rotating frame of the cylinder (the mantle frame) read

$$\frac{\partial \mathbf{u}}{\partial t} + 2\hat{\mathbf{z}} \times \mathbf{u} + \nabla \mathbf{p} = \text{Ek} \nabla^2 \mathbf{u} - 2\hat{\mathbf{z}} \mathbf{r} \text{Po} \sin \alpha \mathbf{e}^{i(t+\theta)}, \quad (81)$$

$$\nabla \cdot \mathbf{u} = 0. \quad (82)$$

The system is normalized by the cylinder radius  $R$  and the rotation rate  $\Omega$  in a cylindrical coordinate  $(\hat{\mathbf{r}}, \hat{\theta}, \hat{\mathbf{z}})$ . The equations need to be completed by non-slip boundary conditions. The last term in the first equation is the so-called Poincaré forcing that drives a Kelvin mode with azimuthal wavenumber  $m = 1$ .

In contrast to the precession system, the annulus in our experiment is not completely filled with fluid but has an upper free surface. It rotates around the symmetry axis  $\hat{\mathbf{z}}$  which is inclined by a small angle  $\alpha$  with respect to the direction of gravity. Obviously, in such a setup the Poincaré forcing term is missing, however, a Kelvin mode with  $m = 1$  is now driven by the upper boundary, see fig. 6.1. The governing equation is

$$\frac{\partial \mathbf{u}}{\partial t} + 2\hat{\mathbf{z}} \times \mathbf{u} + \nabla \mathbf{p} = \text{Ek} \nabla^2 \mathbf{u}, \quad (83)$$

$$\nabla \cdot \mathbf{u} = 0, \quad (84)$$

with the upper boundary condition for small angle  $\alpha$

$$w = dz/dt = \alpha r \cos(t + \theta). \quad (85)$$

Since in our case the Froude number  $\text{Fr} = \Omega^2 R/g$ , comparing the centrifugal force to gravity is small, the deformation of the surface has been neglected. As can be seen, the forcing (85) is similar to the forcing term in (81). Therefore, a strong analogy between the classical precessing cylinder (or wide gap annulus) experiment and the rotating free surface experiment can be expected when the rotation axis is tilted with respect to gravity.

Experimental configurations are introduced in detail in Sec. 3 as well as measurement techniques in Sec. 4. In this chapter, the length and time scale are nor-

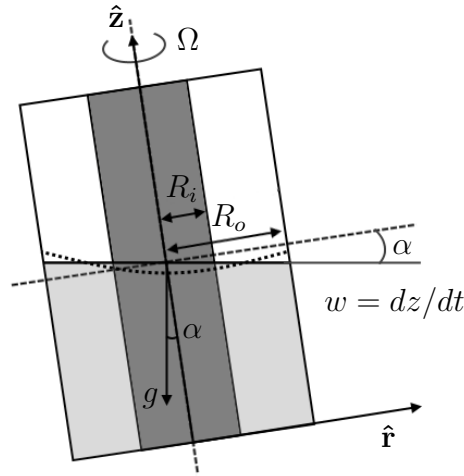


**Figure 6.1:** Sketch of the experiment that rotates with  $\Omega$  about its axis of symmetry at angle  $\alpha$  from the vertical. This tilt leads to a periodic motion at the surface that can be assumed to be flat for small Froude number  $\text{Fr} = \Omega^2 R/g$ .

malized by the radius of the outer cylinder  $R_o$  and the rotation period of the annulus  $\Omega^{-1}$  that is

$$(r, \theta, z) \rightarrow (r^*/R_o, \theta, z^*/R_o), \mathbf{u} \rightarrow \mathbf{u}^*/(R_o\Omega), t \rightarrow t^* \cdot \Omega, \omega \rightarrow \omega^*/\Omega, h \rightarrow h^*/R_o, \quad (86)$$

where  $h$  is the filling depth of the water.

Due to the limitation of the PIV technique in the present setup, the PIV measurements only provide quantitative information of velocity components on the directions subjected to the axial direction, i.e.  $u_\theta$  and  $u_r$  in a cylindrical coordinate. The amplitude of a mode is referred to as the amplitude on the horizontal plane, i.e.  $A = \sqrt{u_\theta^2 + u_r^2}$ .

Before starting a measurement, the rotating system is required to run for a sufficiently long time to ensure that the rotating flow reaches a statistically steady state. The waiting time is supposed to be longer than the spin-up time from rest, which is of the order  $\text{Ek}^{-1/2}\Omega^{-1}$ . For a rotation rate of 20 rpm, the spin-up time is around 15 minutes. In this chapter, all measurements, if not specifically noted, are performed after the annulus was rotating for at least 40 minutes.

### 6.3 Forced Kelvin Mode and Wave Breakdown

As discussed in the previous section, the periodic non-axial-symmetric gravitational torque due to the inclination acts as a force leading to the excitation of a forced Kelvin mode, which is similar to the precessional force. The periodic forcing does not directly provide energy for the Kelvin mode but plays the role as

a conveyor that extracts energy from the rotation and converts it into the fluid motions which then depart from the solid body rotation [67].

The forced Kelvin mode has the angular frequency that equals the rotation frequency of the cylinder/annulus, see fig. 6.2(a). The horizontal structure of this mode is reconstructed with the help of so-called harmonic method, as shown in fig. 6.2(c), suggesting that the mode consists of two counter-rotating vortices and indicates the forced mode having the azimuthal and radial wavenumber  $m = n = 1$ . The structure of the forced Kelvin mode reconstructed from PIV measurements also shows an excellent agreement with the linear solution of a  $m = n = k = 1$  mode from (36) (see fig. 6.2(d)).

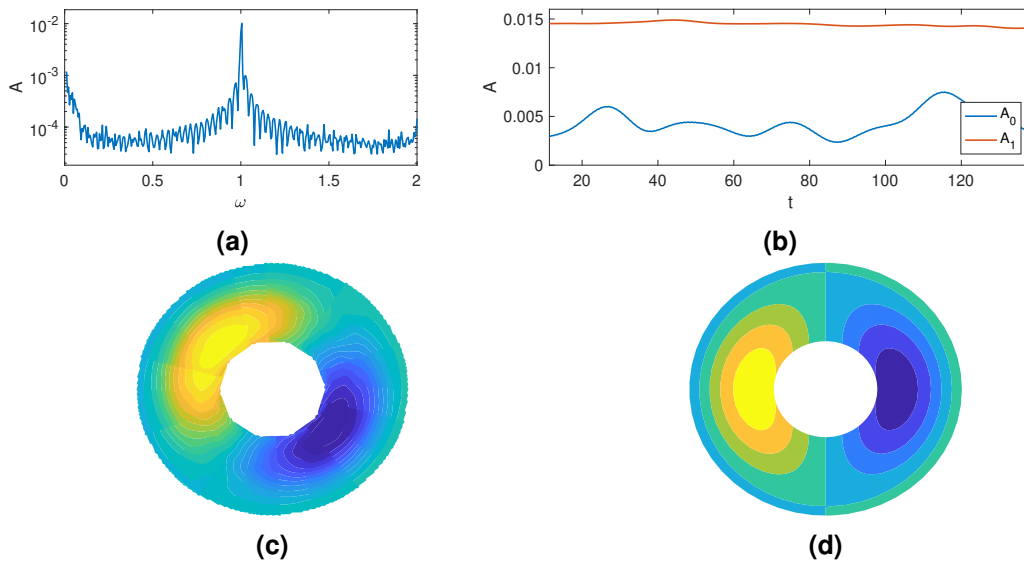


**Figure 6.2:** (a) Amplitude spectrum of azimuthal velocity; (b) temporal evolution of amplitude of the forced mode  $m_1$  and the geostrophic mode  $m_0$  for  $h = 1.2$ ,  $Ek = 2.38 \times 10^{-5}$ ,  $Fr = 0.02$ ,  $\alpha \approx 0.1^\circ$ ,  $z = 0.75h$ ; (c) reconstruction of the forced Kelvin mode based on the azimuthal velocity field from PIV measurement and (d) linear solution of the forced Kelvin mode. The colour in (c) and (d) represents the azimuthal velocity, where yellow (blue) indicates clockwise (anti-clockwise) direction.

The vertical structure of the forced mode is depending on the filled fluid depth and can be observed optically with the aid of rheoscopic fluid such as Kalliroscope (see fig. 6.3(a)) or by performing PIV in a vertical section. The curving contour in the middle of fig. 6.3(a) via rheoscopic visualisation indicates the interface of a shear flow. It is noticed that this curving contour does not represent the amplitude of the forced mode, however, it does indicate that the forced mode has roughly an axial wavenumber  $k = 1$ , where the wavenumber  $k = 1$  means there are two half lobes in the vertical direction.



Due to the strong flow in the azimuthal direction, the tracing particles continuously pass through the vertical laser plane perpendicularly to the plane, therefore a PIV measurement on a vertical cross-section under the current setup is not able to provide a sufficiently accurate measure of the velocity field. Nevertheless, it is still a useful tool to qualitatively reveal the structure of the forced Kelvin mode on a vertical plane, see fig. 6.3(b). Apparently, the PIV measurement is consistent with the rheoscopic visualisation in fig. 6.3(a) and meanwhile achieves a good agreement with the linear prediction in fig. 6.3(c).

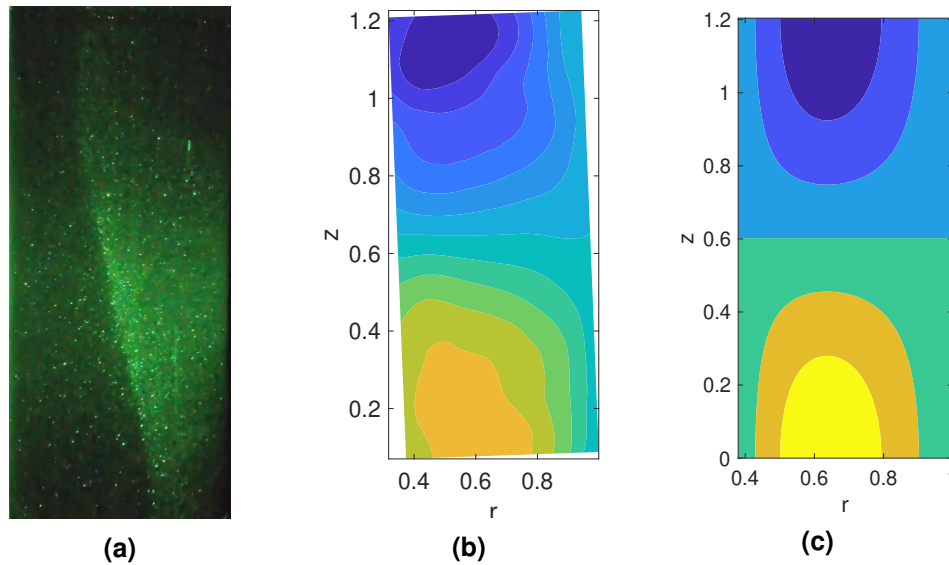


**Figure 6.3:** (a) Structure of the forced Kelvin mode visualised by Kalliroscope for  $h = 1.2$ ,  $Ek = 1.19 \times 10^{-5}$ ,  $Fr = 0.09$ ,  $\alpha \approx 1^\circ$ ; (b) PIV measurement and (c) linear solution of radial velocity field in a vertical section of frequency  $\omega = 1$  showing structure of the forced Kelvin mode for  $h = 1.2$ ,  $Ek = 2.38 \times 10^{-5}$ ,  $Fr = 0.02$ ,  $\alpha \approx 1^\circ$ .

In a system with a sufficiently small inclination angle or a non-resonant fluid depth, the system is in a marginally stable state. The forced Kelvin mode arises due to the periodic forcing and at the same time damped by the viscosity so that the amplitude of the forced mode keeps constant in this equilibrium state. The evolution of the mode amplitude in time is plotted in fig. 6.2(b) with the help of STFT, where  $A_0$  is the amplitude of the geostrophic mode, i.e. the mean flow, and  $A_1$  is the amplitude of the forced mode. In the rest of this chapter, the subscript of amplitude  $A$  and frequency  $\omega$  denotes the azimuthal wavenumber of the respective mode so that  $A_1$  represents the amplitude of mode  $m = 1$ . The time  $t = 0$  in the diagram does not represent the beginning of the rotation but the starting of the measurement, where the rotating system has been kept running for a time longer than  $400\Omega^{-1}$ . Comparing to the fluctuating  $A_0$ , the amplitude  $A_1$  is very

stable during the measurement.

For a precessing cylinder, when the rotation rate becomes close to a resonant frequency of the respective mode, even a weakly precessional forcing can excite a strongly amplified Kelvin mode [4]. Overcoming the viscous damping, a resonant collapse is triggered that the forced mode grows over-saturation and breaks down into small scale disorders accompanied by a sudden decrease of the amplitude of the forced mode. Under certain circumstances, e.g. a slow rotation rate, the degenerated flow field can be reorganised or relaminarized and show a smooth flow structure without completely suppressing the disorders. The reorganised flow passes through a secondary breakdown and enters a cycle of breakdown and relaminarization.

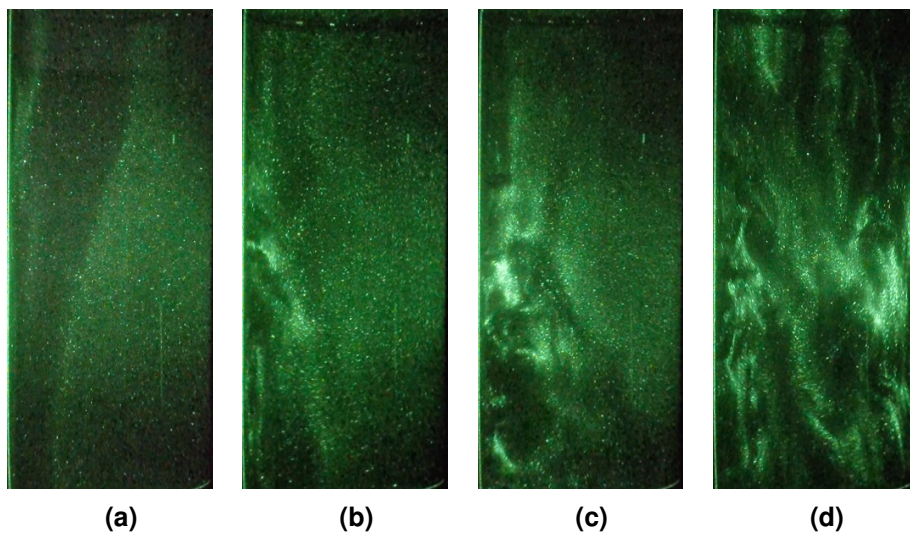


**Figure 6.4:** A sequence of photographs of a vertical cross section in the annulus showing the process of the resonant collapse for  $Ek = 1.19 \times 10^{-5}$ ,  $Fr = 0.09$  and water depth  $h = 1.2$ . The first photo (a) is taken at about 100 revolutions after starting rotation and the following photos are captured within 20 revolutions after (a). The left edge of the photograph represents the inner cylinder and the right edge the outer one.

The resonant collapse has been observed in the tilted rotating setup, as shown by a sequence of photographs in fig. 6.4, that a persisting laminar form (fig. 6.4(a)) abruptly degenerates into disorders (fig. 6.4(d)). In these photographs, left edges are the wall of the inner cylinder and right edges are the inner wall of the outer cylinder. In fig. 6.4(a), the fluid is in a laminar state and the forced mode with the radial and axial wavenumber  $n = k = 1$  is easily observed with illumination. The breakdown starts close to the inner cylinder, where a local disturbance appears, see fig. 6.4(b). The localized disorder moves with the crest of the forced mode and gradually expands to the whole annular gap (see fig. 6.4(d)) within 20 revo-

lutions. A further relaminarization can be observed for a low rotation rate, where the small scale disorders merge and the flow field becomes generally smoother compared with its most chaotic phase shown in fig. 6.4(d).

Despite the fact that in our experiment we have a rotating annulus instead of a cylinder, the picture shows good agreement with the photography of the elliptically excited inertial wave shown in Malkus [59] and the photographs of the classical precession experiment presented in Manasseh [78].

The resonant collapse in our experiment might be triggered by two types of instability: a parametric triadic instability and a shear-type instability. To excite either type of the instabilities, a resonant forced Kelvin mode is required. In the tilted rotating annulus, the forced Kelvin mode always has the angular frequency  $\omega = 1$ . A forced Kelvin mode is in resonance, if the frequency of the forced mode matches the eigenfrequency of the container for inertial modes. Since the eigenfrequency solely depends on the container's geometry, an advantage of the free surface system is that the aspect ratio can be easily controlled through changing the filling depth. Thus the rotating system allows being well-tuned to excite a resonant forced Kelvin mode in order to investigate the response of the fluid in a resonant regime.

**Table 6.1:** The eigenfrequency of the inertial modes with azimuthal wavenumber  $m = 1$  for  $h = 1.2$ .

$n$	$k$	$\omega_{mnk}$	$\xi_{mnk}$	$n$	$k$	$\omega_{mnk}$	$\xi_{mnk}$
1	1	0.995	4.579	2	2	0.942	9.824
2	1	0.529	9.564	1	3	1.696	4.912
1	2	1.474	4.820	2	3	1.241	9.941

The eigenfrequencies of inertial modes in a rotating annulus are calculated from the linear dispersion relation (33) and (34). Solving the equations for the forced Kelvin mode with the wavenumber  $m = n = 1$  and the forcing frequency  $\omega_f = 1$  gives the ratio  $h/k = 1.2$ . Several eigenmodes with  $m = 1$ ,  $h = 1.2$  and a low radial and axial wavenumber are listed in table 6.1. According to the dispersion relation, the frequency of the forcing  $\omega_f = 1$  is very close to the frequency of the eigenmode  $\omega_{111} = 0.995$  for a filling depth  $h = 1.2$ , i.e., the forced Kelvin mode is very close to resonance for this water depth. The space-time diagram in fig. 6.5, where the green pixels represent bright rheoscopic particles under the illumination of a green plane laser, illustrates temporal developments of a forced Kelvin mode with different filling depth ranging from 1.05 to 1.25. Similar to fig. 6.3(a), the wavy-edge shape of the bright zone in the middle does not directly represent

the amplitude of the forced Kelvin mode, however, a violent oscillating wavy shape does indicate a strong forced Kelvin mode. At  $h = 1.05$ , the wavy shape is clearly observed with the period equaling the rotation period of the cylinder. The amplitude of this wavy edge grows with the increasing filling depth. At  $h = 1.2$ , the forced mode matches with the eigenmode of the container and triggers a resonant collapse, where the forced mode breaks down and degenerates into small-scale instabilities. In this case, a clear wavy edge can no longer be observed. With deeper water ( $h = 1.25$ ), the forced mode is away from resonance and the amplitude decreases. The wavy edge can then be observed again.

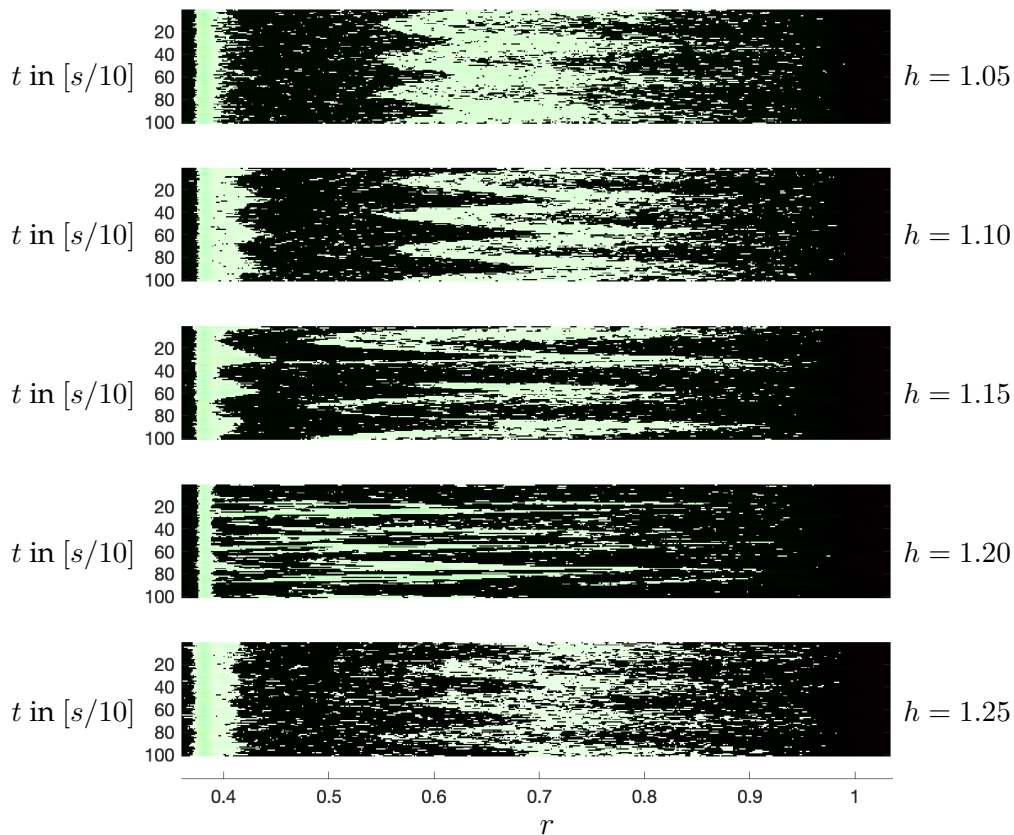


**Figure 6.5:** Space-time diagrams for experiments with different  $h$  and for  $\text{Ek} = 1.19 \times 10^{-5}$ ,  $\text{Fr} = 0.09$  indicating the resonant collapse for  $h = 1.2$ . x-axis: radius, left represents inner cylinder and right outer cylinder; y-axis: frame number (time in 0.1s). The bright pixels are the laser reflected by the Kalliroscope seeded in the water.

A series of PIV measurements are performed for different fluid depths, as plotted in fig. 6.6, showing the amplitude of the forced Kelvin mode varying with the filling depth for a constant Ekman number and inclination angle. The amplitude  $A_1$  is obviously higher for  $h = 1.2$ . In fact, the forced mode by  $h = 1.2$  has already reached its saturation limit and broke down before it grows to reach

a higher amplitude. Comparing with the linear theoretical prediction by (59) (the red curve in fig. 6.6), the amplitude at  $h = 1.2$  measured in the experiment is significantly lower than the inviscid theoretical result. On the other hand, the linear theory seems able to provide a reasonable prediction in mode amplitude for non-resonant cases.

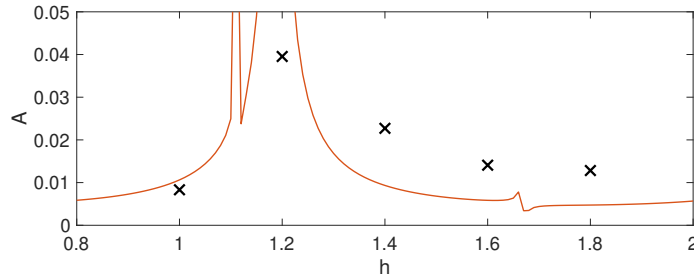


**Figure 6.6:** Amplitude of the forced Kelvin mode as a function of fluid depth  $h$  for  $Ek = 1.19 \times 10^{-5}$ ,  $Fr = 0.09$ ,  $\alpha \approx 1^\circ$  and measured at  $z = 0.75h$ . The red curve represents the linear theoretical prediction calculated from (59).

An alternative method to observe the resonant collapse is measuring the light intensity (intensity of grayscale) of the flow seeded with rheoscopic fluid. Figure 6.7 shows the light intensity sampled at the center of the annulus gap as a function of time  $t$ . The time  $t$  is scaled by  $\Omega^{-1}$ , and  $t = 0$  denotes the starting of the rotation. The absolute value of the light intensity has actually no clear physical meaning, however violently fluctuating magnitude in a single video indicates strongly unstable flow. For  $t < 110$  the light intensity fluctuates at a regular frequency with a relatively small amplitude, the flow is dominated by the forced Kelvin mode. The breakdown of the forced mode occurs at  $t \approx 110$ , after which the magnitude of the fluctuation grows significantly and the flow is no longer dominated by a single mode. Nevertheless, the increased fluctuation of the light intensity indicates only a more unstable flow, but not necessarily that the fluid velocity is increased.

During the constant rotation of the fluid in an unstable state, a typical cycle of inertial wave breakdown and relaminarization has been observed. An unstable flow can become stable within a certain period after the breakdown leading to a repetition of breakdown and relaminarization, as reported by McEwan [84], Thompson [110] and Manasseh [78]. Due to the limitation of the rotation rate of the current experimental facility, we are not able to prove whether for smaller  $Ek$  a sustained chaotic state exists, but given the similarity of our experiment with precessing cylinders, it is likely.

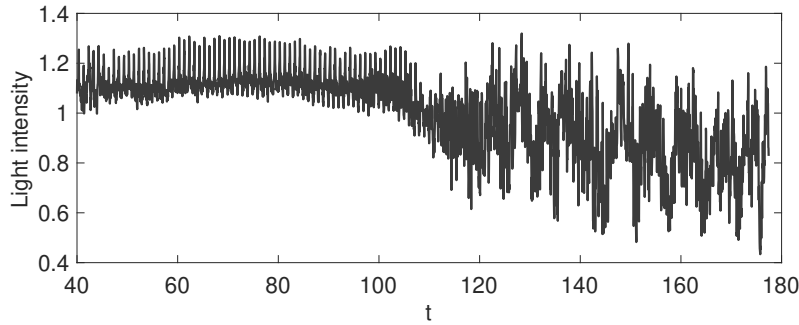


**Figure 6.7:** Light intensity measured in the middle of the gap at  $z = 0.75h$  for  $Ek = 1.19 \times 10^{-5}$ ,  $Fr = 0.09$ ,  $\alpha \approx 1^\circ$  and  $h = 1.2$ . The distance between two sharp peaks is equal to one period of the rotation.

## 6.4 The Geostrophic Mode

In a rotating fluid with inertial oscillations, a mean flow in the azimuthal direction, also referred to as steady stream in some contexts, exists due to Reynolds stresses. The mean flow is supposed to have a geostrophic structure, i.e. the mean flow is independent of the  $z$ -axis.

To verify the  $z$ -axis dependency, the average azimuthal velocity  $u_\theta$  departure from the solid body rotation is measured at different depths for  $\alpha = 1^\circ$  with a cover on the top of the annulus to avoid the possible disturb from the wind on the upper surface during rotation, see fig. 6.8. Each velocity profile is time-averaged over 200 revolutions and measured after a waiting time much larger than the Ekman time scale. The gray colour band is the standard deviation based on repeating the measurement at  $0.8h$  by completely restarting the experiment three times.

Apparently, the mean flow has a negative velocity with a U-shape profile that the fluid rotates slower than the container. The maximum magnitude of azimuthal velocity locates close to the inner cylinder. Note that due to the limitation of the PIV settings, the velocity in the boundary layer at the inner cylinder having a thickness of a few millimetres is unavailable. However, the turning point close to the inner cylinder (see black curve in fig. 6.8) might be caused by the Ekman pumping in the boundary layer. In general, the velocity profiles at different depths show good agreement, with only a small deviation with respect to  $z$ .

### 6.4.1 Influence of the wind effect

A common issue for the fluid in a rotating tank with a free surface is the wind effect. For an unclosed container, the air above the free surface does not co-rotate

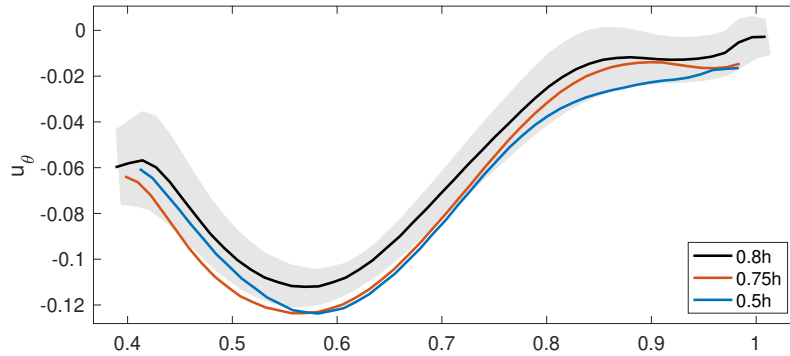


**Figure 6.8:** Illustration of time-averaged non-dimensional azimuthal velocity measured over 200 revolutions at different heights. The legend denotes the height of the laser plane from the bottom. Note that for  $0.8h$  we performed three measurements. The gray shading gives the standard deviation. The tank is tilted with angle  $\alpha \approx 1^\circ$ .  $Ek = 1.19 \times 10^{-5}$ ,  $Fr = 0.09$  and  $h = 1.2$ .

equally with the container. This velocity difference between air and water might slow down the surface water rotation and hence might influence the flow.

To verify the wind effect, experiments have been performed either with a lid at the top of the container or without any cover. The top lid forces the air in the gap to rotate uniformly with the container, thus eliminating the air drag on the water surface. Measurements are performed at the height of  $0.88h$  that are close to the surface and the time-averaged azimuthal velocity profiles are shown in fig. 6.9. The red dashed curve represents the profile with the cover on the top while the black solid curve is without cover. Both experiments are measured with the same  $Ek$  at the same position, and each case was repeated three times. Obviously, the fluid with the top cover has weaker retrograde flow, which proves that for the case with a small inclination angle  $\alpha$  the air torque is an important reason for the retrograde flow.

Nevertheless, the velocity close to the inner cylinder boundary still has an obvious deviation from zero, which implies another factor that influences the mean velocity profile. In fact, this profile is due to the nonlinear self-interaction of the forced mode mainly in the boundary layers.

#### 6.4.2 Influence of the inclination angle

With respect to a classical precession experiment, Kobine [61] states that the azimuthal flow results from the precessionally forced mode and an additional contribution related to nonlinear and viscous effects in the boundary layer. We think that for non-zero  $\alpha$  the mean flow is generated by a similar effect, except that



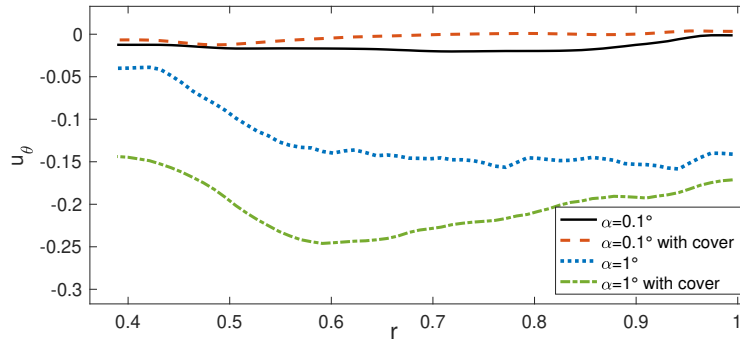


**Figure 6.9:** Illustration of time averaged non-dimensional azimuthal velocity in radial direction measured at  $0.88h$ , each of the dataset is averaged over 600 revolutions for  $Ek = 1.19 \times 10^{-5}$ ,  $Fr = 0.09$  and  $h = 1.2$ . Black solid line: Tank without cover,  $\alpha \approx 0.1^\circ$ ; red dashed line: tank with top cover,  $\alpha \approx 0.1^\circ$ ; blue dot line: tank without cover,  $\alpha \approx 1^\circ$ ; green cross line: tank with top cover,  $\alpha \approx 1^\circ$ . (All other figures in the article are with top cover.)

the normal mode is forced by a gravitational torque on the non-axisymmetric viscously rotating mass instead of precessional forcing. It can be anticipated from (85) that the forced mode is stronger by increasing  $\alpha$ . Hence the nonlinear effect is more pronounced for an increased  $\alpha$ , which contributes to a stronger geostrophic mode.

To show this we performed further experiments by increasing  $\alpha$  from  $0.1^\circ$  to  $1^\circ$ , as shown in fig. 6.9. The blue and green curves indicate the mean flow profile with increased  $\alpha$ . The significant difference between the experimental results for different tilt angles confirms our anticipation.

Nevertheless, referring to the mean flow profiles with  $\alpha \approx 1^\circ$ , the top cover also plays an important role, where the experiment without cover and hence with wind stress (blue curve in fig. 6.9) surprisingly has a significantly weaker retrograde flow than that with cover (green curve in fig. 6.9). A possible explanation is that the wind induced Ekman layer damps the motions. In the previous section, the eigenfrequency of the cylindrical annulus was calculated from inviscid equations given in Lin *et al.* [72], where the Ekman pumping is not considered. This pumping, however, leads to an exponentially decreasing velocity profile in the boundary layer, thus influences the effective aspect ratio for resonance [64], [73]. The study of Borcia *et al.* [15] about the inertial mode in a rotating annulus with librating side-wall boundaries shows that the Stokes layer can influence the effective volume inside the container and therefore change the resonance frequency. Hence, in our experiment, the Ekman layer can also influence the effective volume and leads to a detuning of the resonant frequency and consequently to a



weaker forcing.

### 6.4.3 Influence of the filling depth

Since the generation of the mean flow is directly related to the nonlinear interactions in the Ekman layer, the magnitude of the mean flow depends strongly on the nonlinearities in the rotating flow. When a forced mode is in resonance, the nonlinear interactions are stronger, thus give rise to an increased mean flow. Figure 6.10 shows the mean flow profile with different filling depths, where the magnitude of the mean flow is significantly higher for  $h = 1.2$  than for the other depths.

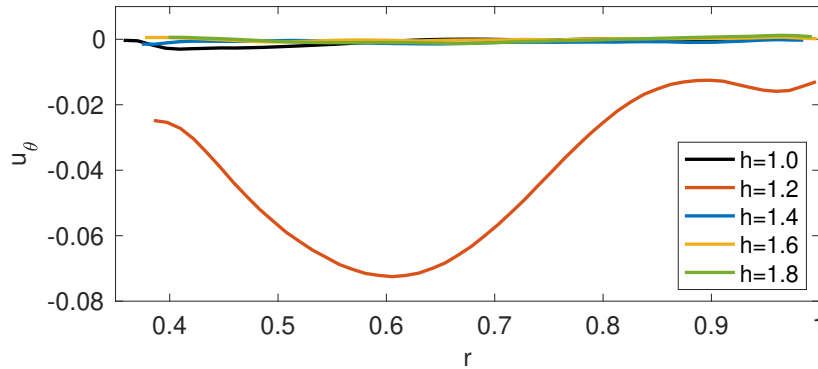


**Figure 6.10:** Mean azimuthal flow profile as a function of radius for different fluid depth  $h$  with  $Ek = 1.19 \times 10^{-5}$ ,  $Fr = 0.09$  and measured at  $z = 0.75h$ .

The strength of the non-zero mean flow is relevant for the instabilities in the rotating fluid where two types of instability can occur: a parametric triadic instability and a barotropic shear instability.

## 6.5 Triadic Instability

In the tilted rotating system, the directly forced Kelvin mode may become unstable via a parametric instability, in which two secondary free Kelvin modes are excited and interact with the forced mode. The triadic resonance requires three modes in a triad to satisfy the parametric condition:  $\omega_i \pm \omega_{\mp j} = \omega_1$ ,  $m_i \pm m_{\mp j} = m_1$  and  $k_i \pm k_{\mp j} = k_1$ , when the index 1 stands for the forced mode. This type of instability requires a sufficiently strong forced mode, which can be achieved by e.g. a perfectly tuned resonant depth or a large inclination angle when the forced mode does not match the eigenfrequency of the container perfectly.

The triadic instability can be easily identified from an amplitude spectrum, as can be seen in fig. 6.11. The diagram shows the amplitude spectra for three Ekman numbers, i.e.  $2.39 \times 10^{-5}$ ,  $1.19 \times 10^{-5}$  and  $7.96 \times 10^{-6}$ , with the same  $\alpha$  and  $h$ .

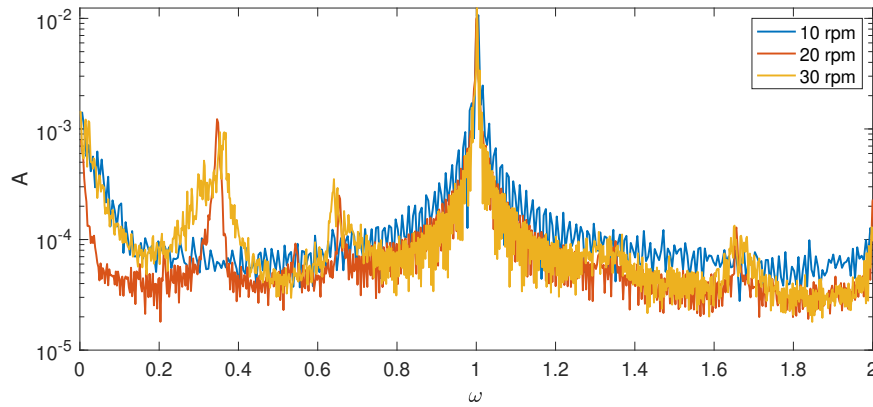


**Figure 6.11:** Amplitude spectrum for different Ekman numbers measured at  $z = 0.75h$  with  $\alpha = 0.1^\circ$  and  $h = 1.2$ . Ek are respectively  $2.39 \times 10^{-5}$ ,  $1.19 \times 10^{-5}$  and  $7.96 \times 10^{-6}$  for 10, 20, 30 rpm.

For  $Ek = 2.39 \times 10^{-5}$  (10 rpm), the rotating flow is dominated solely by the forced Kelvin mode with frequency  $\omega = 1$ . This forced mode, as shown previously in fig. 6.2(b), is balanced by the effect of the forcing and the viscous damping and remains a nearly constant amplitude during the measurement. Decreasing Ek, the effect of viscous damping decreases, which leads to the growth of the forced mode. When the amplitude of the forced mode  $A_1$  exceeds the saturation of viscosity, a resonant collapse will be induced which gives rise to two free Kelvin modes that form a triad with the forced mode. The sum of the frequencies of the two free modes,  $\omega = 0.3461$  and  $0.6537$  respectively for  $Ek = 1.19 \times 10^{-5}$  (20 rpm), equals the frequency of the forced mode. This process is captured with the help of STFT in fig. 6.12, where the two free Kelvin modes emerge at  $t = 80 - 130$  in fig. 6.12(a) accompanied with the decrease of  $A_1$  at  $t = 100 - 150$ . Figure 6.12(b) shows the growth of the free modes at an earlier time from  $t = 30$  and the two free modes exhibit different growth rates. It needs to be noticed that the forcing is introduced at the beginning of the spin-up, not after reaching a solid body rotation as in a typical precession experiment. Therefore the growth rate in the present experiment is not directly comparable with a growth rate based on solid body rotation.

To confirm the triadic relation for wavenumbers, the Kelvin modes are reconstructed by harmonic analysis and shown in fig. 6.13. The reconstructions present

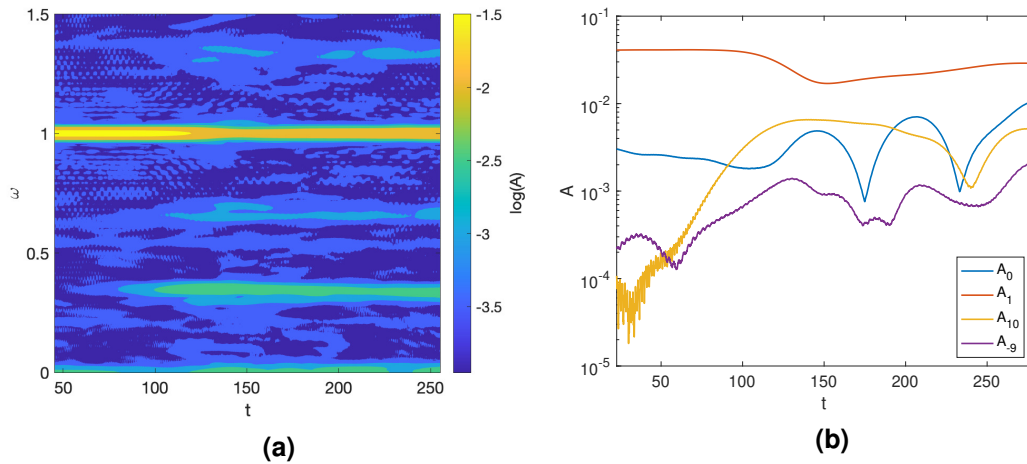


**Figure 6.12:** Temporal evolution of amplitudes for  $Ek = 1.19 \times 10^{-5}$ ,  $\alpha = 0.1^\circ$  and  $h = 1.2$ .

the vorticity fields of the prominent modes, i.e. the forced mode and the two free modes, for  $Ek = 1.19 \times 10^{-5}$ . Note that the figure is mainly for a qualitative understanding of the mode structure, therefore a colour bar is not provided and hence the same colour for different reconstructions does not imply the same vorticity magnitude.

As shown in fig. 6.13a and b, the two free Kelvin modes have azimuthal wavenumbers  $m = 10$  and  $-9$  respectively. The negative sign of the wavenumber indicates the wave propagates in the prograde direction, i.e. the opposite direction of the mean flow, and hence faster than the annulus rotation. Apparently, the azimuthal wavenumbers and the frequencies of the two free modes satisfy the rule for the triadic resonance that read  $m_{10} + m_{-9} = m_1$  and  $\omega_{10} + \omega_{-9} = \omega_1$ .

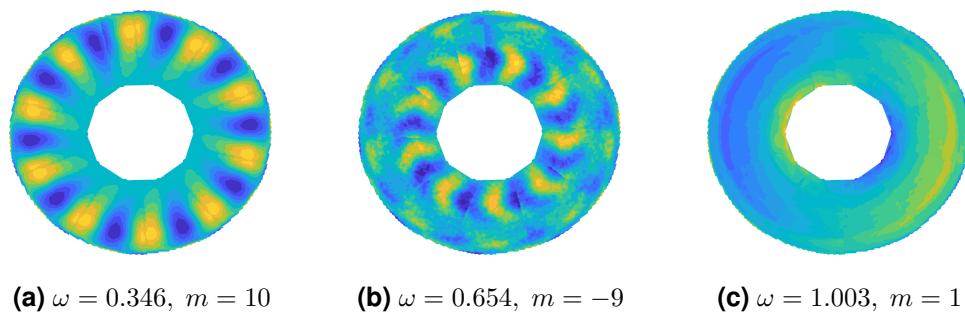


**Figure 6.13:** Reconstruction of Kelvin modes based on the vorticity field for  $h = 1.2$ ,  $Ek = 1.19 \times 10^{-5}$ ,  $Fr = 0.09$ ,  $\alpha \approx 0.1^\circ$ ,  $z = 0.75h$ . The colour represents the vorticity, where yellow (blue) indicates positive (negative) value of the vorticity.

Due to a strong mean flow in the azimuthal direction, accurate PIV data in a vertical section are not available for the free modes, the axial wavenumber of the free modes is in general not known from the horizontal PIV measurement. To

further verify the presence of triadic interactions, we applied a bispectral analysis (see sec. 5.5). Particularly in our case, time series from different grid points are included in the bispectra analysis and gives the bicoherence, which presents a statistical measure of quadratic phase coupling.

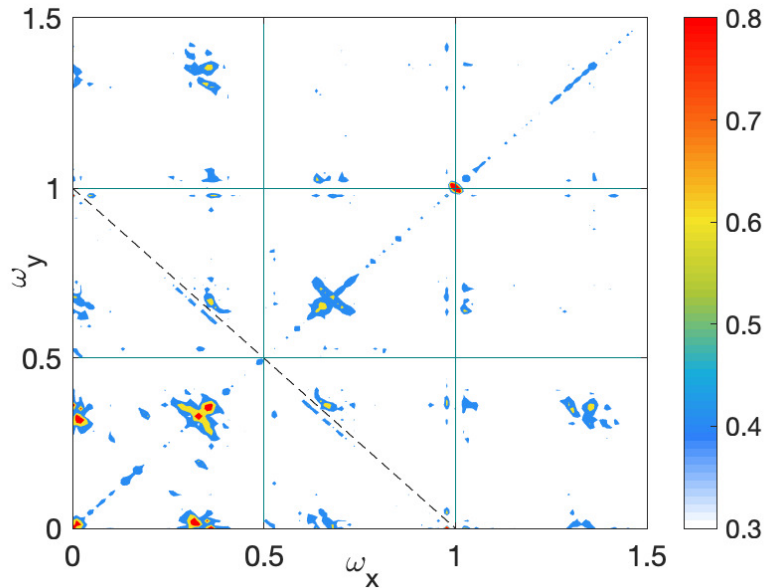


**Figure 6.14:** Bicoherence spectrum for  $\alpha \approx 0.1^\circ$ ,  $Ek = 1.19 \times 10^{-5}$ ,  $Fr = 0.09$  and  $h = 1.2$ .

Figure 6.14 shows the bicoherence for  $Ek = 1.19 \times 10^{-5}$  and  $\alpha \approx 0.1^\circ$  of the azimuthal velocity component. Note that a bicoherence of 1 represents a perfect triadic coupling of two modes and 0 means no coupling. The red spots in the diagram highlight the frequencies with strong bicoherence. The strong peaks on the line with  $\omega_x = \omega_y$  correspond to the self-correlation of the forced mode or the free modes. The diagram is symmetric with respect to the line  $\omega_x = \omega_y$ . Possible triads that resonate with the forced mode can be identified by connecting a line with slope  $-1$  between point  $(0, 1)$  and  $(1, 0)$ , the points with high correlation on this line reveals the components of the triads as  $\omega_x$ ,  $\omega_y$  and  $\omega_x + \omega_y$  [20]. Thus the mode pair of frequency  $(0.346, 0.654)$  form a triplet with the forced mode, which confirms that the mode  $m_{10}$  and  $m_{-9}$  are indeed free Kelvin modes generated due to resonant breakdown of the forced Kelvin mode.

The two free Kelvin modes in the triadic resonance are supposed to be equal or close to the solution of the linear dispersion relation (34). Tab.6.2 lists solutions with azimuthal wavenumber 10 and  $-9$  and low radial wavenumber, which suggests that the two free Kelvin modes have the wavenumbers  $(10, 1, 2)$  and  $(-9, 2, 1)$ . However, the frequencies show no perfect match indicating that the

triad is not precisely tuned. This in fact corresponds to a typical scenario of a triadic resonance.

**Table 6.2:** The eigenfrequency of the inertial modes with azimuthal wavenumber  $m = 10$  and  $-9$  for  $h = 1.2$ .

m	n	k	$\omega_{mnk}$	$\xi_{mnk}$	m	n	k	$\omega_{mnk}$	$\xi_{mnk}$
10	1	2	0.699	13.993	-9	1	1	0.376	13.637
10	2	2	0.558	17.962	-9	2	1	0.294	17.557
10	3	2	0.468	21.691	-9	3	1	0.243	21.327

This resonant triad can be identified from a diagram of dispersion relations between the frequencies  $\omega$  and the axial wavenumbers  $k$  for the two free Kelvin modes, see fig. 6.15. The diagram is plotted in a similar way as done by Albrecht *et al.* [4], in which the curves are shift vertically and horizontally according to the frequency and the axial wavenumber of the forced mode respectively. A cross in such a diagram, as marked by the blue circle in fig. 6.15, indicates the modes that in a resonant triad with the forced Kelvin mode. In this case, the resonant modes are  $(10, 1, 2)$  and  $(-9, 2, 1)$ .

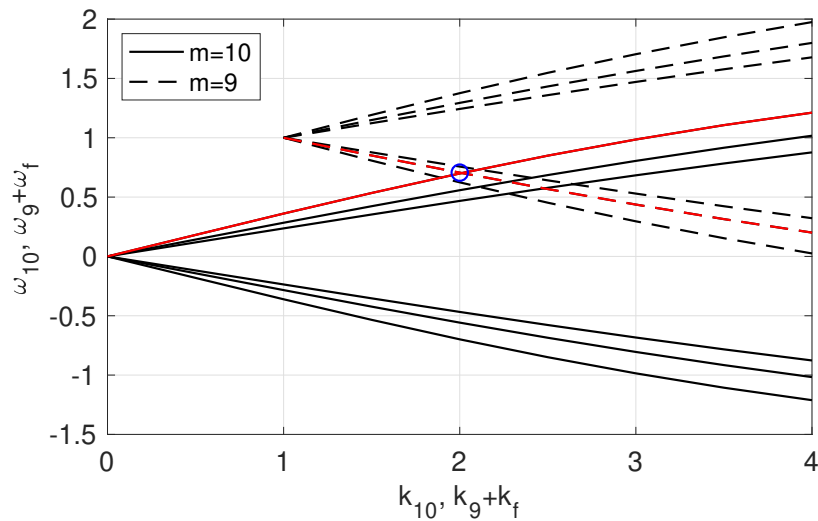


**Figure 6.15:** The dispersion relations showing the frequencies  $\omega$  and the axial wavenumbers  $k$  of two free Kelvin modes for azimuthal wavenumbers  $m_9$  (dashed lines) and  $m_{10}$  (solid lines). For each wavenumber, upper/lower branches are for prograde/retrograde modes in the rotating frame and the lines successively represent  $n = 1, 2, 3$  from the outer to inner side. The blue circle marks the resonant triad with the forced mode, where the frequency of the Kelvin mode  $(-9, 2, 1)$  is equal to the frequency of the Kelvin mode  $(10, 1, 2)$ .

## 6.6 Shear Instability

Due to the presence of a strong non-zero mean flow, i.e. the geostrophic mode, a shear-type instability might be triggered. Fundamentals of this instability are introduced in the previous section 2.8. In the tilted rotating system, a geostrophic mode with a large amplitude is generated due to strong nonlinear interactions. The geostrophic mode gives rise to a barotropic shear mode, which interacts with the forced Kelvin mode and results in the generation of further modes that fulfill triadic relations with the shear mode and the forced mode.

The shear instability requires a sufficiently strong mean flow, which is produced with a large inclination angle ( $\alpha = 1^\circ$ ) and a resonant fluid depth ( $h = 1.2$ ). With the help of STFT, the onset of the shear instability is captured and shown in fig. 6.16 for  $Ek = 1.59 \times 10^{-5}$ ,  $\alpha = 1^\circ$  and  $h = 1.2$ . The figure presents the evolution of amplitudes as a function of time after a very short spinning up time for  $45\Omega^{-1}$ . The barotropic mode, which has a wavenumber  $m = 3$  and frequency  $\omega = 0.146$  in this case, grows from  $t = 30$ , see fig. 6.16(b), with its amplitude increases by two orders. Shortly after the emergence of  $m_3$ , a second mode with frequency  $\omega = 2\omega_3$  arises and has a similar growth rate as mode 3. This mode has the azimuthal wavenumber  $m = 6$  and is considered as a harmonic mode of mode 3. The amplitude of the forced mode  $A_1$  drops down at  $t = 50 - 70$  after a continuous rise for  $t < 50$ , this might be in accordance with the overshooting and breakdown of an oversaturated forced mode.

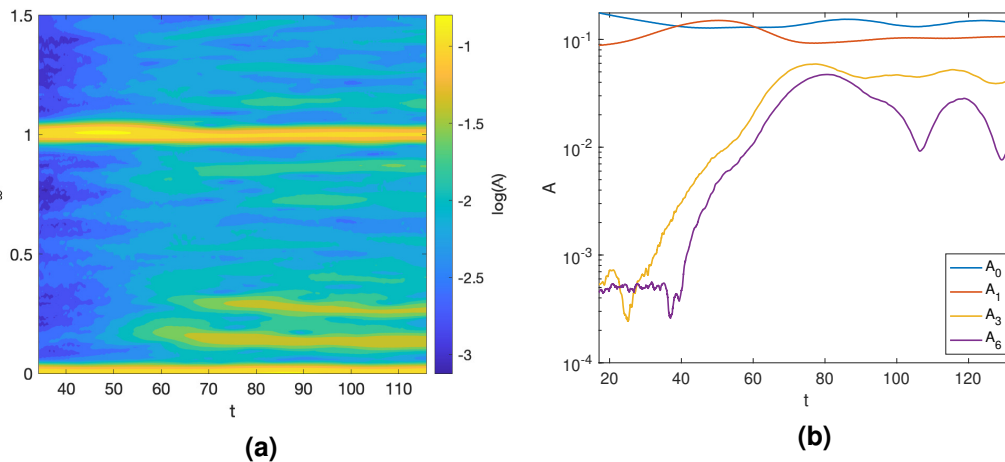


**Figure 6.16:** Temporal evolution of amplitudes for  $Ek = 1.59 \times 10^{-5}$ ,  $\alpha = 1^\circ$  and  $h = 1.2$ .

The distribution of the modes in frequency domain is acquired from the amplitude spectrum for  $Ek = 1.19 \times 10^{-5}$ , see fig. 6.17, with the structures of the respective modes shown in fig. 6.18, which is presented in a similar way as fig.

6.13. In this case the barotropic mode has an azimuthal wavenumber  $m = 3$  and a frequency  $\omega_3 = 0.162$  with its harmonic mode  $m = 6$  and  $\omega_6 = 2\omega_3 = 0.327$ . Several less prominent free modes are identified from the spectrum. Their frequencies and wavenumbers, according to the reconstructions in fig. 6.18, satisfy the triadic relation with  $m_1, m_3$  and  $m_6$ :

$$m_3 + m_{-2} = m_1, m_4 - m_3 = m_1, m_6 + m_{-5} = m_1,$$

$$\omega_3 + \omega_{-2} = \omega_1, \omega_4 - \omega_3 = m_1, \omega_6 + \omega_{-5} = m_1.$$

Beside the triadic interactions between the forced mode, the barotropic modes and the free modes, we noticed such relations also exist even without the participation of the forced mode, e.g.  $m_6 + m_{-2} = m_4, m_3 + m_{-5} = m_{-2}$ ,

$$\omega_6 + \omega_{-2} = \omega_4, \omega_3 + \omega_{-5} = \omega_{-2}.$$

This might indicate a further step of the energy cascade, that the energy transfers from a less prominent mode to a secondary mode through the triads.

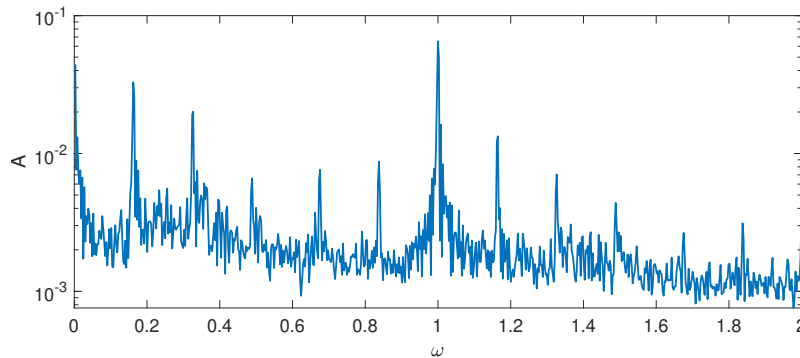


**Figure 6.17:** Amplitude spectrum for  $Ek = 1.19 \times 10^{-5}$ ,  $\alpha = 1^\circ$ ,  $h = 1.2$  and  $z = 0.8h$ .

The triadic interactions are confirmed by the bicoherence spectrum in fig. 6.19, where we see the mode pair of frequency  $(0.162, 0.838)$  form a triplet with the forced mode. The red spot at  $(0.162, 0.162)$  on fig. 6.19 suggests a strong self-interaction of the  $m_3$  mode, which gives rise to the  $m_6$  mode. This  $m_6$  mode also interacts with the forced mode in the triplet  $(0.327, 0.676, 1.003)$ . Furthermore, similar triplets can be found for the modes with frequency  $(0.838, 0.327)$  and  $(1.003, 0.162)$  with mode  $\omega = 1.165$  as well as the triplet  $(0.162, 0.676, 0.838)$ , which indicates the presence of strong nonlinear interactions between the modes.

An essential question with respect to the shear-type instability is whether the low-frequency  $m_3$  mode is a barotropic mode or not. The low frequency of  $m_3$  suggests that this mode is unlikely a Kelvin mode, since the eigenfrequencies for Kelvin modes with wavenumbers  $(3, 1, 1)$  and  $(3, 2, 1)$  are respectively 0.799 and 0.485, which is far away from  $\omega_3$ .

Although a PIV on a vertical plane is not sufficiently reliable for giving an ac-



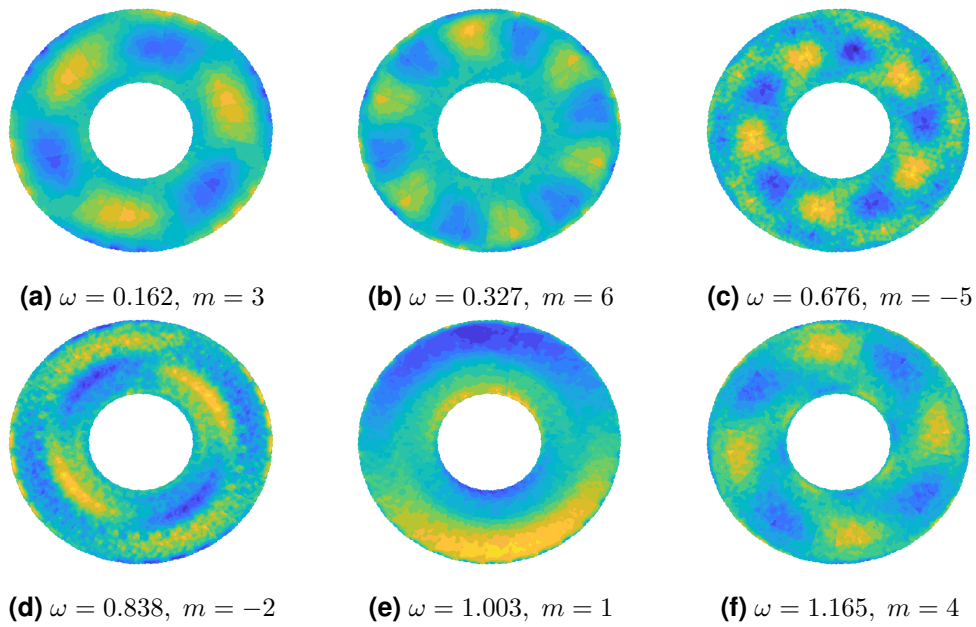


**Figure 6.18:** Reconstruction of wave modes based on the velocity field for  $h = 1.2$ ,  $\text{Ek} = 1.19 \times 10^{-5}$ ,  $\text{Fr} = 0.09$ ,  $\alpha \approx 1^\circ$ ,  $z = 0.8h$ . The colour represents the vorticity, where yellow (blue) indicates positive (negative) value of the vorticity.

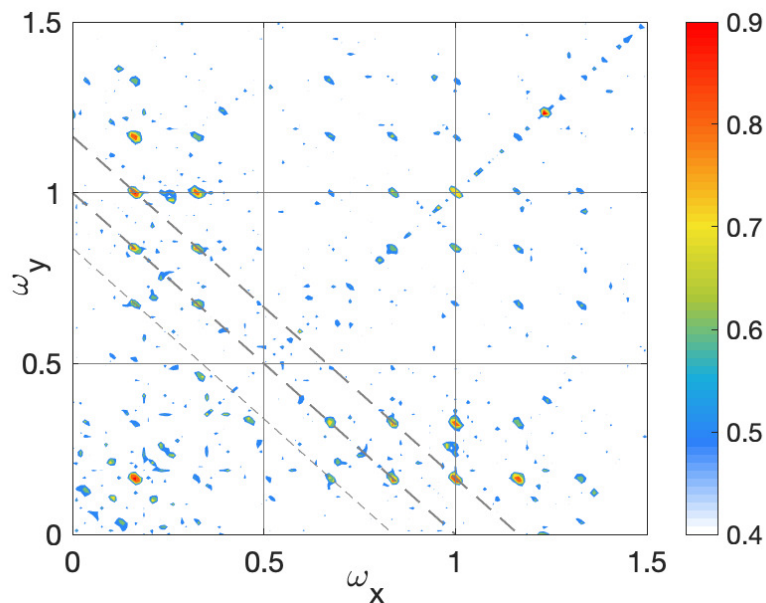


**Figure 6.19:** Bicoherence spectrum for  $\alpha \approx 1^\circ$  with  $\text{Ek} = 1.19 \times 10^{-5}$ ,  $\text{Fr} = 0.09$  and  $h = 1.2$ .



curate measurement of the flow velocity, it is possible to use PIV to simply show the structure of the modes in the vertical direction. Such results are presented in fig. 6.20 only for a qualitative understanding of the flow structure in the radial-axial plane. Despite the imperfect match in frequencies, we consider the mode with  $\omega = 0.159$  being identical to  $m_3$  in fig. 6.18 and the mode  $\omega = 1.165$  as the mode  $m_4$ . Figure 6.20 confirms the relation of the three modes in axial direction that  $k_4 - k_3 = k_1$ .

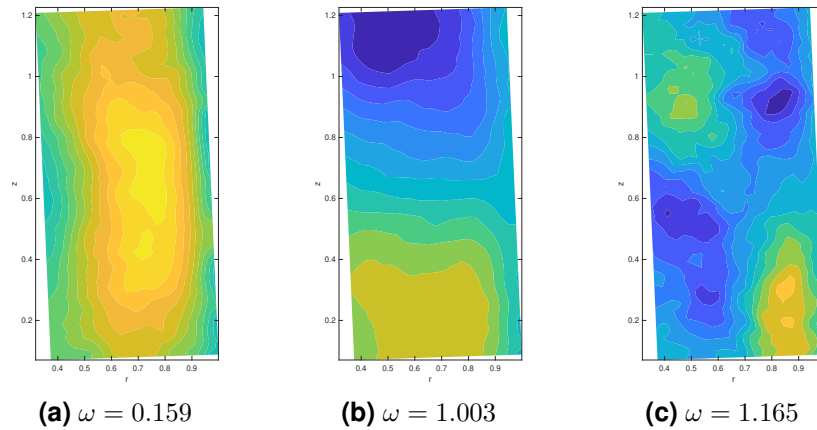


**Figure 6.20:** Radial velocity field of modes with frequencies (a) 0.159, (b) 1.003 and (c) 1.165 from PIV on a vertical plane for  $h = 1.2$ ,  $Ek = 1.19 \times 10^{-5}$ ,  $Fr = 0.09$ ,  $\alpha \approx 1^\circ$ . The yellow colour represent a positive radial velocity and blue is negative.

The axial wavenumber of  $m_3$  and  $m_4$  is further verified by performing a series of PIV measurement at different positions in vertical direction for different values of the Ekman number, as shown in fig. 6.21. Figure 6.21(a) shows mode amplitudes  $A_0$ ,  $A_1$  and  $A_3$  measured at two different  $z$  as a function of  $Ek$ . As is known previously, the geostrophic mode has an axial wavenumber  $k = 0$  so that the amplitude  $A_0$  is invariant with  $z$ , whereas the forced mode has  $k = 1$  so that  $A_1$  at  $z = 0.75h$  is larger than  $A_1$  at  $z = 0.5h$ . The distributions of  $A_0$  and  $A_1$  in fig. 6.21(a) achieve an excellent agreement with this fact that  $A_0(z = 0.75h) = A_0(z = 0.5h)$  for all Ekman numbers while  $A_1(z = 0.75h) > A_1(z = 0.5h)$ . The amplitudes of mode 3, as indicated with red marks in fig. 6.21(a), show no obvious dependency on  $z$  and indeed confirms our assumption that the mode 3 has a barotropic structure, i.e.  $k = 0$ .

The amplitudes of mode 2 and 4 are presented in fig. 6.21(b). Both of the modes form a triplet with mode 1 and mode 3. Their amplitudes  $A_{-2}$  and  $A_4$  have distinguished magnitudes at  $0.75h$  and  $0.5h$  that  $A(z = 0.75h) > A(z = 0.5h)$  for  $A_{-2}$  and  $A_4$  except for  $Ek = 7.95 \times 10^{-6}$ , where the Ekman number is small and the sys-

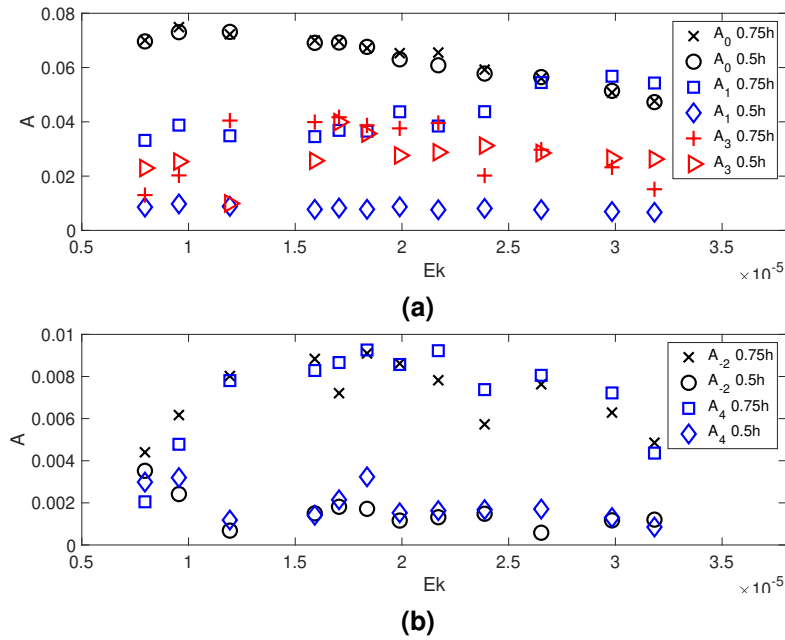


**Figure 6.21:** Amplitudes of modes (a)  $A_0, A_1, A_3$  and (b)  $A_{-2}, A_4$  as a function of  $Ek$  measured at different  $z$  for  $h = 1.2$  and  $\alpha \approx 1^\circ$ .

tem is more unstable. This result agrees with fig. 6.20(c) that the axial wavenumbers of mode 2 and 4 satisfy the triadic relation:  $k_3 + k_{-2} = k_1, k_4 - k_3 = k_1$ .

A similar shear instability as the one described above has been reported by Herault *et al.* [52] where a low-frequency mode resulted from a destabilized azimuthal mean flow in a precessing cylinder. Herault *et al.* further related this instability to the theoretical prediction by Kerswell [59] that the dominant geostrophic mode interacts with the forced mode and gives rise to two subdominant Kelvin modes. The frequencies of the two sub-dominant Kelvin modes are equal to the linear combination of the forced mode and the geostrophic mode, which explains the presence of the triplets  $(m_1, m_3, m_{-2})$  and  $(m_1, m_3, m_4)$  in our experiment.

Repeating the experiment for shear instabilities, we noticed a bifurcation in the azimuthal wavenumber of the barotropic mode. Instead of a barotropic mode with an azimuthal wavenumber 3, the shear instability excites a  $m = 4$  mode with its structure shown in fig. 6.22(a). With a higher wavenumber, the frequency of this mode is also increased from 0.162 to 0.195 (see fig. 6.18). Meanwhile, since the excitation of the other modes is related to the barotropic mode, frequencies and wavenumbers of the other modes are also changed corresponding to the barotropic mode. To keep the text concise, in the following we still refer to the barotropic mode as  $m_3$ .

As discussed in this section, the shear instability is excited due to the velocity

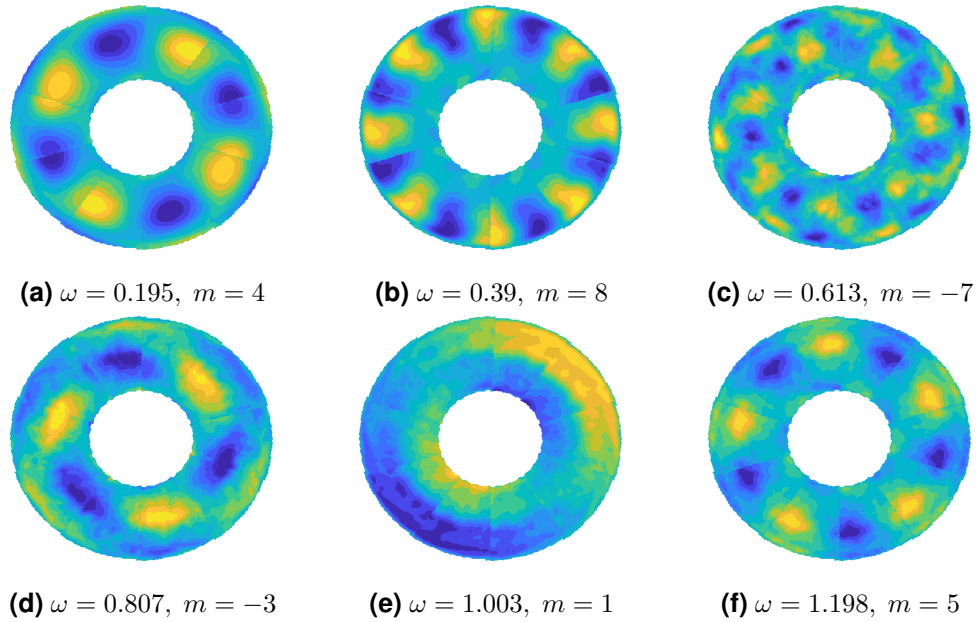


**Figure 6.22:** Reconstruction of wave modes based on the velocity field for  $h = 1.2$ ,  $\text{Ek} = 1.19 \times 10^{-5}$ ,  $\text{Fr} = 0.09$ ,  $\alpha \approx 1^\circ$ ,  $z = 0.75h$ . The colour represents the vorticity, where yellow (blue) indicates positive (negative) value of the vorticity.

gradient of the shear flow. On the other hand, the instability can be suppressed by properly manipulating the velocity gradient. A benefit of the annulus container is that the rotation rate of the inner and outer cylinder can be controlled individually. By slowing down the rotation rate of the inner cylinder so that  $\Omega_i/\Omega_o < 1$ , we are able to modify the profile of the background flow, as shown in fig. 6.23. As can be seen from the diagram, a slight differential rotation does not have much influence on the velocity profile. A significant modification of the velocity profile is observed for  $\Omega_i/\Omega_o \leq 0.85$ , where the velocity gradient  $du/dr$  is constantly negative for  $r < 0.8$ .

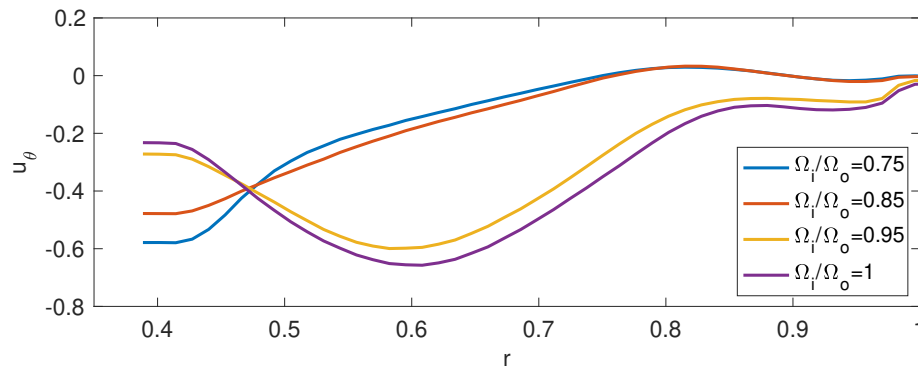


**Figure 6.23:** Azimuthal mean flow profile for differential rotation with  $\text{Ek} = 1.19 \times 10^{-5}$ ,  $\text{Fr} = 0.09$  and  $h = 1.2$ .

According to the amplitude spectra presented in fig. 6.24, the shear instability

has been suppressed by the artificially modified mean flow profile. The peaks excited by shear instabilities (fig. 6.24(c) and 6.24(d)) are no longer visible with stronger differential rotations (fig. 6.24(a) and 6.24(b)).

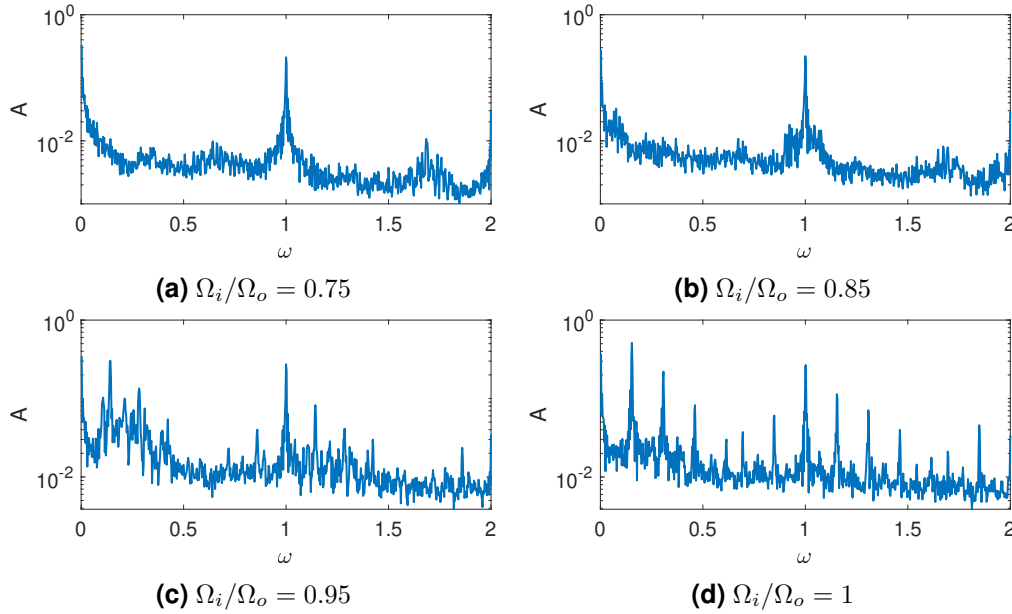


**Figure 6.24:** Amplitude spectrum of differential rotation with  $Ek = 1.19 \times 10^{-5}$ ,  $Fr = 0.09$  and  $h = 1.2$ .

## 6.7 Doppler Shift

We noticed the dependency of the mode frequencies on the Ekman numbers for  $\alpha \approx 1^\circ$ . Figure 6.25 shows the variation of the mode frequency with  $Ek$  ranging from  $2.39 \times 10^{-5}$  to  $7.96 \times 10^{-6}$ . For the reader's convenience, we multiplied each two neighboring energy spectra by a factor of  $10^5$ . Obviously, we find similar peaks according to the energy spectra for the given  $Ek$  and the harmonic analysis indicates that the wavenumbers corresponding with the peaks are invariant of  $Ek$  for  $2.39 \times 10^{-5} \leq Ek \leq 7.96 \times 10^{-6}$ . On the other hand, the frequencies of the peaks vary with  $Ek$ . The frequency of the  $m_3$  mode constantly increases with the decrease of  $Ek$ , meanwhile the frequencies of the other modes changes respectively so that the linear relation of the mode frequencies is robustly sustained during the considered range of  $Ek$ . The frequencies of the free modes are plotted in fig. 6.26(a) for a broader range of  $Ek$ . The frequency of mode  $m_3$  increases from a very low frequency (0.066) to 0.189 when  $Ek$  decreases from  $3.2 \times 10^{-5}$  to  $7.9 \times 10^{-6}$ , whereas mode  $m_2$ , which fulfills the relation  $\omega_3 + \omega_{-2} = \omega_1$ , shows a contrary tendency.

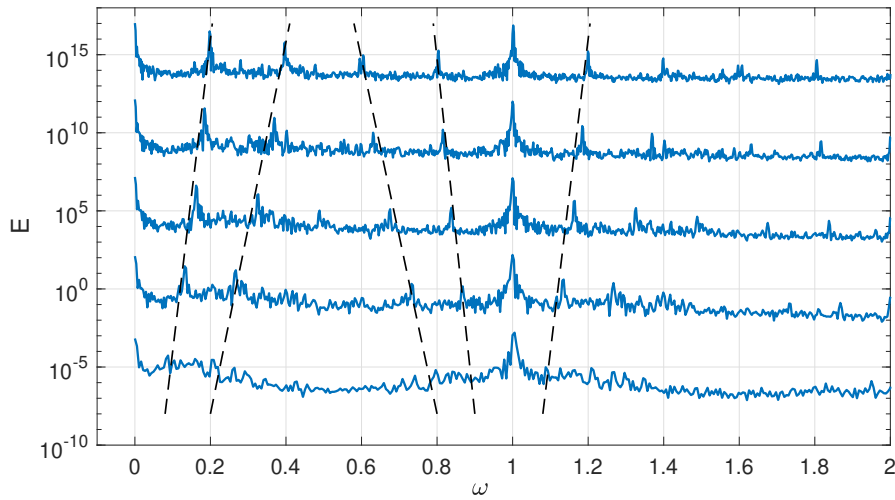


**Figure 6.25:** Non-dimensional kinetic energy spectrum at different angular velocity measured at  $0.8h$  with  $\alpha \approx 1^\circ$ . The curves in the diagram from bottom to top represent respectively  $E_k = 2.39 \times 10^{-5} - 1.59 \times 10^{-5} - 1.19 \times 10^{-5} - 9.55 \times 10^{-6} - 7.96 \times 10^{-6}$ . To separate the curves in y-direction, a factor of  $10^5$  is multiplied for the visualisation. The black dashed line indicates the frequency variation of the respective mode with  $E_k$ .

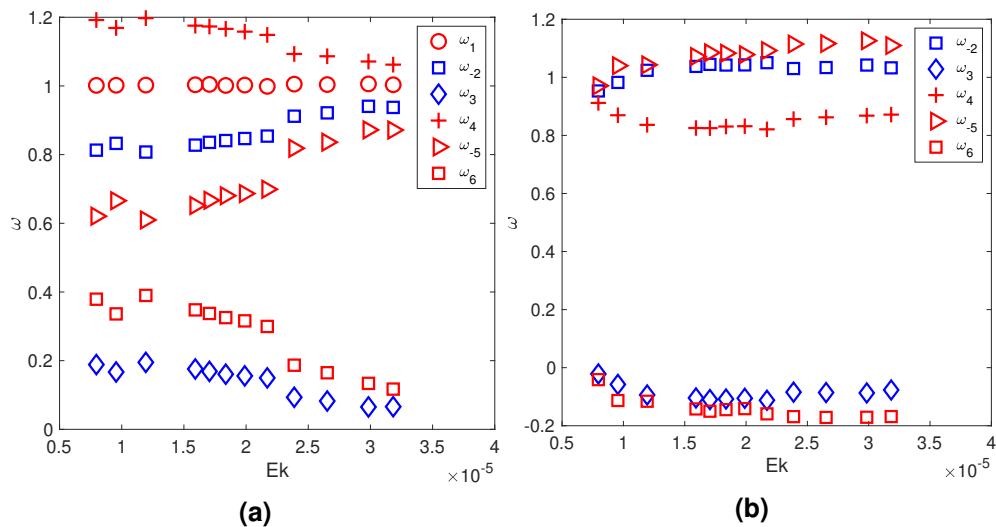


**Figure 6.26:** Frequency distribution of the respective mode as a function of  $E_k$  at  $0.75h$  for  $h = 1.2$ . (a) measured frequency; (b) frequency corrected by the Doppler effect.

Since the camera system is fixed with the rotating frame, the influence of the Doppler effect on the measured frequency should be considered due to the presence of the mean flow in the azimuthal direction. An Ek-dependent frequency change was observed by Hoff *et al.* [54] when investigating inertial modes of spherical Couette flow. A frequency shift of the triad was discovered after the transition from a weakly turbulent regime to a regular-inertial-mode regime. The authors attributed the frequency shift to the abrupt change of the mean flow through regime transition.

The shift of the frequency caused by the Doppler effect is estimated by

$$\Delta\omega = \Delta\Omega_\theta m = \frac{U_\theta}{R_o} m, \quad (87)$$

where  $\Delta\omega$  is the frequency change for different Ekman numbers,  $m$  is the non-dimensional azimuthal wavenumber and  $U_\theta$  is the mean azimuthal velocity in the rotating frame [54].

By considering the Doppler effect, the corrected intrinsic frequency as a function of Ek is plotted in fig. 6.26(b). Generally speaking, the Doppler effect provides a reasonable correction to the frequency variation that reduces the change of the mode frequencies with regard to the Ekman numbers.

## 6.8 Mode Amplitude

The amplitudes of the modes, which is defined as  $A_m = (u_{\theta,m}^2 + u_{r,m}^2)^{1/2}$ , are plotted as a function of Ek in fig. 6.27 for  $7.79 \times 10^{-6} < \text{Ek} < 3.18 \times 10^{-5}$ .

It must be noticed that the measured amplitude is not necessarily equal to the real amplitude of the mode due to the complex wave structure in the vertical direction. However, assuming the vertical structure of the respective mode keeps constant for different values of Ek, the relative size of the mode amplitude can be measured using data at a single depth.

For small Ek, the viscosity can be ignored in the interior of the rotating flow, however, this term has to be considered close to the boundary due to the presence of the Ekman layer. The nonlinear and viscous theory developed by Meunier *et al.* [88] shows that the mode amplitude is saturated by the viscous or the nonlinear effects or both. For high Ekman numbers, the mode amplitude is saturated by the viscous boundary layers and scales as  $\text{Ek}^{-1/2}$ . With the decrease of the Ekman number, the saturation due to the nonlinear effects becomes stronger and eventually dominant. Specifically, the nonlinear effects lead to the generation

of the geostrophic mode, which in fact plays an important role in saturating the amplitude of the Kelvin modes. In fact, this mean flow related saturating effect is more significant than the saturation due to the nonlinear self-interaction of Kelvin modes.

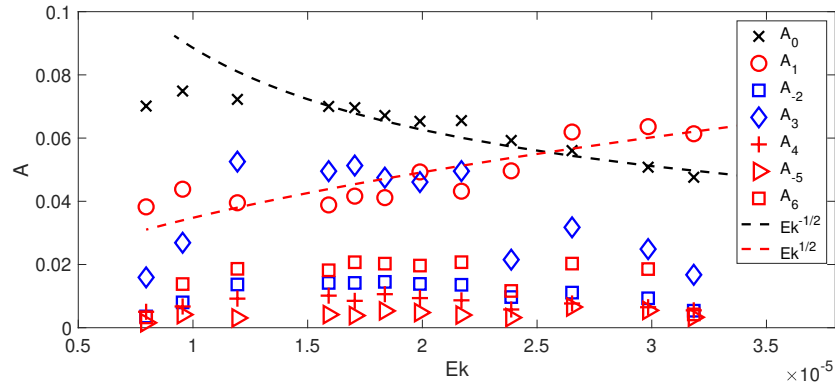


**Figure 6.27:** The mode amplitude as a function of  $Ek$  at  $0.75h$ ,  $h = 1.2$ .

In our experiment, the amplitude of the mean flow  $A_0$  (black crosses in fig. 6.27) gets larger with decreasing  $Ek$ , whereas the forced mode  $A_1$  (red circles in fig. 6.27) shows the opposite trend. The red and black dashed curves denote the scaling  $Ek^{1/2}$  and  $Ek^{-1/2}$  respectively. The presence of the free Kelvin modes indicates that the rotating fluid is in a nonlinear regime. This implies a possibly weaker viscous saturation comparing with the saturation due to the nonlinear effects. The change of  $A_0$  as a function of  $Ek$  suggests a strong dependency on the nonlinear effects on the Ekman number. For lower  $Ek$ , the nonlinear effect becomes stronger, promotes the generation of the mean flow and therefore increases the saturation effect on the forced mode.

## 6.9 Low-Order Amplitude Equation

A weakly nonlinear model has been developed by Lagrange *et al.* [64] to describe the flow which couples the forced Kelvin mode to two free Kelvin modes and a geostrophic mode in a classical precessing cylinder. For the Ekman numbers of our experiment, this model shows irregular and possibly chaotic dynamics. However, we know that this is not the common route to turbulence for rotating fluids. On this route not a single triad becomes chaotic but a cascading process leads to more and more triads and eventually to wave chaos [20]. From fig. 6.19 we have learnt that this process has started in our experiment. However, the single triad model by Lagrange *et al.* [64] is still useful to understand certain

aspects of the flow in our experiment.

In this weakly nonlinear model, the evolution of the geostrophic mode amplitude is given by

$$\frac{\partial A_0}{\partial t} = \text{Ek}^{1/2} \left( -\frac{2}{h} A_0 + \chi_2 |A_2|^2 + \chi_3 |A_3|^2 \right), \quad (88)$$

where  $A_0$ ,  $A_2$  and  $A_3$  are respectively the amplitude of the geostrophic mode and two free Kelvin modes and  $\chi_2$  and  $\chi_3$  are tuning constants. The first term on the right-hand-side represents the viscous damping of the geostrophic mode and the second and third terms represent the nonlinear self-interaction of the two free Kelvin modes driving the geostrophic mode. This equation suggests that the generation of the mean flow is due to nonlinear self-interactions of the excited Kelvin modes and meanwhile damped by the viscous effects. The geostrophic mode grows slowly in time since it is  $O(\text{Ek}^{1/2})$  smaller than  $O(A_0)$ , which creates a delay between the growth of the free modes and the geostrophic mode.

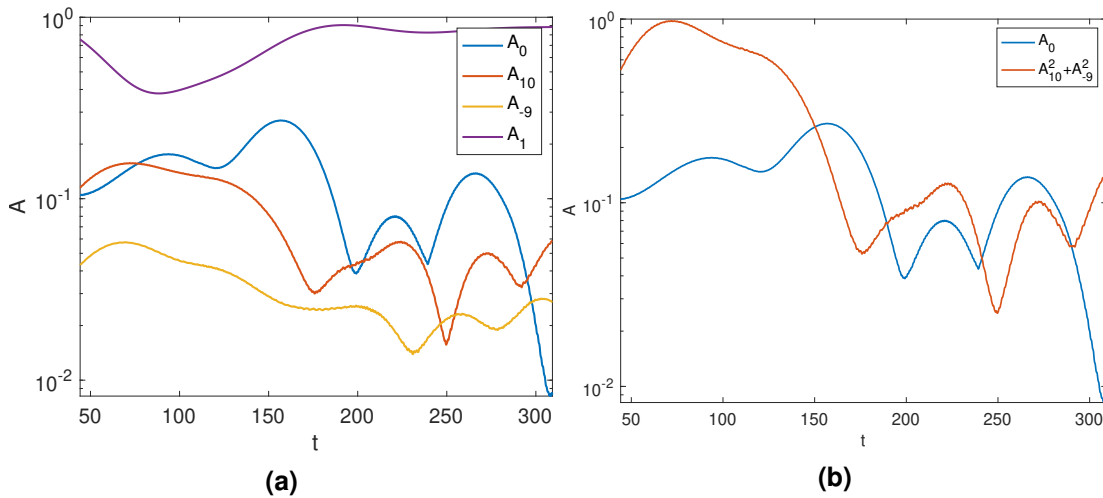


**Figure 6.28:** (a) Amplitude of the modes and (b) comparison between  $A_0$  and  $\chi(A_{10}^2 + A_{-9}^2)$  ( $\chi = 35$ ) as a function of the dimensionless time  $t$  for  $\alpha = 0.1^\circ$ . The data are measured at  $0.75h$  with  $\text{Ek} = 7.95 \times 10^{-6}$ ,  $\text{Fr} = 0.09$  and  $h = 1.2$ .

Figure 6.28(a) shows the evolutions of amplitudes of the geostrophic, the forced and the free Kelvin modes as a function of time for the experiment with the triadic resonance, i.e.  $\alpha = 0.1^\circ$  and  $\text{Ek} = 7.95 \times 10^{-6}$ .

Temporal evolutions of amplitudes of the free Kelvin modes  $A_{10}$ ,  $A_{-9}$  and the geostrophic mode  $A_0$  exhibit a similar pattern in fig. 6.28(a). According to (88), we further compare the temporal evolution of  $A_0$  and  $\chi(A_{10}^2 + A_{-9}^2)$ , where  $\chi = 35$ , see fig. 6.28(b). A high correlation can be seen between the evolutions of  $\chi(A_{10}^2 + A_{-9}^2)$  and the geostrophic mode.



Comparing this to triadic instabilities, wave interactions in a shear instability seem to satisfy triadic relations in a similar way. Therefore we attempt to simply fit the weakly nonlinear model to the scenario of shear instabilities. Temporal evolutions of the mode amplitudes are shown in fig. 6.29(a) for  $\alpha = 1^\circ$  and  $\text{Ek} = 1.19 \times 10^{-5}$ . The geostrophic mode, the blue curve in fig. 6.29(a), shows only a rather weak fluctuation in time (i.e. a small standard deviation). In fact the ratio between the data based  $\frac{\partial A_0}{\partial t}$  and  $\text{Ek}^{1/2}$  is in the order  $10^{-2}$ , i.e.  $\frac{\partial A_0}{\partial t} \ll \text{Ek}^{1/2}$ . Assuming  $\chi_2$  equals  $\chi_3$  in (88), in a dynamical system with slow varying  $A_0$  ( $\frac{\partial A_0}{\partial t} / \text{Ek}^{1/2} \ll 1$ ),  $A_0 / (|A_2|^2 + |A_3|^2)$  should remain nearly constant so that  $(-\frac{2}{h}A_0 + \chi_2 |A_2|^2 + \chi_3 |A_3|^2)$  is close to 0.

For (88) this means that the ratio between  $A_0$  and  $|A_2|^2 + |A_3|^2$  should be close to a constant. Obviously, for our experiment not only two free modes are excited. The  $\text{Ek}$  in our case is more than one order of magnitude smaller and the flow is closer to a turbulent state than the one observed by Lagrange *et al.* [64]. However, their model, heuristically fitted to our case, is still useful in understanding some characteristics of wave interactions. Hence, we try to extend (88) by introducing nonlinear self-interactions of all the prominent modes except the forced Kelvin mode. In this case, it is expected that  $A_0 / \sum |A_{free}|^2$  remains nearly constant in time. Figure 6.29(b) shows the ratio between  $A_0$  and a number of squared amplitudes as a function of dimensionless time. It can be seen that indeed  $A_0 / \sum |A_{free}|^2$  is nearly constant. In contrast, just using one triad leads to stronger variations (red curve).

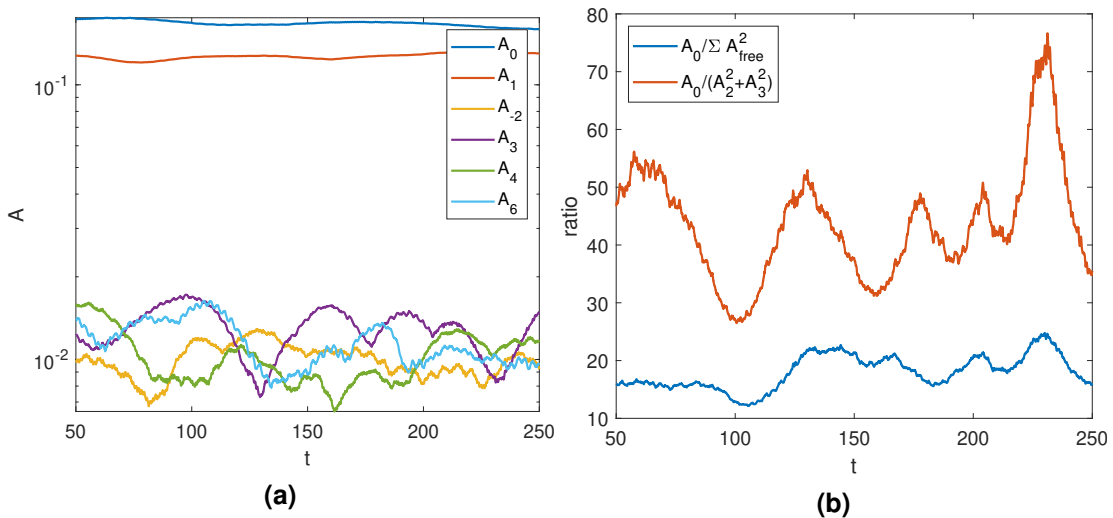


**Figure 6.29:** (a) Amplitude of the modes and (b) ratios between  $A_0$  and nonlinear effects of different modes as a function of the dimensionless time  $t$ . Measured at  $0.8h$  with  $\alpha = 1^\circ$ ,  $\text{Ek} = 1.19 \times 10^{-5}$ ,  $\text{Fr} = 0.09$  and  $h = 1.2$ .

**Table 6.3:** The ratio of  $A_0/\Sigma |A_{free}|^2$  for different Ek from experimental data measured at  $0.8h$  and  $A_0/\Sigma_{i=1}^2 |A_{free}|^2$  from the model by Lagrange *et al.* [64] (at the fourth row) but for  $Ro = 30Ro_L = 30\Omega_p \sin \alpha / (\Omega + \Omega_p \cos \alpha)$ , where  $\Omega_p$  is the precession frequency,  $h = 1.2$ ,  $\chi = 0.003\chi_L$ , where the index L denotes the values used by Lagrange *et al.* [64].

$Ek (\times 10^{-5})$	2.39	1.59	1.19	0.955	0.796
$A_0/\Sigma  A_{free} ^2$	33.82	24.28	28.02	24.98	21.25
$A_0/\Sigma_{i=1}^2  A_{free} ^2$	18.18	18.03	18.25	17.85	17.50

Another information from (88) suggests, that since  $h$  and  $\chi$  are independent of Ek, the ratio  $A_0/\Sigma |A_{free}|^2$  should also not depend on Ek. This ratio taken from the experimental data as well as the numerical runs is compared in table 6.3. The second row in the table is from the experimental measurements at  $0.8h$  and the third row shows the numerical result from the model by Lagrange *et al.* [64] when all the parameters are kept fix but the ones given in the caption are adapted to our model. This means that we use  $h$  and Ek from our experiment. Note that the forcing in our experiment is stronger since in contrast to the precession experiment there is no small Poincaré number in the forcing term (see (83) and (85)). We used a value for  $Ro$  that is 30 times larger than the one by Lagrange *et al.*. The tuning parameter  $\chi$  was adapted in the following way: from fig. 6.29(b) we read off the constant for  $A_0/\Sigma |A_{free}|^2$ . Then we determined  $\chi$  by  $\chi = \frac{2}{h} A_0/\Sigma |A_{free}|^2$ , which gives a  $\chi$  that is a factor  $3 \times 10^{-3}$  smaller than the value by Lagrange *et al.* [64]. Note again that the experimental measurements give the amplitude of the modes at a certain depth, which might not necessarily be equal to the mode amplitude when we would have access to the full axial structure of the mode. However, we only compare the dependency of  $A_0/\Sigma |A_{free}|^2$  with respect to Ek, the magnitude of this ratio is not relevant here.

Although, as discussed in the previous section, we find a disagreement between our free surface and the classical precessing experiment, namely that the strength of the nonlinear effects is influenced by Ek in our case, the experimental results reveal that  $A_0/\Sigma |A_{free}|^2$  depends only very weakly on the Ekman numbers, which is consistent with the weakly nonlinear model designed for the precessing cylinder [64]. Therefore this analysis confirms, that for the tilted rotating annulus with a free surface, the nonlinear self-interaction of the free Kelvin modes becomes stronger for decreasing Ek and implies an increase of mean flow amplitude. This amplitude increase is such that the ratio  $A_0/\Sigma |A_{free}|^2$  remains constant.

## 6.10 Discussion and Conclusion

A series of experiments have been performed to investigate the mode interaction in a tilted rotating annulus with a free surface. In the experiments, two modes play a major role in the dynamics: a forced Kelvin mode, which is driven by the gravitational torque on the non-axisymmetric viscously rotating mass, and a geostrophic mode, i.e. a mean flow, generated by nonlinear wave-wave interactions. Free Kelvin modes and shear modes are given rise by instabilities of the forced mode and the geostrophic mode, respectively.

Due to the inclination of the annulus, a forced Kelvin mode with wavenumber  $m = n = k = 1$  and frequency  $\omega = 1$  is excited. The amplitude of the forced Kelvin mode grows rapidly when the mode is close to an eigenmode of the annulus. Once the amplitude of the forced mode exceeds a threshold value, the mode becomes oversaturated, breaks down and leads to a resonant collapse as described for the precessing cylinder experiment by McEwan [84] and Manasseh [78]. Two well-tuned subdominant free Kelvin modes are excited during this process and form a triad with the forced Kelvin mode. This corresponds to a typical scenario of the triadic resonance.

Besides the parametric triadic instability, we also observed a shear-type instability that is related to the non-zero mean flow, i.e. the geostrophic mode. The experimental result confirms, that similar to the precessing cylinder experiment carried out by Kobine [61], the mean flow increases with the tilt angle  $\alpha$  (see (85)). For a sufficiently strong mean flow, a shear-type instability is excited and gives rise to a low-frequency barotropic shear mode. This shear mode interacts with the forced Kelvin mode and generates two free Kelvin modes that satisfy the triadic relation with the shear mode and the forced mode.

Shear instabilities in a partially filled and tilted rotating full cylinder have been studied by Thompson [110], who presented a theoretical prediction of the instability bounds. Following Thompson, we predicted the bounds of the shear instability for our experiment with annular geometry and experimentally verified the existence of the shear instability for different aspect ratios (fluid depths). The result is shown in fig. 6.30. The shaded areas represent shear instabilities calculated from (59) and the shade at  $H/R = 1.2$  is the first resonance corresponding to (61). The symbols show the number of triads we find experimentally in the frequency range  $0 < \omega \leq 1$ . In this range, the most prominent triads can be found.

The open circle indicates that more than one triad emerges, where the shear instability not only induced a low-frequency geostrophic mode  $m_3$  but also its har-

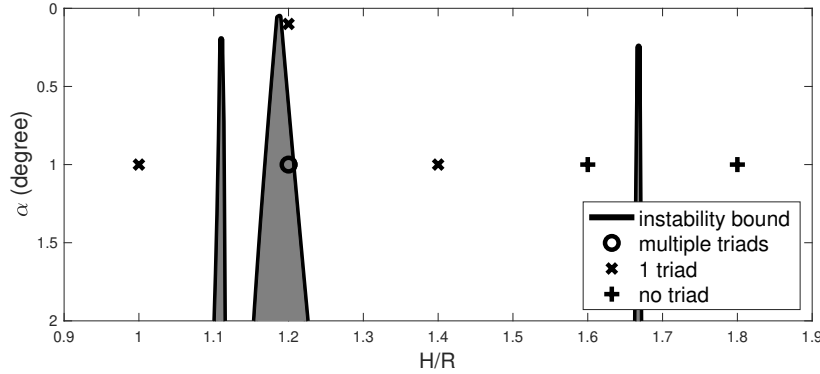


**Figure 6.30:** Theoretical prediction of the shear instability in the annulus for  $Ek = 1.19 \times 10^{-5}$  and  $Fr = 0.09$ . The symbols show whether mode triads exist for  $0 < \omega \leq 1$  from experimental results. The figure should be compared with figure 4 by Thompson [110].

monic mode  $m_6$ , as discussed in section V. Both modes interact with the forced Kelvin mode and give rise to additional free Kelvin modes. The shear instability necessitates a sufficiently strong mean flow, which requires a large forcing, e.g. large inclination angle of the annulus. A resonant fluid depth helps to strengthen the mean flow by a coupling to free modes. On the other hand, when the forcing is weak ( $\alpha = 0.1^\circ$ ) and hence the nonlinearly driven shear flow is too weak for becoming unstable, the forced Kelvin mode can still become unstable due to resonance, e.g. when  $H/R$  is close to 1.2 (see the cross above  $H/R = 1.2$  in fig. 6.30). As shown by crosses in fig. 6.30, if  $H/R$  is close enough to the resonance depth (e.g. for  $H/R = 1$  or  $H/R = 1.4$ ), a triadic resonant instability occurs and induces two free Kelvin modes satisfying the triadic relation with the forced Kelvin mode. Finally, if we are outside the depths for shear instability and too far away from the resonant depth, only the forced mode can be observed.

We further observed that the Ekman number has a prominent impact on the frequencies of the excited modes, except the frequency of the forced Kelvin mode. The frequencies of the retrograde modes increase with decreasing  $Ek$ , whereas the frequencies of the prograde modes have an opposite trend. The Doppler shift due to the strong background flow is found to be mainly responsible for this behaviour. A recent paper by Herault *et al.* [52] also points out that the non-zero background flow modifies the dispersion relation and thus detunes the frequency of Kelvin modes.

In fact, our experiment exhibits some similar characteristics when compared to the precessing cylinder experiment by Herault *et al.* [52], where they reported the presence of the parametric triadic resonance as well as a low-frequency barotropic

mode interacting with the forced Kelvin mode. Moreover, in our experiment with a free surface, a higher harmonics of the barotropic shear mode has been noticed that is also part of the triads with the forced mode.

The bicoherence spectrum further confirms triadic interactions between the modes and reveals also triads between three free Kelvin modes for the multiple triad case. We also attempt to connect the low-order dynamical system by Lagrange *et al.* [64] to our data. Although in our case more modes are active than contained in the low-order model, we could confirm that the geostrophic mode is balanced by a forcing due to self-interacting free modes and viscous damping. In future work, we will try to better adapt the dynamical system to our experiment so that we could have a simple tool for understanding the nonlinear interactions between the excited modes and to find thresholds for regime transitions.

Aside from the common phenomena that have been observed in classical precession experiments, we also observed some remarkable characteristics that deviate from what has been found in the precession setups. For example, in our experiment the amplitudes of the forced Kelvin mode and the geostrophic mode are saturated mainly due to the nonlinear effects. For the classical precession setup, theoretical and experimental results show that nonlinear effects are independent of the Ekman numbers. However, our experiment shows that the nonlinear effects significantly depend on  $Ek$  which seems to scale roughly with  $Ek^{-1/2}$  (see the red dashed curve in fig. 6.27). The nonlinear dependency further influences the amplitude of the mean flow and the saturation of the forced Kelvin mode.

Presently, our experiments are conducted within a relatively narrow range of Ekman numbers and a fixed inclination angle, which leaves plenty of space for further explorations. The existence of a free surface introduces extra complexity to the rotating system. Nevertheless, it is useful for further study, since it provides a convenient approach to investigate wave interactions and the influence of the aspect ratio on resonance. As suggested by Meunier [87], the open surface rotating cylinder might also be important for technical applications. This system might improve bioreactors since mixing due to the resonant collapse is much less destructive than mixing with rotating blades.

## 6.11 Outlook

To further explore the mode excitation in the rotating annulus, experiments with a modified bottom, as shown in fig. 6.31, have been planned and performed. The bottom has an inner and outer radius of 7.6/19.9 cm, a height of 9 cm and the angle

of the slope is  $36.19^\circ$ . On the upper side of the bottom irregularly distributed a number of screw holes, which are used for installing small obstacles on the surface of the bottom to produce small scale disturbances. Beside these screw holes, there are two smaller size screw holes for pull-down or pull-up the bottom block in the container.

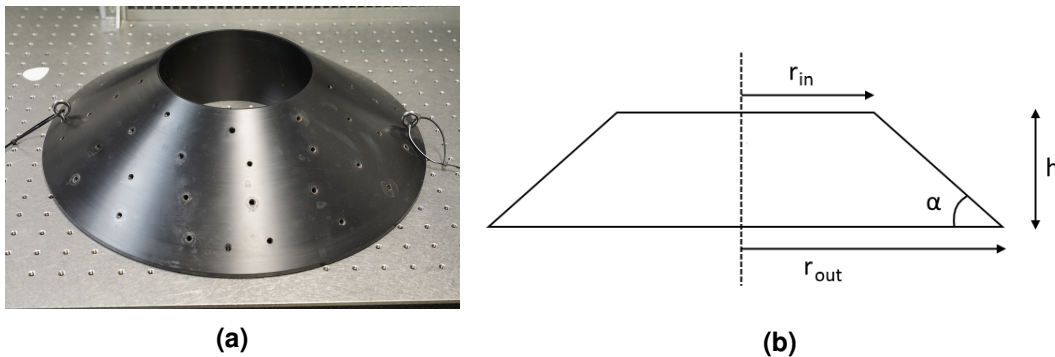


**Figure 6.31:** (a) Photography of the extended slope bottom and (b) a sketch showing its geometry

With the extra bottom, the closed container is indeed equipped with a sloping wall, the oscillating gravitational torque will thus generate an inertial beam. The beam reflects at the inner wall of the closed container. At certain fluid depth, the inertial wave ray is confined in a closed path and forms wave attractors. Figure 6.32 shows the different behaviour of the inertial wave with the help of Kalliroscope and EOF. For a normal closed annulus, as shown in fig. 6.32(a), the trapped inertial wave forms a global inertial mode. With the slope at the bottom, see the left-hand side of fig. 6.32(b), the inertial wave is emitted from the corner in the form of wave beams. This inertial wave ray can be numerically computed using a ray-tracing code and shown in the right-hand side of fig. 6.32(b).

A similar phenomenon has been experimentally observed in the early investigation by McEwan [84], where inertial waves were excited by an inclined top plate rotates relative to the cylinder. Inertial beams can be observed at particular filling depth when a resonant inertial mode was not excited. The numerical study by Lopez and Marques [74] suggests that the retracing beams have a stabilizing effect on the forced mode. With the beams retracing themselves, it appears that the symmetric breakdown of the forced mode is delayed by the nonlinear and viscous interactions with the forced mode to a much higher rotation rate.

In our experiment, we did observe that a resonant collapse requires a higher rotation rate with the same filling depth  $h = 1.2$  as in previous sections. However, this might be also related to a different resonant condition due to the change of

container geometry. Further investigations are needed to draw a conclusion.

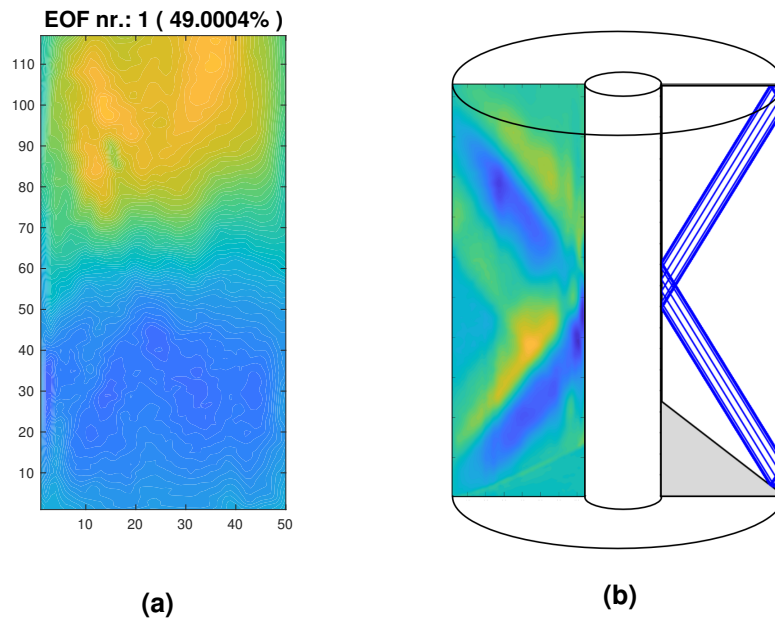


**Figure 6.32:** The first EOF component of light intensity of a r-z plan for (a) the normal annulus and (b) the annulus with the extended slope bottom. On the right hand side of (b) is a numerical ray-tracing result of the wave attractor.





## 7 Undular Bores in a Circular Channel

### 7.1 Introduction

A tidal bore is a natural tidal phenomenon in which the leading edge of an incoming tidal forms a series of waves propagating upstream in the estuarine zone of a river or a narrow bay against the direction of the river's or the bay's current. Tidal bores are usually formed during the flood tide in spring or autumn and have been observed in over 400 river estuaries in all continents except Antarctica. Representative rivers with tidal bores are e.g. Baie du Mont Saint Michel in France, Colorado River in Mexico and Qiantang River in China [24].

Tidal bores have wave heights ranging from tens of centimetres to as high as 5 to 9 metres under some conditions. Although they are usually weaker and less destructive than Tsunamis, their periodic occurrence (twice a day for semi-diurnal tidal bores) can lead to unpredictable developments near the riverbank, such as the transfer of sediments, as well as strong influences on the fishery in the river estuary.

A photograph in fig. 7.1 shows one of the world's largest bore, the Qiantang River tidal bore in China, which is resulted from the funnelling of the flood tidal wave into Hangzhou Bay and is formed twice a day. The tidal bore that occurs in spring causes waves is usually ranging from 1 to 3 m, with a maximum height of about 4 m, and travels upstream along the river to a distance of exceeding 100 km at a speed of 20 – 30 km/h [95]. Due to the human deaths caused by the tidal bore, a large number of tidal bore warning signs have been erected on the river banks [70].



**Figure 7.1:** A photography showing the tidal bore flows upstream (i.e. from right to left in the photo) on China's Qiantang River by Michael Greshko from National Geographic [48].

Field measurements of tidal bores have been extensively performed in the past years, such as the ones performed on Qiantang River [55], [70] and on Garrone

River at different locations like Podensac or Arcins channel [58], [81]. On the other hand, despite the importance of the bore collision for the suspended sediment transport, bedload, scour and erosion, the collision of tidal bores has been observed in a small number of rivers only due to the special conditions for occurrences. This phenomenon occurs for special local river geometry where the flow of the incoming flood tide has been split and remerged. An example is the Garonne River, which splits into two branches near Arcins. A “backward bore” is produced when the tidal bore approaches to the end of the main channel, propagates backward in the Arcins channel and collides with the forward propagating bore, as presented in fig. 7.2. For further records of bore collisions the reader might refer to Keevil *et al.* [58].

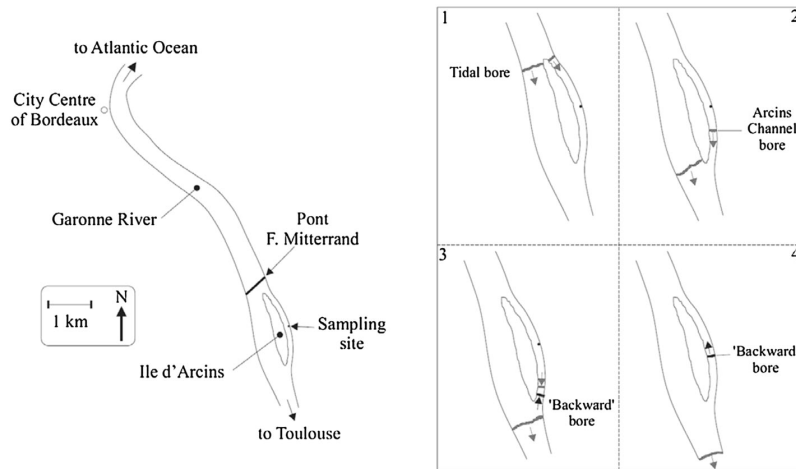


**Figure 7.2:** Plan view showing the collision of the tidal bore in Arcins channel on 19 October 2013, reprinted from Keevil *et al.* [58].

According to visual observations and free-surface measurements, several flow patterns are identified and characterized by the tidal bore Froude number, which is defined as

$$Fr_b = \frac{V_0 + U}{\sqrt{gD_0}} \quad (89)$$

where  $U$  denotes the absolute propagation speed of the wavefront referred to the channel bank,  $g$  is the gravity acceleration,  $D_0$  and  $V_0$  are the initial steady flow depth and velocity. For  $Fr_b < 1$ , the tidal wave is not able to form a tidal bore; for  $1 < Fr_b < 1.5$  to  $1.8$ , the undular bore is formed by a propagating front followed with a train of well-formed, quasi-periodic undulations; for  $Fr_b > 1.5$  to  $1.8$ , a breaking tidal bore is produced that the bore front shows a breaking roller associated with air entrainment and turbulent mixing [23].

In a long open channel, undular bores occur when a constant mass flux is fed

into the channel filled with water which is stationary initially. The bores propagate as a train of changed water level [26], [66], [107], [112]. Similar to solitary waves, the travelling wave train slowly depends on time [13]. Undular bores produced by a submerged line source or sink were first modelled by Sozer and Greenberg using a vortex sheet method, where they traced the nonlinear evolution of the free surface and explored the possible existence of steady-state solutions [106]. Positive bores are induced by source flows whereas negative bores by sink flows, see fig. 7.3(a).

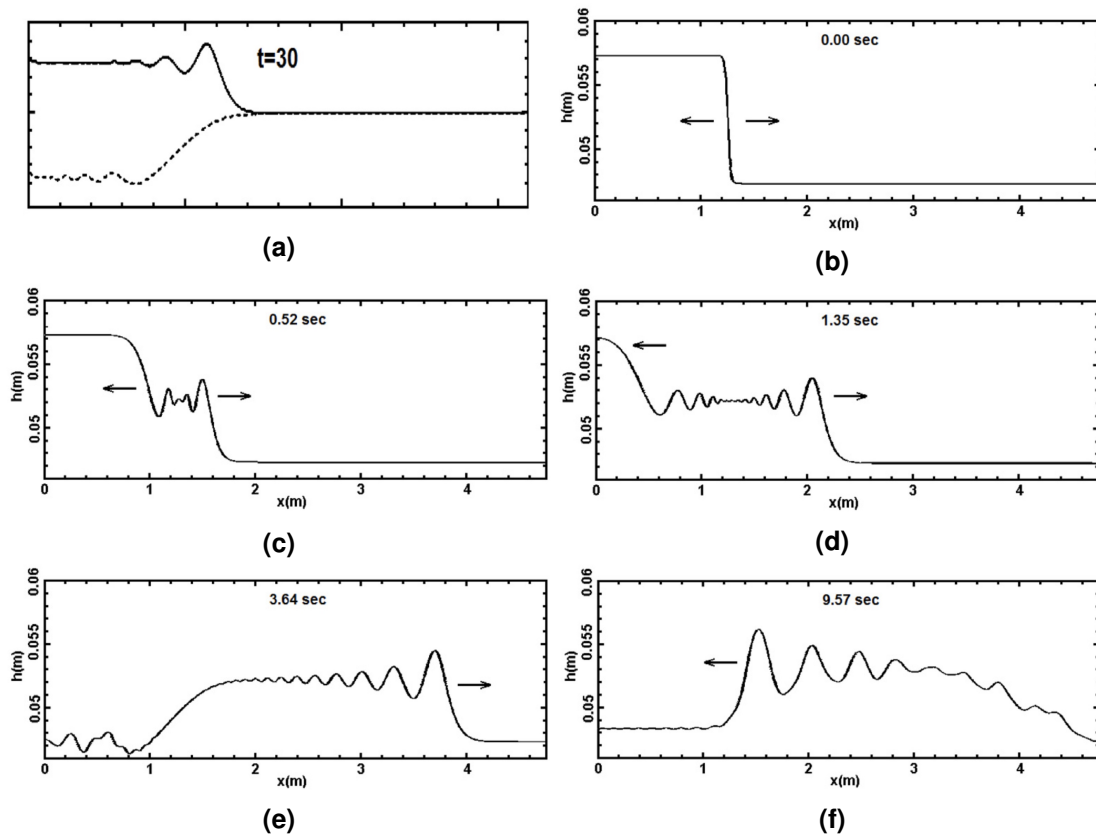


**Figure 7.3:** Simulation results from Besthorn and Tyvand [13] showing bore generation with different methods: (a) by injecting (solid line) or sucking (dot line) the fluid; (b) - (f) by abruptly removing the wall separating water with different levels.

To produce undular bores in laboratory experiments, a usual method is abruptly changing the height of fluids in two regions with different levels, such as suddenly removing a barrier that separates fluids with different depths. Although undular bores produced by an abrupt change of fluid depth are not identical to tidal bores generated by a constant pumping (source term), the differences are insignificant if the length of the two zones with different levels is sufficiently large compared to the bore wavelength. Compared with bore production with a

source/sink, where only a positive/negative bore is generated, an abrupt change of the fluid depth generates a pair of positive and negative bores, that originate from the middle of the height difference and propagate in different directions, as can be seen in fig. 7.3(b)-7.3(f).

This process is depicted with a simple model, as presented in fig. 7.4, showing the formation of the bore pair by abruptly changing the fluid depth. Assuming that the water surface outside the bore front is flat at the onset of the bore formation, due to mass and momentum conservation and the fact that the wave speed is proportional to  $\sqrt{h}$ , the rupture point is given by

$$h_r = \frac{h_{max} + h_{min}}{2} + \frac{(h_{max} - h_{min})^2}{8h_{min}} + O((h_{max} - h_{min})^3), \quad (90)$$

where  $h_{min}$  and  $h_{max}$  are the fluid levels before the bore formation. The equation suggests that the two bores rupture not at the halfway point of two water levels  $(h_{max} + h_{min})/2$  but slightly above the halfway point. In practice, the magnitude of the second-order term in (90) yields a value of two orders smaller than  $(h_{max} + h_{min})/2$  for present experimental parameters, which is in fact not resolved in the experimental measurements and numerical simulations.

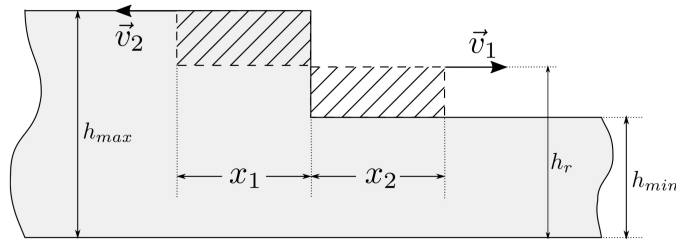


**Figure 7.4:** Sketch of the idealized model of bore generation by abruptly changing the height of fluids in two regions with different levels. The solid line indicates a step function as the initial profile and the dashed line represents the front splits into two step fronts after a short time  $t$ . The sketch is reprinted from Borgia *et al.* [16].

A considerable number of systematic laboratory studies on bores have been performed over the last two decades [25], [33], [75], [102]. All the laboratory studies on tidal bores have been conducted in horizontal rectangular open channels with lateral boundaries. In contrast, we have designed an experiment in which undular bores are produced in an open circular channel. More specifically, two different cases have been investigated: a single bore case with a rigid boundary setup and a bore colliding case with a periodic lateral boundary setup. For the latter case, according to our knowledge, we have realized for the first time the

bore generation in a circular and hence periodic channel. This geometry accomplishes in naturally the periodic lateral boundary conditions, very often used in numerical simulations. On the other hand, the circular geometry permits a good and efficient deployment of the measurement equipments along the experimental channel.

In the present chapter, we experimentally and numerically investigate the influence of the initial fluid depth difference on an undular bore and the interaction between two colliding identical bores. The chapter is organized as follows: section 7.2 describes the experimental setups; section 7.3 discusses the experimental results and the properties of the generated bores; section 7.4 presents the theoretical formulation of the problem in the frame of an inviscid irrotational fluid including comparisons between the numerical and the experimental results; section 7.5 presents an experiment with a sloshing shallow water setup by switching on the longitudinal oscillation of the circular channel; finally, the conclusions are given in Sec. 7.6.

## 7.2 Experimental Setups

The experiment takes advantage of the outer circular channel of the MSGWs tank, which has the circumference of  $L = 4.76$  m and the gap width  $D = 8.5$  cm. A detailed introduction of the tank has been given in chapter 3. The measurement of a bore is realized by measuring the position of the water surface with the help of ultrasonic sensors (acoustic sensors), which are placed along the centerline of the channel with certain distances from each other. For the distribution of ultrasonic sensors, as shown in fig. 7.5, we have different options depending on the particular requirement of the measurements. In order to produce bores, two rectangular plates are used as barriers and placed in the channel. The broadside of both barriers are enveloped by single-sided EVA (Ethylene-vinyl acetate copolymer) foam tape to enhance the sealing of the barriers and reduce the leakage of the fluid due to the different fluid levels.

When the two barriers are placed in the channel, as marked with red colour in fig. 7.5, the circular gap is divided into two parts: a shorter arc channel with a length of 140 centimetres and a longer channel with 334 centimetres. By pumping the water from the longer channel into the shorter, we create regions with different water levels separated by a rigid wall. A single bore or two bores are able to be generated when suddenly removing one barrier (fig. 7.5(a)) or lifting two barriers simultaneously (fig. 7.5(b) and 7.5(c)). For the single bore setup, since

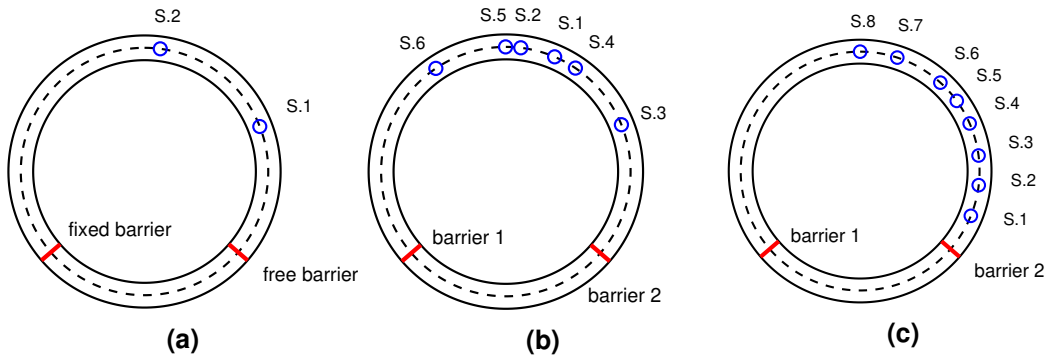


**Figure 7.5:** Position of ultrasonic sensors for different experimental setups. For (a) only the right barrier is removed to produce bores, whereas for (b) and (c) the two barriers are removed simultaneously to produce colliding bores.

one barrier is fixed, the boundary condition is not periodic. If the curvature is neglected, the system is equivalent to a straight channel with two rigid walls at each end.

For the investigation of single bore generation, only two ultrasonic sensors (S.1, S.2) have been placed at about 20 cm above the liquid surface with a separation distance of 81 cm one from the other. For the study of colliding bores six or eight different sensors (S.1–S.6) have been mounted in the collision zone (fig. 7.5(b) and 7.5(c)). In fig. 7.5(b) the sensor S.5 is placed on the symmetry axis at the bore collision point. The sensors S.4 and S.6 are placed symmetrically over S.5 and are used to verify the synchronicity of clockwise and anticlockwise propagating bores. To assure the formation of two identical bores, the two barriers should be simultaneously removed. In this case, the configuration in fig. 7.5(b) has been chosen in order to reconstruct the bore propagation before and after the collision based on the symmetry condition. The sensor S.8 is located on the symmetric axis and all other sensors (S.1 - S.7) are arranged on the right side of S.8 for a higher resolution of the elevation.

The experiments are controlled by two parameters: the undisturbed water level  $h_0$  ranging from 30 to 160 mm and the difference of water levels  $\Delta h$  ranging from 5 to 60 mm. The difference of water levels between the two sides of the removable barrier describes the “source strength” of the tidal bore and  $\Delta h/h_0$  is the equivalent to the Froude number for small surface elevations. In our experiments, the ratios  $\Delta h/h_0$  are kept lower than 0.4 in order to avoid breaking waves (turbulent processes) [13]. For the main part of the experiments, we kept this limit even under 0.28, thus assuring the formation of undular bores [11], [98]. With these parameters, we are able to produce undular bores with the tidal bore Froude number of  $1.11 < Fr_b < 1.43$ .

## 7.3 Experimental Results

### 7.3.1 Single bore

The free surface profile of undular bores excited in the circular channel of the MSGWs tank is presented in fig. 7.6. The data were measured by sensors S.1 and S.2 with the setup of fig. 7.5(a) for two different heights  $h_0$  and two height level differences  $\Delta h$ . Figure 7.6 shows a train of waves travelling through the positions of the two sensors after releasing the barrier. The  $y$ -coordinate  $h$  represents the surface level relative to the bottom.

To quantify the experimental results, the following parameters are defined and compared: bore propagation velocity  $v_f$ , bore wavelength  $\lambda$  and front height  $H_f$ . The propagation velocity  $v_f$  is calculated by dividing the distance between S.1 and S.2 with the time difference after detecting the arrival of the first crest at the sensors ( $t_v$  on fig. 7.6(b)). The wavelength  $\lambda$ , according to Berry [12], is defined as the distance between the first two crests. Considering the variation of the propagation velocity is slow,  $\lambda$  can be calculated by simply multiplying  $v_f$  and  $t_\lambda$ , i.e. the time interval between the first and second crest, as noticed on fig. 7.6(b). The front height  $H_f$ , as marked on fig. 7.6(b), is the height of the first crest relative to the water level before releasing the barrier.

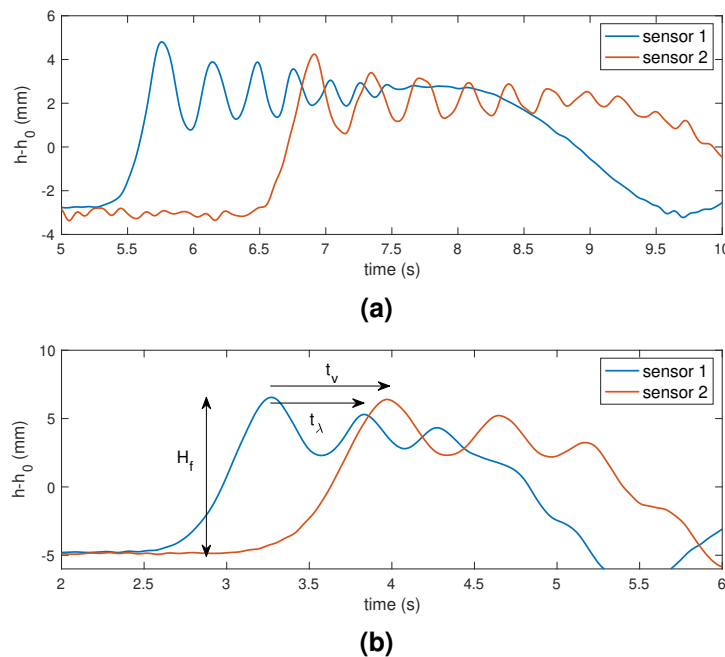


**Figure 7.6:** Undular bores excited in the circular channel for two different heights and height level differences: (a)  $h_0 = 5$  cm,  $\Delta h/h_0 = 0.2$  (b)  $h_0 = 16$  cm,  $\Delta h/h_0 = 0.125$ . The value 0 on  $y$ -axis represents the level of undisturbed water.

Compared to fig. 7.6(a), the bore in fig. 7.6(b) has a higher front height  $H_f$ . Meanwhile, the bore in the latter figure spends a shorter time travelling from the position of S.1 to S.2, which suggests the latter case has a faster propagation velocity  $v_f$ . For a systematic study on the propagation velocity and bore wavelength versus the depth of the undisturbed water layer  $h_0$  and the difference of water level  $\Delta h$  (before the removing of the rigid wall), a series of experiments have been performed with different combinations of  $h_0$  and  $\Delta h$ . The result is elucidated in fig. 7.7.

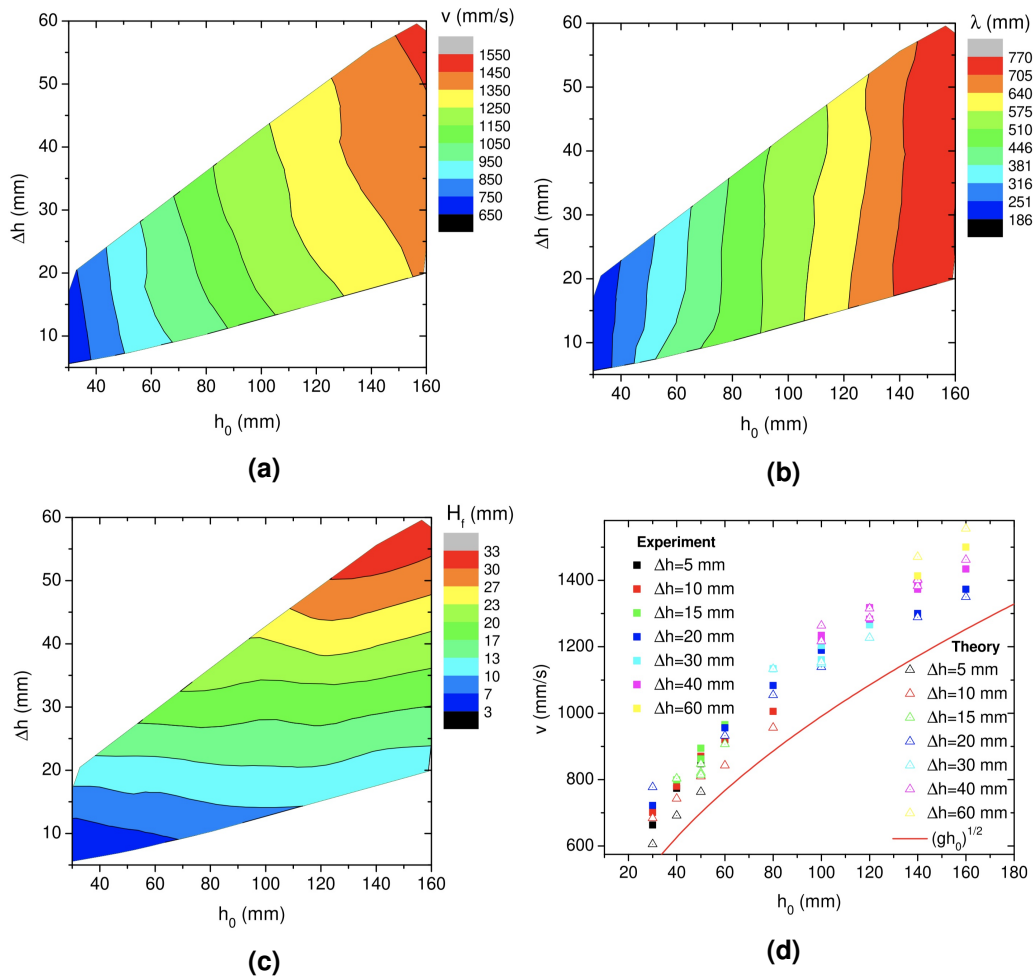


**Figure 7.7:** (a) The propagation velocity  $v_f$ , (b) the wavelength  $\lambda$  and (c) the front height  $H_f$  of undular bores as functions of the depth of the undisturbed water layer  $h_0$  and difference of surface level  $\Delta h$  before removing the barrier; (d) Comparisons of  $v_f$  for the same  $h_0$  and  $\Delta h$  between experiments and numerics. The squares in (d) denote experimental results, the red line corresponds to the shallow water theory for small perturbations around  $h_0$ , and the triangles are the calculated velocities for shallow water but with finite bore height  $\Delta h$  as in [7]. The figures are reprinted from Borgia *et al.* [16].

According to fig. 7.7(a) - 7.7(c), the propagation velocity, the wavelength and



the front height show different dependencies on the average liquid depth and the initial height difference. The wavelength mainly depends on the average depth and less on  $\Delta h$  (see fig. 7.7(b)), whereas the front height  $H_f$  depends mainly on the initial height difference  $\Delta h$  (see fig. 7.7(c)). The propagation velocity, in contrast, depends on both the average liquid depth and the initial height difference. For a smaller height difference, the undular bore propagates with a slower velocity.

The measured phase velocities are plotted with square symbols in fig. 7.7(d) showing that  $v_f$  asymptotically approaches the shallow water value  $v_f = \sqrt{gh_0}$  for  $\Delta h \rightarrow 0$ , which actually agrees with Ali and Kalisch [7]. In the same figure, the results using equation (2.6) from Ali and Kalisch [7] without base flow are plotted for the same values of  $h_0$  and  $\Delta h$  using the same colour but with a triangle symbol. In view of the experimental errors, the tendency showed by the experiment is retrieved also in the theoretical results. Although we are at the validity limit of the long-wave approximation ( $h_0/\lambda$  ranging between 0.1 and 0.2), the propagation velocity still satisfies the model as prescribed by the shallow water limit.

Tracking a bore travelling over a longer time period in the channel, we observed decay of the bore amplitude, which is not the case for all surface waves (for example for a class of capillary gravity solitary waves [56]). In the experiment, the bore front moves with a spatially constant velocity during the bore propagation except for thin boundary layers near the lateral walls. The decay of the bore amplitude is equivalent to the decay of the internal fluid velocity. The propagation of the bore can be regarded as a Poiseuille flow in an open channel. Since the laws of flow resistance in open channels are essentially the same as those in closed pipes [51], the loss of the velocity can be estimated by the Darcy-Weisbach equation using the friction factor for a rectangular pipe. In the experiment, the utilised acoustic sensor can return random errors and produce deviations in the measured value. These deviations may lead to a high relative error for a long duration measurement. Therefore the acoustic sensors are not suitable for precisely measuring the decay of the surface elevation of the bore for long travel time. For this reason, a PIV measurement were performed for a more reliable measure of the decay of the flow velocity.

The PIV applied a typical setup that a line laser (MediaLas® Compact line laser kit GREEN 75mW) was placed over the channel and projected a laser plane perpendicular to the surface and along the centerline of the channel in the stream-wise direction. To ensure the laser plane corresponding to the circular shape of the channel, an additional tilted convex cylindrical lens was added to the system

so that the laser plane is slightly bent into a curved laser sheet [79]. The camera was placed perpendicular to the laser sheet outside the outer wall, which allows recording the video with a  $1920 \times 1080$  resolution at 120 frames per second. To ensure that the velocity field in the wave crest is measured by PIV, the field of view is required to capture the entire bore. Since the boundary between the fluid and the air changes continually during the propagation of the bore, the evaluation of the PIV inevitably contains the region of the air, where no tracers are distributed, and produces spurious vectors, such as the upper region in fig. 7.14. An appropriate solution is creating a dynamic mask based on the surface profile measured by ultrasonic sensors to ensure that the PIV evaluation is only executed in the interior of the fluid [32]. However, since the errors in the air region do not influence the measurement in the flow interior as well as the data presented in the thesis, a dynamic mask was not applied for our experiment.

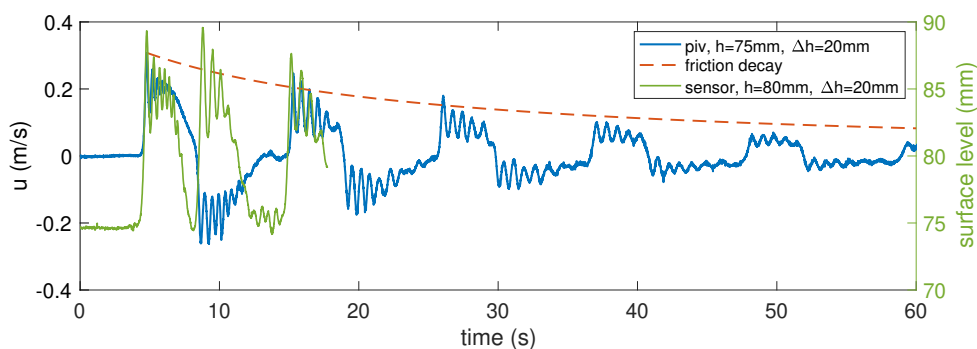


**Figure 7.8:** The streamwise velocity  $u$  as a function of time measured at  $h = 60$  mm for a single bore with  $h_0 = 75$  mm,  $\Delta h = 20$  mm compared with the surface profile of a single bore with  $h_0 = 80$  mm,  $\Delta h = 20$  mm. The red dashed curve indicates the decay of velocity due to the friction.

The blue curve in fig. 7.8 elucidates the temporal evolution of the streamwise velocity  $u$  measured at a fixed point 60 mm above the bottom by PIV. The positive velocity indicates that the bore propagates in an anticlockwise direction, whereas the negative velocity represents a clockwise propagating bore, i.e. the bore reflected after an odd number of times. The green curve in fig. 7.8 represents the surface profile measured by an acoustic sensor and the sign is independent of the propagation direction of a bore. The red dashed curve in the figure indicates the decay of velocity due to the friction.

The velocity profile shows a good agreement with the surface profile measured at a similar position. Compared to the frictional decay, the velocity appears to have a slightly faster damping rate. One reason for the difference is that the simple empirical equation for a rectangular pipe may be not perfectly appropriate for

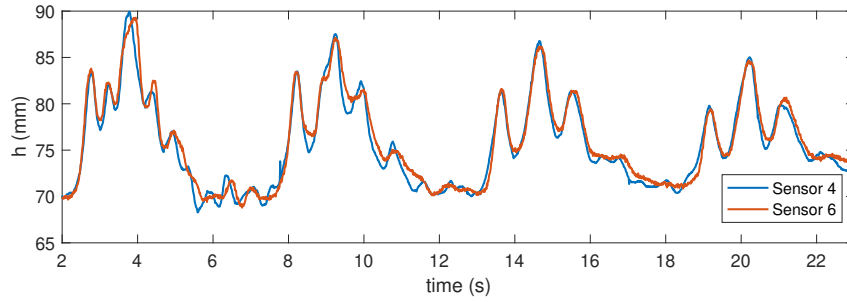


**Figure 7.9:** Signals from the symmetrically positioned sensors S.4 and S.6 for  $h_0 = 75$  mm,  $\Delta h = 20$  mm verifying the symmetry condition of colliding bores.

the case with a propagating bore. A further reason might be due to the nonlinear effects during the reflection at the barrier. Nevertheless, the friction loss provides a reasonable explanation for the damping of the fluid velocity.

In addition, a group of weak fluctuations of the surface profile (the green curve) at  $t = 12 - 15$  s is noticed on fig. 7.8. The group of fluctuations might correspond to the backward propagating bore (i.e. the negative bore) as elucidated in fig. 7.3. This negative bore is not stably generated for each individual experiment, since the release of the barrier is manually controlled and thus can influence the production of the negative bore.

### 7.3.2 Colliding bores

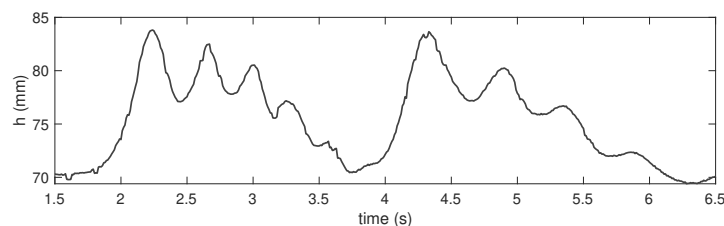
Releasing the two rigid walls in fig. 7.5(b) simultaneously, two groups of bores are produced and propagate symmetrically in clockwise and anti-clockwise directions. Due to the periodic boundary condition of the circular channel, the bores collide repetitively at the 6 and 12 o'clock position in the channel. The odd collisions (i.e. the first collision, the third collision and so on) can be observed by sensor S.5 and the even ones (the second collision, the fourth collision, etc.) occur in the diametrically opposite region of the circular channel.

Figure 7.9 and 7.10 show the signals of a bore collision experiment with the initial condition  $h_0 = 75$  mm and  $\Delta h = 20$  mm. Signals in fig. 7.9 are measured from the symmetrically positioned sensors S.4 and S.6, which demonstrates the symmetry condition of colliding bores. Since the two barriers are released manually, the synchronisation between S.4 and S.6 is an essential quantity that is directly related to the quality of a measurement.

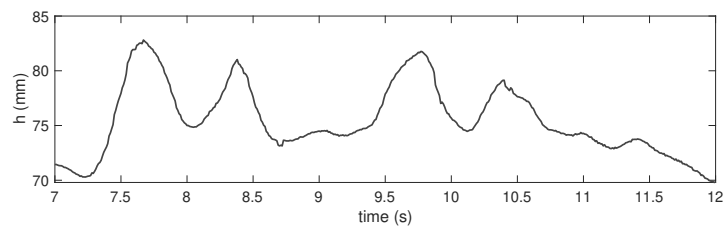
Figure 7.10 shows the shape of bores measured by S.3 before and after the first and third collisions. The sensor S.3 is positioned sufficiently far from the colliding point with a longer distance than the length of a bore so that the anticlockwise

propagating wave train does not overlap with the clockwise propagating wave train.

Assuming the experiment is axisymmetric and considering the fact that the shape and propagation velocity of bores change slowly in time, a plot of bores shortly before and after the collision using the surface height as a function of time, is equivalent to a plot using the surface height as a function of azimuthal coordinate. Following this rule, a plot in fig. 7.10(a) shows the structure of the anticlockwise bore before the first collision and the clockwise bore after the first collision, whereas fig. 7.10(b) is plotted in the same way for the third collision. According to the symmetric condition (fig. 7.9), fig. 7.10 can be considered as the structure of the same bore before and after a collision. It is obvious that the shape of the bore is slightly changed after a collision and for the first collision the change in shape is more significant. One of the reasons responsible for the change is that the fluid depth is slightly increased after the collision. Since the propagation of an undular bore is accompanied by volume flux, the liquid after a bore is deeper than that in front of the bore. After a few collisions, the small scale structures are damped and only the major bore structures retain, meanwhile the height of bore crests is also gradually decreased.



(a)



(b)

**Figure 7.10:** Signals from the sensor S.3 showing the bores before and after the first (a) and third (b) collisions for  $h_0 = 75$  mm,  $\Delta h = 20$  mm. For both cases, the left side of the signal ( $t < 4s$  in (a) and  $t < 14.5s$  in (b)) gives the bore shape before collision and the right side the bore shape after.

## 7.4 Comparisons Between Simulations and Experiments

### 7.4.1 Introduction of the numerical model

Direct numerical simulations of the Euler equations have been performed at BTU Cottbus-Senftenberg in the group of Michael Bestehorn. As given in Bestehorn and Tyvand [13], a 2D irrotational flow of an incompressible and inviscid fluid with free surface is considered. The velocity field of the fluid  $\mathbf{v}$  can be described by the scalar flow potential  $\Phi$  that

$$\mathbf{v}(x, z, t) = \nabla\Phi(x, z, t). \quad (91)$$

Due to the incompressibility condition, the continuity equation becomes

$$\Delta\Phi = 0. \quad (92)$$

The length and time scale are normalized by the undisturbed water level  $h_0$  and the gravitational acceleration  $g$  so that

$$(x, z) \rightarrow (h_0 \cdot \tilde{x}, h_0 \cdot \tilde{z}), \quad t \rightarrow \sqrt{h_0/g} \cdot \tilde{t}. \quad (93)$$

Letting the location of the free surface be described by  $h(x, t)$ , the boundary condition on the free surface is given by the Bernoulli equation (momentum equation) and reads

$$\frac{\partial\Phi}{\partial t} \Big|_{z=h} = 1 - h - \frac{1}{2} \left[ \left( \frac{\partial\Phi}{\partial x} \right)^2 + \left( \frac{\partial\Phi}{\partial t} \right)^2 \right] \Big|_{z=h}, \quad (94)$$

where  $h$  is calculated from the kinematic boundary condition at the deformable surface in the form

$$\frac{\partial h}{\partial t} = \frac{\partial\Phi}{\partial z} \Big|_{z=h} - \frac{\partial h}{\partial x} \frac{\partial\Phi}{\partial x} \Big|_{z=h}. \quad (95)$$

The equations (90)–(94) have been numerically solved in two spatial dimensions for a laterally closed geometry with impermeable side walls, following the scheme described in detail in Bestehorn and Tyvand [13].

### 7.4.2 Single bore

Figure 7.11 compares the experimental measurement and numerical simulation of the temporal evolution of the surface at two fixed positions, i.e. S.1 and S.2 in fig. 7.5(a). The diagram shows a very good agreement with a rather perfect overlap between the theoretical curve and the experimental curve even after three reflec-

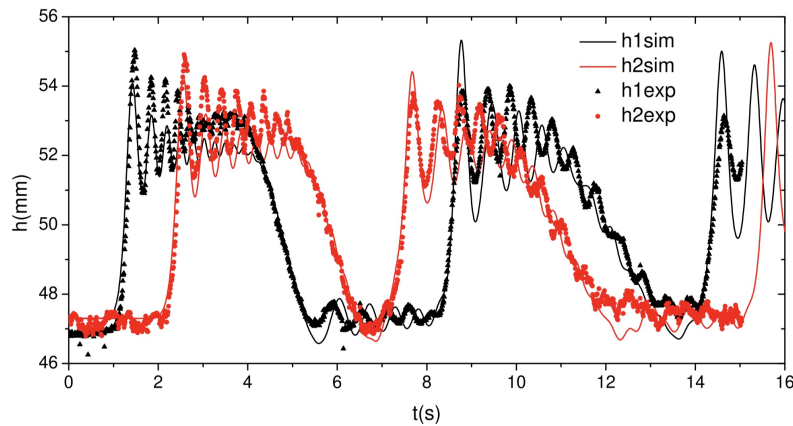


**Figure 7.11:** Comparison of experiment and simulation for undular bore generation and reflection, reprinted from Borcia *et al.* [16].

tions from the fixed wall. However, the slowly decreasing amplitude in terms of time for the experimental result is not revealed by the numeric simulation, since the simulation is applying inviscid conditions so that the viscous friction inside the liquid is not taken into account in the numerical model.

### 7.4.3 Colliding bores

Furthermore, a comparison of the experiment and numerical simulation for the bore collision problem has been performed with the same initial condition  $h_0 = 75$  mm,  $\Delta h = 24$  mm. As plotted in fig. 7.12, we focus only on the first collision and on the region where the sensors are placed.

Figure 7.12(a) is a 2D contour plot interpolated from measured data of the six sensors (fig. 7.5(b)) showing the evolution of the free surface. In the plot, the positions of the sensors and their symmetrical positions are marked with dashed lines. The plot shows two opposite propagating bores colliding in the middle and travelling sequentially afterwards. However, due to the not sufficiently dense distributed ultrasonic sensors, the evolution at the free surface is not fully captured. The numerical result is shown in fig. 7.12(b). Comparing to fig. 7.12(a), the numerical simulation provides more information of the free surface evolution. For a better comparison of experimental and numerical results, only those numerical data that are at the positions that correspond to the position of the sensors are extracted and plotted in fig. 7.12(c) using the same interpolation. These positions in the circular channel are elucidated in fig. 7.12(a). Despite the stripes at the bottom of fig. 7.12(a) due to the systematic errors of the acoustic sensors, fig. 7.12(a) and 7.12(c) show a very good agreement, especially in the region of the collision.

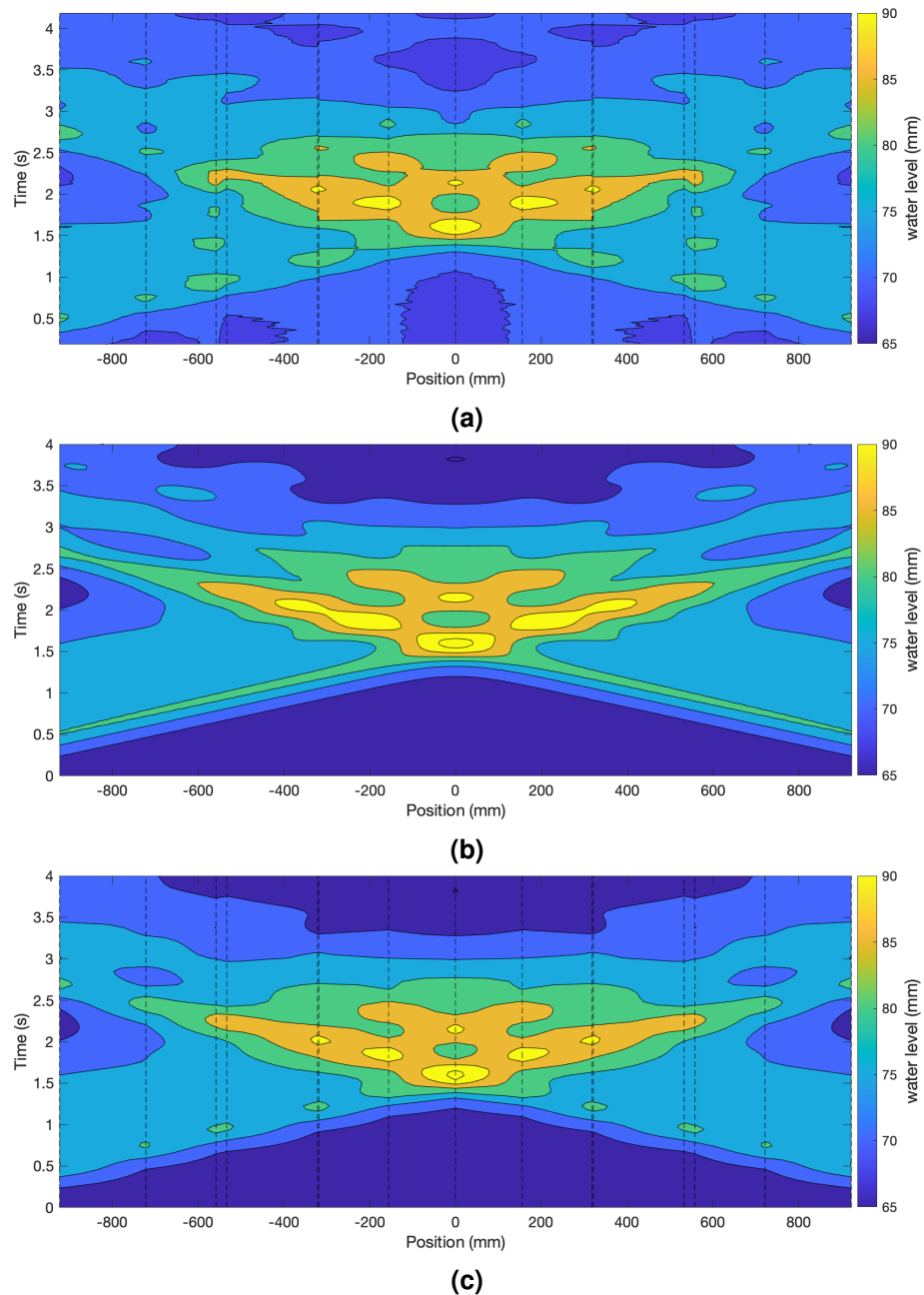


**Figure 7.12:** Comparison between experimental data (a) and numerical simulations (b) and (c) in the bore collision region for  $h_0 = 75$  mm,  $\Delta h = 24$  mm. The position of the sensors are marked with dashed lines. Note that also the symmetry of the problem is taken into account. Plot (b) shows the complete information from the numerical simulation where as in (c) only the data corresponding to the position of the sensors has been used.

Since the numerical simulation was conducted with an inviscid fluid, the slow decrease of the bore amplitude cannot be resolved in the numerical result, therefore the bore amplitude in the numerical simulation is higher than the amplitude from the experimental measurement. However, the propagation of the wavefront in experiments and numerics is still comparable.

The time-space diagram of fig. 7.13 shows the composition of the surface level from the numerical result and the experimental measurement for a longer duration (six collisions). The central region with position from -1 to 1 is plotted based on the experimental data and shows the collision with odd numbers, whereas the rest part of the diagram is based on the numerical result and shows the collision with even numbers. It is noticed that both the experiment and the numerical simulation have a periodic boundary condition, therefore the time-space diagram is periodic in the y-axis.

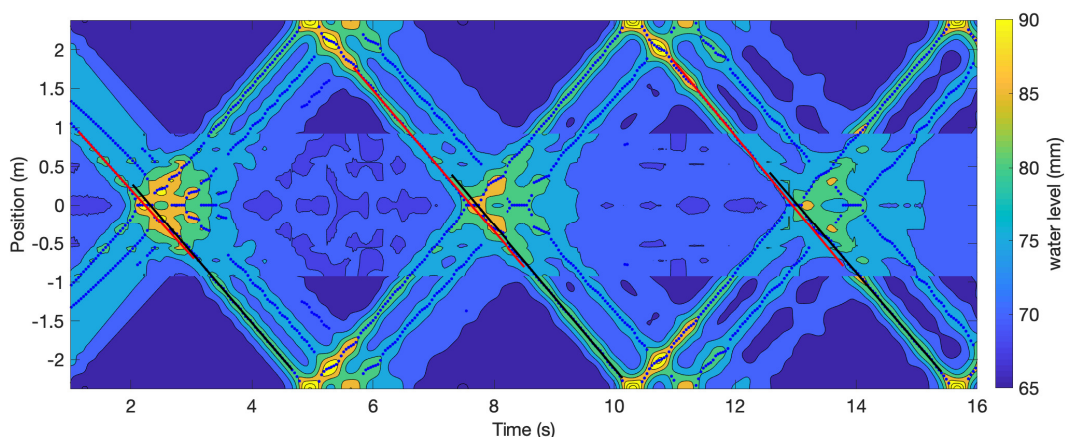


**Figure 7.13:** A Hovmöller plot showing the surface profile of the first six bore collisions. Odd collisions happen around the origin of the position axis. In this region, ultrasound sensors are placed and the plotted water level corresponds to the measurements. For the even collisions no sensors are placed, the plotted water level is provided by computer simulations. Blue points are maxima from the numerical simulation. The red and black lines are the fitting of the bore front position before and after a collision.

Again, numeric and experiment achieve a very good agreement in the bore propagation in fig. 7.13. Based on this result we can focus on the numerical simulation since it provides data of the full circular channel with a spatial resolution of 1000 gridpoints.

Tracing the trajectory of the wave peaks, we can find out the influence of the collision on the velocity and phase of the bore. As one can see in fig. 7.13, the blue dots indicate the trajectory of the two highest wave peaks of a bore from the numerical data and several solid lines are plotted based on a linear regression of the



blue dots, which gives a linear prediction or retrospect of the bore propagation. The red lines represent the bore before a collision and the black lines are after a collision.

A tiny change in the bore velocity during the first collision is observed, where the slopes of the lines are slightly different before and after the first collision, but for the further collisions, a change in the bore velocity is not obvious. This fact can be correlated with the change of bore shape (see fig. 7.10) during the first collision, which is also more significant than for the following collisions. The velocity after the collision is slightly increased since the bore propagates in deeper water after the collision.

A slight shift of the lines before and after a bore collision has been observed. The slight shift suggests that there is a small delay in the bore propagation, which results from the nonlinear effects during the collision.

#### 7.4.4 Influence of the centrifugal force

Since the bores propagate in a circular channel whereas the simulation applies a straight channel with an equivalent length, the influence of the centrifugal forces should be evaluated in case the centrifugal force leads to different surface heights in the radial direction during the propagation of the wave.

By performing a PIV measurement on a vertical section along the centerline of the channel, the evolution of the streamwise velocity  $u$  during a travelling bore is acquired and shown in fig. 7.14 for the single bore setup with  $h_0 = 75$  mm,  $\Delta h = 20$  mm. The outliers on the upper part of the diagram above  $h = 60$  mm to 80 mm are errors due to executing a PIV evaluation on part of the images above the fluid surface, where there are in fact no PIV tracers. The PIV data show that the maximum velocity locates at the first wave crest of the bore and its magnitude is around 0.33 m/s, which is significantly slower than the propagation of the bore (around 1 m/s for the same parameter).

In the circular channel, the velocity with the magnitude 0.33 m/s has the centrifugal acceleration of  $0.14 \text{ m/s}^2$ , which results in a 1 mm difference (1.5% of the water height) in the surface level in the radial direction between the outer and inner side of the channel. The PIV data in fact show a very good agreement with the numerical simulations. As listed in table 7.1, the velocity of the fluid for  $h_0 = 80$  mm,  $\Delta h = 20$  mm is well predicted by the simulations. Consider the best and worst scenario in the range of the parameters, the liquid height difference in the radial direction due to the centrifugal force ranges from 0.5% to 3.5% of the

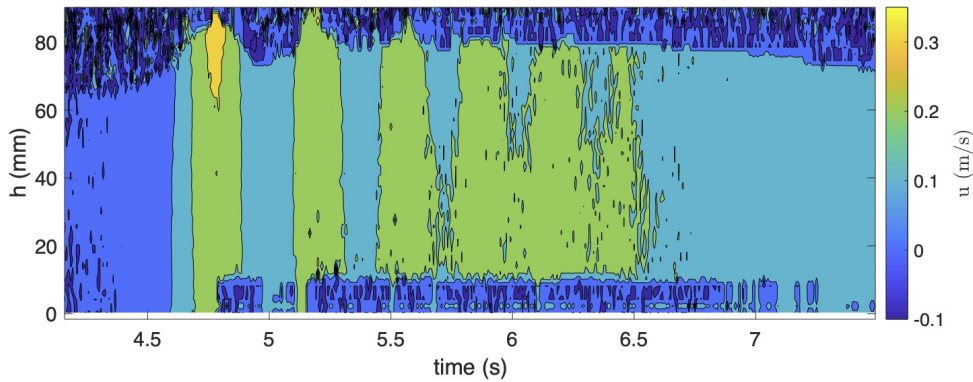


**Figure 7.14:** A Hovmöller diagram showing the streamwise velocity  $u$  as a function of time for a single bore with  $h_0 = 75$  mm,  $\Delta h = 20$  mm.

mean liquid height and can thus be ignored.

**Table 7.1:** The maximal value of the centrifugal acceleration  $a_{cf,max}$  and the surface elevation due to the centrifugal force during the bore propagation from numerical simulations. The effect of the curvature is measured by the liquid height difference in radial direction due to the centrifugal force  $\frac{a_{cf,max}}{g} D$  ( $D = R_{max} - R_{min}$ ,  $D \ll R_{min}$ ) relative to the mean liquid height  $h_0$ . The table is adapted from Borgia *et al.* [16].

case	$h_0$ (mm)	$\Delta h$ (mm)	$u_{max}$ (m/s)	$a_{cf,max}$ (m/s <sup>2</sup> )	$\frac{a_{cf,max}}{g} \cdot \frac{D}{h_0}$ (%)
maximum	160	60	0.7	0.65	3.5
minimum	30	5	0.12	0.019	0.5
typical	80	20	0.32	0.14	1.5

## 7.5 Sloshing Shallow Water

Based on the present experimental setup, another type of sloshing flow is investigated, in which the channel is equipped with a fixed barrier and filled with shallow water and the tank oscillates longitudinally with  $\Omega \sin(\omega t)$ , where  $\omega$  is the oscillation angular frequency and  $\Omega$  is the oscillation amplitude with the unit in rpm. Depending on the oscillation amplitude, the sloshing barrier is able to produce waves or hydraulic jumps (i.e. bores) travelling to and fro periodically in the channel [65].

This setup is related to the liquid sloshing in a closed basin, which has been studied in many engineering fields such as coastal engineering [27], aerospace engineering [1], and earthquake engineering. The mechanism is also closely related to the so-called tuned liquid damper (TLD), which changes the dynamic characteristics of a structure and dissipates its vibration energy relying on the motion

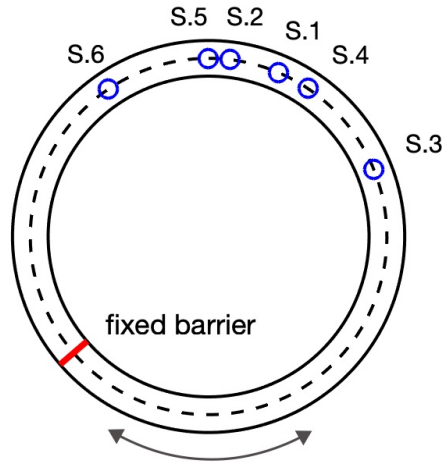


**Figure 7.15:** Configuration of the oscillating experiment.

of shallow liquid inside a rigid tank [43]. The TLDs have been used for suppressing the structural vibrations of large buildings, towers and bridges resulting from external impacts such as earthquakes [44].

In the shallow water setup, the natural sloshing frequencies can be predicted by using the linear theory

$$\omega_r^n = \frac{2\pi(2n-1)\sqrt{gh_0}}{L}, \quad n = 1, 2, 3, \dots \quad (96)$$

where  $L$  is the length of the channel and  $h_0$  is the still water depth. The lowest natural frequency ( $n=1$ ) is simply denoted by  $\omega_r$ . Violent surface wave response may take place, when the forcing frequency close to resonance, i.e. close to  $\omega_r$ , even for small forcing amplitudes. At a critical frequency  $\omega_f$  close to  $\omega_r$ , the resonant excitation ceases due to a bifurcation phenomenon [40]. For forcing frequency around higher natural frequencies (i.e.  $n > 1$ ), primary resonances also arises, although the induced wave response is generally weaker [19].

Due to the strong nonlinear effects in a resonant sloshing flow, the linear theory is no longer valid. In this case, the effects of dissipation and dispersion also play a significant role in determining the form of the oscillating surface. In a sloshing flow with a sufficient strong forcing, when the dissipation becomes dominant compared to the dispersion, the sloshing flow forms a weak bore that travels back and forth while continuously reflected from the barrier in the channel, whereas the surface profile behaves like a series of cnoidal waves when the dispersion is dominant [27].

The resonance response of sloshing shallow water was studied by Bouscasse *et al.* [19], Chester [27], Chester and Bones [28], Faltinsen and Timokha [41], Lepel-

letier and Raichlen [69], Ockendon *et al.* [93] and Ockendon and Ockendon [94]. Nevertheless, the experimental studies explored only the characteristic depth, i.e. the ratio of the water depth and the channel length,  $h_0/L > 0.03$ . In the presented experimental setup, we investigated the resonant response of the sloshing water for a very small ratio  $h_0/L = 0.01$ , where the effect of the dissipation in dominant and travelling bores are generated by the periodic forcing.

Figure 7.16(a) shows the response amplitude  $(h - h_0)/h_0$  as a function of the forcing frequency  $\omega/\omega_r$  measured by different sensors. It is noticed that the forcing amplitude  $A/L$  is not constant but inverse proportional to the forcing frequency  $\omega$  with the relation  $A/L = 2\pi\Omega R/(60L\omega) = 0.0058/\omega$ , where  $\omega$  ranges from 0.3 to 3.6 so that  $0.0192 > A/L > 0.0016$ .

As shown in fig. 7.16(a), four primary resonances can be observed at around  $\omega/\omega_r = 1, 3, 5, 7$ , where the response amplitude of the first resonance is magnified in fig. 7.16(b). The resonant response amplitudes for higher resonances are significantly lower. The main reason is attributed to the decreasing forcing amplitude when the forcing frequency increases. Although higher resonances generally induce weaker responses [19], this effect is not obvious in our case due to the dramatic decrease of the forcing amplitude.

According to the nonlinear theory, the response amplitude is not symmetric over the resonant frequency but increases gradually with the forcing frequency and drops abruptly after reaching the maximum amplitude. The maximum amplitude is achieved at a frequency detuned from the resonant frequency ( $\omega > \omega_r$ ) due to nonlinear effects. An example of this effect is presented in fig. 7.16(c), which shows the response amplitude as a function of forcing frequency under the effect of different forcing amplitudes for a sloshing shallow water setup with  $h_0/L = 0.03$ . The data are taken from the numerical simulations reported in Bouscasse *et al.* [19].

This characteristic can be also identified in fig. 7.16(b). However, due to the small forcing ( $A/L = 0.0192 - 0.01$  for  $\omega/\omega_r = 0.7 - 1.3$ ), the nonlinear effects in the experiment are very weak. In fact, the experimental result can be compared with the numerical data from Bouscasse *et al.* [19], see fig. 7.16(c). In this figure, the curve of the experimental result is given by the maximum values of the six acoustic sensors for each  $\omega/\omega_r$ . Despite the lower response amplitude, the experimental result appears to have a certain agreement with the numerical data. However, due to the inconstant forcing amplitude, such a comparison is not very strict.

In the shallow water setup, the dissipation is stronger than the dispersion, the

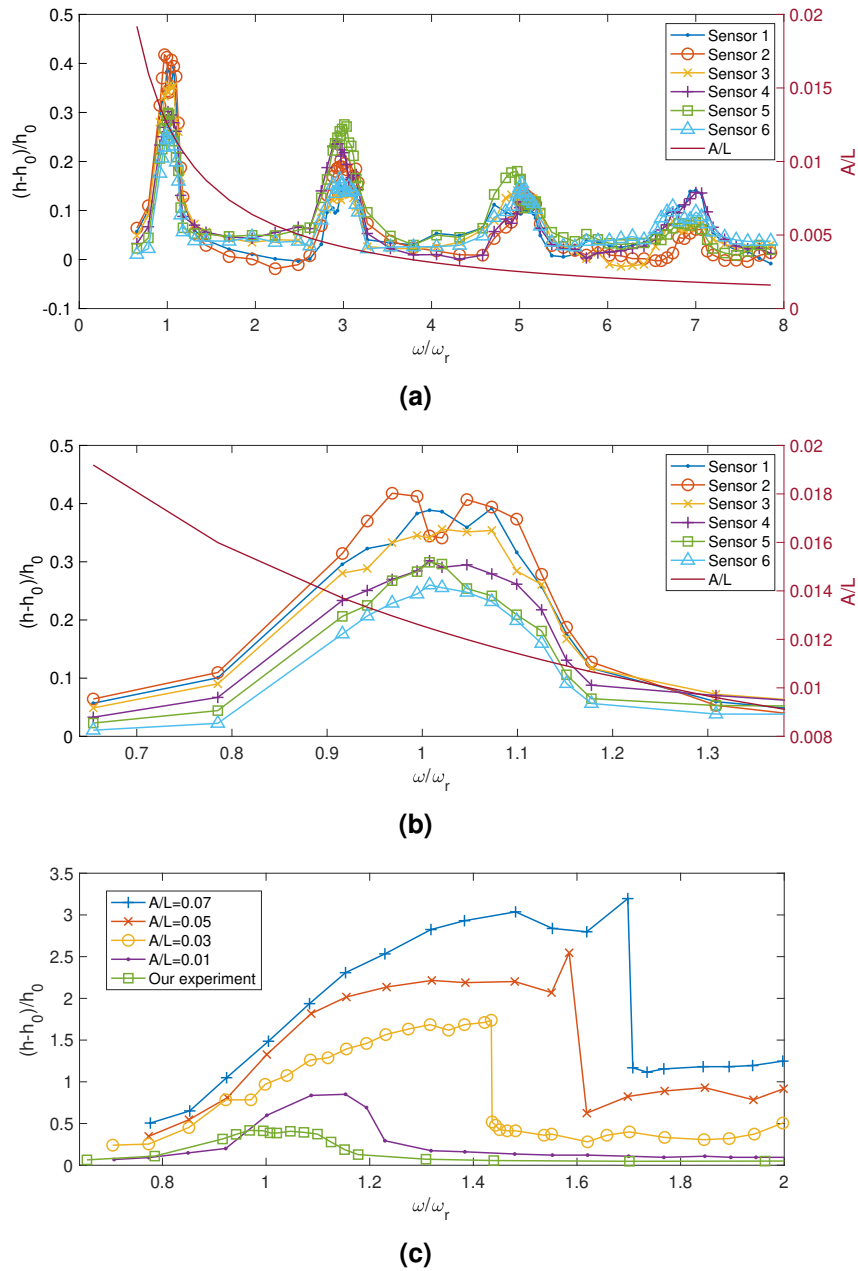


**Figure 7.16:** (a) The response amplitude  $(h - h_0)/h_0$  as a function of the forcing frequency  $\omega/\omega_r$ , measured by different sensors. The dark red curve indicates the forcing amplitude  $A/L$  in accordance with  $\omega/\omega_r$ . (b) is the magnification of the amplitude response around the first resonance. (c) shows the comparison between our experimental data to the numerical data reported in Bouscasse *et al.* [19]. The numerical data give the response amplitude for different forcing amplitudes in a shallow water setup  $h_0/L = 0.03$ .

sloshing flow generated by the periodic forcing propagates as an undular bore, which travels to and fro in the channel. The surface profile of the bore is shown in fig. 7.17 for  $\omega/\omega_r = 1.12$ . Increasing the forcing frequency, we noticed that the bore does not exist for  $\omega/\omega_r > 1.2$  and the surface profile behaves like a cnoidal wave, see red curve in fig. 7.17.

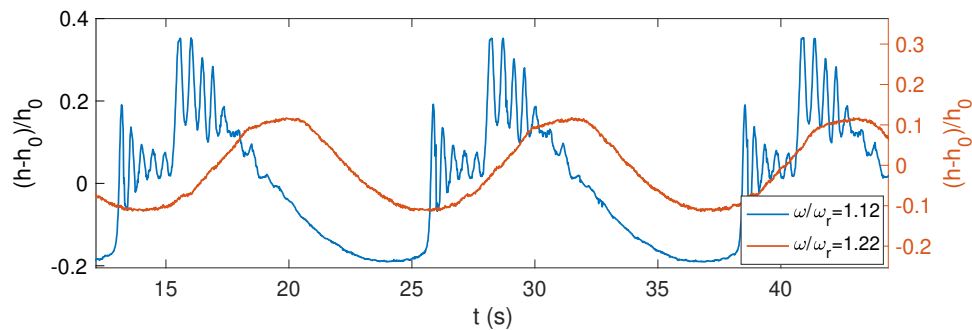


**Figure 7.17:** The surface elevation as a function of time measured by sensor 3 for  $\omega/\omega_r = 1.12$  (blue curve) and  $\omega/\omega_r = 1.22$  (red curve) showing the sloshing flow propagating with different behaviour.

## 7.6 Conclusions and Outlook

Taking advantage of the outer circular channel of the MSGWs tank with a circumference of about 5 m, we have designed an experiment for bore formation and propagation. By sudden releasing a barrier separating fluid with different surface levels ranging between 5 cm and 15 cm, we were able to produce undular bores with tidal Froude numbers ranging between 1.11 and 1.43 and wavelengths ranging between 10 mm and 80 mm. The produced undular bores travel in the channel with a velocity of about 0.6 to 1.4 m/s.

With the present experimental setups, one single bore or a pair of counter-propagating identical bores can be produced by removing one of the two barriers or removing the two barriers simultaneously. As a benefit from the circular geometry, we were able to use the symmetry and periodicity of the problem to study multiple reflection processes. Using multiple acoustic sensors, the surface profiles are captured and recorded. The experimental measurements were compared with the numerical simulations performed by Sebastian Richter in the group of Prof. Besthorn using the model reported in Besthorn and Tyvand [13].

An excellent agreement has been achieved by comparing the numerical simulations to the experimental measurements: the surface profiles are perfectly predicted both for the single bore case (fig. 7.11) and for the colliding bore case (fig.

7.12); the fluid velocity in the wave crest measured by PIV agrees with the numerical result; the propagation of the colliding bores are well reproduced even after several collisions (fig. 7.13).

A decay of the wave amplitudes, as well as the fluid velocities, has been observed in the laboratory experiment. The decay rate can be partly explained by a simple open channel flow model in which the decay results from friction. Nevertheless, the damping cannot be validated with the present numerical method since viscosities and frictions have not been included in the numerical model.

Taking advantage of the oscillating MSGWs tank, we have performed a sloshing shallow water experiment with a very small characteristic depth  $h_0/L$ . The response amplitude has been observed for a wide range of forcing frequencies that cover four primary resonant frequencies. Our results show some agreement with the numerical simulations from Bouscasse *et al.* [19]. However, due to the small forcing amplitude, the nonlinear effects are rather weak. For forthcoming studies, further experiments have been planned with a few improvements, such as a constant forcing amplitude regardless of the oscillation rate and a better arrangement of the ultrasonic sensors, where e.g. one sensor is monitoring the surface elevation close to the barrier.





## 8 Summary

In this work, we presented laboratory experiments with two different setups: a rotating cylindrical annulus setup, which focused on the instability of a rotating and inertially oscillating flow, and a circular channel setup, which investigated the propagation, reflection and collision of undular bores.

In the first experiment, we investigated the rotating fluid in a tilted rotating annulus with the presence of a free surface. Since the rotating axis was subjected to the direction of gravitational acceleration, a Kelvin mode was forced by the gravitational torque on the non-axisymmetric rotating mass. The forced Kelvin mode had the same frequency as the rotation rate of the annulus and the wavenumber 1 in the azimuthal and radial direction. By controlling the rotation rate and the inclination angle of the container, we have explored the rotating flow for the Ekman numbers ranging from  $7.9 \times 10^{-6}$  to  $3.2 \times 10^{-5}$  and two different inclination angles, namely  $\alpha = 0.1^\circ$  and  $1^\circ$ .

When the depth of the filling water is adjusted to a particular value so that the forced Kelvin mode matches or is close to the natural frequency of the rotating fluid, the forced Kelvin mode becomes resonant. The amplitude of the resonant forced mode rapidly grows oversaturated, breaks down and gives rise to small scale disturbances, which is also referred to as “resonant collapse”. In this process, we identified two types of instabilities.

For a small inclination angle ( $\alpha = 0.1^\circ$ ), the instability corresponds to a typical scenario of the triadic resonance, which is similar to the precessing cylinder experiment reported in McEwan [84] and Manasseh [78]. Two well-tuned subdominant free Kelvin modes are given rise and form a triad with the forced Kelvin mode. The frequency and wavenumber of the two free Kelvin modes match the eigenmodes from the linear dispersion relation.

Increasing the inclination angle ( $\alpha = 0.1^\circ$ ), a stronger retrograde mean flow generated due to the nonlinear interactions in the Ekman layer was observed. When the mean flow is sufficiently strong, a shear-type instability is given rise and leads to the generation of a low-frequency barotropic shear mode. The shear mode interacts with the forced Kelvin mode and excites two free Kelvin modes that satisfy the triadic relation with the shear mode and the forced Kelvin mode. The shear instability in fact confirms the theory presented by Kerswell [59], for which a shear instability with a dominant geostrophic component can be triggered before the triadic resonance when the resonant triad is imperfectly tuned and the amplitude of the forced mode is relatively large [52]. Following the shear

instability theory presented by Thompson [110], we achieved a good agreement between the theoretical prediction of the shear instability bounds and our experimental data.

We have observed that the frequencies of the excited modes, except the forced Kelvin mode, are related to the Ekman numbers. The frequencies of the retrograde modes increase with decreasing  $Ek$ , whereas the frequencies of the prograde modes have the opposite tendency. The main reason is attributed to the Doppler shift due to the presence of a strong background flow. This agrees with the work by Herault *et al.*[52]. Moreover, the authors pointed out that the non-zero background flow can modify the dispersion relation, which also influences the frequency of Kelvin modes.

Furthermore, we attempted to adapt the experimental data to a low-order dynamical system developed by Lagrange *et al.* [64] based on weakly nonlinear theory. Although in our experiment more modes were active than in the low-order model, it was confirmed that the geostrophic mode is balanced by the self-interactions of free modes and viscous damping.

Overall, the presented experimental setup mimics the classical precession experiments with only one rotating axis and the result suggests that the two systems do share many common characteristics. Nevertheless, we also observed some significant characteristics that differ from the observations in the precession setups. In our experiment, the nonlinear effects were more dominant for the saturation of the forced Kelvin mode and the geostrophic mode. Theoretical and experimental results in Lagrange *et al.* [64] indicated that nonlinear effects are independent of the Ekman numbers in the classical precession setup. However, our experiment suggested that the nonlinear effects are related to  $Ek$  with a scaling of roughly  $Ek^{-1/2}$ . The relation between the nonlinear effect and the Ekman numbers further influences the amplitude of the mean flow and the saturation of the forced Kelvin mode.

The present experiment has been conducted within a relatively narrow range of Ekman numbers, two fixed inclination angles and only a few fluid depths, which leaves plenty of space for further explorations to achieve a more plausible instability diagram. Limited by the current measurement techniques, an accurate observation of the velocity in a vertical plane is absent. It would be very helpful for understanding the mode structure in the vertical direction as well as confirming the mode interactions if the velocity field in a vertical plane could be measured. A modified bottom with an oblique upper side has been equipped in the rotating annulus. Due to the slope at the bottom of the tank, inertial beams have been

observed for particular filling depths and rotation rates. A further investigation is worthwhile to explore the influence of the inertial beams on the instabilities of the flow in the tilted rotating annulus with an oblique bottom.

In the second experiment, we studied the formation, reflection and collision of undular bores in a circular channel with a circumference of about 5 m. In the circular channel, two plane barriers were inserted into the channel, thus separated the circular channel into two arc sections. The water was filled into two sections with different surface levels. By abruptly removing one barrier or removing the two barriers simultaneously, a single undular bore or two identical counter-propagating undular bores were generated. The measurement of the bores was realized by measuring the surface profile using acoustic sensors. PIV has also been performed for a single bore case showing the velocity field of the fluid in a vertical plane in the streamwise direction.

Observations of the single bore experiment indicated that the average liquid depth and the initial height difference influence the propagation velocity, the wavelength and the front height in different ways. The wavelength mainly depends on the average depth and less on the initial height difference, whereas the front height depends mainly on the initial height difference. The propagation velocity, in contrast, depends on both the average liquid depth and the initial height difference. Due to the surface elevation in the hydraulic jumps, the bore propagates faster than  $\sqrt{gh}$ . For the propagation with a longer duration, a decay of the wave amplitude and the fluid velocity has been observed. The decay can be partly explained by the frictions using a simple Poiseuille flow model.

For the experiment with colliding bores, due to the circular geometry, we were able to use the symmetric and periodic condition to study the problem with multiple reflected colliding bores. The surface profiles are measured by multiple distant distributed acoustic sensors.

The experimental measurements were compared with numerical simulations performed by Sebastian Richter in the group of Prof. Bestehorn using the model reported in Bestehorn and Tyvand [13] and achieved an excellent agreement for both cases. The surface profiles measured in the experiment were perfectly reproduced in the numerical simulations, even after several collisions in the colliding cases. The fluid velocity in the wave crest measured by PIV also agreed with the numerics.

Moreover, we have performed an experiment for sloshing shallow water with a very small characteristic depth ratio between the average water depth and the channel length. The experiment has been conducted by adding a fixed barrier in

the longitudinally oscillating circular channel. With a wide range of the forcing frequency, four resonances were observed with frequencies matching the natural frequencies of the system. A simple comparison to the numerical simulations by Bouscasse *et al.* [19] showed a good agreement. Nevertheless, the nonlinear effects were not sufficiently strong for having a significant impact on the sloshing flow due to the small forcing amplitude.

Currently, numerical simulations for the sloshing shallow water experiment are still in progress based on the same code as used for the bores. For the next step of the investigation, the experimental result will be compared with the numerical simulation.

## References

- [1] H. N. Abramson. The dynamic behavior of liquids in moving containers. *NASA SP*, 106, 1966.
- [2] C. Aerts, J. Christensen-Dalsgaard, and D. W. Kurtz. *Asteroseismology*. Springer Science & Business Media, 2010.
- [3] G. B. Airy. Tides and waves. *encyclopaedia metropolitana (1817–1845)*. *Mixed Sciences*, edited by HJ Rose, 3, 1841.
- [4] T. Albrecht, H. M. Blackburn, J. M. Lopez, R. Manasseh, and P. Meunier. Triadic resonances in precessing rapidly rotating cylinder flows. *Journal of Fluid Mechanics*, 778:62–12, July 2015.
- [5] T. Albrecht, H. M. Blackburn, P. MEUNIER, R. Manasseh, and J. M. Lopez. Experimental and numerical investigation of a strongly-forced precessing cylinder flow. *International Journal of Heat and Fluid Flow*, 61(Part A):68–74, Oct. 2016.
- [6] K. D. Aldridge and A. Toomre. Axisymmetric inertial oscillations of a fluid in a rotating spherical container. *Journal of Fluid Mechanics*, 37(02):307, 1969.
- [7] A. Ali and H. Kalisch. A dispersive model for undular bores. *Analysis and Mathematical Physics*, 2(4):347–366, Oct. 2012.
- [8] A. B. Arons, A. P. Ingersoll, and T. Green. Experimentally observed instability of a laminar Ekman flow in a rotating basin. *Tellus*, 1961.
- [9] F. Auger, P. Flandrin, P. Gonçalvès, and O. Lemoine. Time-frequency toolbox. *CNRS France-Rice University*, 46, 1996.
- [10] Barcilon V. Stewartson Layers in Transient Rotating Fluid Flows. *Journal of Fluid Mechanics*, 33(04):815–825, 1968.
- [11] T. B. Benjamin. Internal waves of permanent form in fluids of great depth. *Journal of Fluid Mechanics*, 29(3):559–592, 1967.
- [12] M. V. Berry. Minimal analytical model for undular tidal bore profile; quantum and Hawking effect analogies. *New Journal of Physics*, 20(5):053066–12, May 2018.

- [13] M. Bestehorn and P. A. Tyvand. Merging and colliding bores. *Physics of Fluids*, 21(4):042107–12, Apr. 2009.
- [14] J. Boisson, D. Cébron, F. Moisy, and P. P. Cortet. Earth rotation prevents exact solid-body rotation of fluids in the laboratory. *Europhysics Letters*, 98(5):59002–7, June 2012.
- [15] I. D. Borcia, G. V. Abouzar, and U. Harlander. Inertial wave mode excitation in a rotating annulus with partially librating boundaries. *Fluid Dynamics Research*, 46(4):041423, Aug. 2014.
- [16] I. D. Borcia, R. Borcia, W. Xu, M. Bestehorn, S. Richter, and U. Harlander. Undular bores in a large circular channel. *European Journal of Mechanics B/Fluids*, 79:67–73, Nov. 2019.
- [17] I. D. Borcia and U. Harlander. Inertial waves in a rotating annulus with inclined inner cylinder: comparing the spectrum of wave attractor frequency bands and the eigenspectrum in the limit of zero inclination. *Theoretical and Computational Fluid Dynamics*, 27(3-4):397–413, July 2012.
- [18] D. Borrero-Echeverry, C. J. Crowley, and T. P. Riddick. Rheoscopic fluids in a post-Kalliroscope world. *Physics of Fluids*, 30(8):087103–6, Aug. 2018.
- [19] B. Bouscasse, M. Antuono, A. Colagrossi, and C. Lugni. Numerical and Experimental Investigation of Nonlinear Shallow Water Sloshing. *International Journal of Nonlinear Sciences and Numerical Simulation*, 14(2):1–17, Mar. 2013.
- [20] C. Brouzet, E. V. Ermanyuk, S. Joubaud, I. Sibgatullin, and T. Dauxois. Energy cascade in internal-wave attractors. *EPL (Europhysics Letters)*, 113(4):44001–7, Mar. 2016.
- [21] F. H. Busse. Shear Flow Instabilities in Rotating Systems. *Journal of Fluid Mechanics*, 33(3):577–589, 1968.
- [22] F. H. Busse. Zonal flow induced by longitudinal librations of a rotating cylindrical cavity. *Physica D: Nonlinear Phenomena*, 240(2):208–211, 2011.
- [23] H. Chanson. Undular Tidal Bores: Basic Theory and Free-Surface Characteristics. *Journal of Hydraulic Engineering-Asce*, 136(11):940–944, Nov. 2010.
- [24] H. Chanson. *Tidal bores, aegir, eagre, mascaret, pororoca: Theory and observations*. World Scientific, 2012.

- [25] H. Chanson and N. J. Docherty. Turbulent velocity measurements in open channel bores. *European Journal of Mechanics B/Fluids*, 32(C):52–58, Jan. 2012.
- [26] H. Chanson Miah. Physical modelling of the flow field in an undular tidal bore. *Journal of Hydraulic Research*, 43(3):234–244, Feb. 2005.
- [27] W. Chester. Resonant Oscillations of Water Waves. I. Theory. In *Proceedings of the Royal Society of London. Series A*, pages 5–22, July 1968.
- [28] W. Chester and J. A. Bones. Resonant Oscillations of Water Waves. II. Experiment. In *Proceedings of the Royal Society of London. Series A*, pages 23–39, July 1968.
- [29] C. Cierpka, R. Hain, and N. A. Buchmann. Flow visualization by mobile phone cameras. *Experiments in fluids*, 57(6):108–10, June 2016.
- [30] A. D. D. Craik. The Origins of Water Wave Theory. *Annual Review of Fluid Mechanics*, 36(1):1–28, Jan. 2004.
- [31] B. Cushman-Roisin and J.-M. Beckers. The Ekman Layer. In *Introduction to Geophysical Fluid Dynamics - Physical and Numerical Aspects*, pages 239–270. Elsevier, 2011.
- [32] L. David, L. Chatellier, D. Calluaud, Y. Jeon, G. Rousseaux, and L. Thomas. Tr-piv measurements in open channel flow for the analysis of undular tidal bores. In *17th International Symposium on Applications of Laser Techniques to Fluid Mechanics, Lisbon, Portugal*, pages 07–10. Citeseer, 2014.
- [33] C. Donnelly and H. Chanson. Environmental Impact of Undular Tidal Bores in Tropical Rivers. *Environmental Fluid Mechanics*, 5(5):481–494, Jan. 2005.
- [34] R. J. Donnelly. Taylor-Couette flow: the early days. *Phys Today*, 1991.
- [35] A. Dörnbrack and C. J. Nappo. A Note on the Application of Linear Wave Theory at a Critical Level. *Boundary-Layer Meteorology*, 82(3):399–416, 1997.
- [36] P. G. Drazin. *Introduction to Hydrodynamic Stability*. Cambridge University Press, July 2002.
- [37] C. Eloy, P. Le Gal, and S. Le Dizès. Elliptic and triangular instabilities in rotating cylinders. *Journal of Fluid Mechanics*, 476:357–388, Mar. 2003.

- [38] W. J. Emery and R. E. Thomson. *Data analysis methods in physical oceanography*. Elsevier Science. Elsevier Science, New York, 2001.
- [39] A. Esser and S. Grossmann. Analytic expression for Taylor–Couette stability boundary. *Physics of Fluids*, 8(7):1814–1819, 1996.
- [40] O. M. Faltinsen, O. F. Rognebakke, and A. N. Timokha. Transient and steady-state amplitudes of resonant three-dimensional sloshing in a square base tank with a finite fluid depth. *Physics of Fluids*, 18(1):012103–15, Jan. 2006.
- [41] O. M. Faltinsen and A. N. Timokha. Asymptotic modal approximation of nonlinear resonant sloshing in a rectangular tank with small fluid depth. *Journal of Fluid Mechanics*, 470(0):319–357, Nov. 2002.
- [42] S. Friedlander. *An Introduction to the Mathematical Theory of Geophysical Fluid Dynamics*. Elsevier, Jan. 1980.
- [43] Y. Fujino, B. M. Pacheco, P. Chaiseri, and L. M. Sun. Parametric Studies on Tuned Liquid Damper (TLD) Using Circular Containers by Free-Oscillation Experiments. *Doboku Gakkai Ronbunshu*, 1988(398):177–187, Oct. 1988.
- [44] I. Gavriluk, I. Lukovsky, Y. Trotsenko, and A. Timokha. Sloshing in a vertical circular cylindrical tank with an annular baffle. Part 1. Linear fundamental solutions. *Journal of Engineering Mathematics*, 54(1):71–88, Jan. 2006.
- [45] Y. Goda. *Random seas and design of maritime structures*. World scientific, 2010.
- [46] I. Grant. Particle image velocimetry: a review. *Proceedings of the Institution of Mechanical Engineers, Part C: Journal of Mechanical Engineering Science*, 211(1):55–76, 1997.
- [47] H. P. Greenspan. *The Theory of Rotating Fluids*. Cambridge, 1968.
- [48] M. Greshko. Watch a wall of water race up a river, 2017. <https://www.nationalgeographic.com/news/2017/10/tidal-bores-qiantang-china-rivers-environment-spdl/>, Last accessed on 2020-08-10.
- [49] G. W. Griffiths and W. E. Schiesser. Linear and nonlinear waves. *Scholarpedia*, 4(7):4308, 2009. revision #154041.



- [50] G. Handler, T. Tuvikene, D. Lorenz, R. Shobbrook, S. Saesen, J. Provencal, M. Pagani, B. Quint, M. Desmet, C. Sterken, et al. Asteroseismology in the young open cluster ngc 3293. *Communications in Asteroseismology*, 157:315–316, 2008.
- [51] F. M. Henderson. Open channel flow. Technical report, 1966.
- [52] J. Hérault, A. Giesecke, T. Gundrum, and F. Stefani. Instability of precession driven kelvin modes: Evidence of a detuning effect. *Phys. Rev. Fluids*, 4:033901, Mar 2019.
- [53] M. Hoff, U. Harlander, and C. Egbers. Experimental survey of linear and nonlinear inertial waves and wave instabilities in a spherical shell. *Journal of Fluid Mechanics*, 789:589–616, Jan. 2016.
- [54] M. Hoff, U. Harlander, and S. A. Triana. Study of turbulence and interacting inertial modes in a differentially rotating spherical shell experiment. *Physical Review Fluids*, 1(4):043701–17, Aug. 2016.
- [55] J. Huang, C.-h. Pan, C.-p. Kuang, Z. Jian, and C. Gang. Experimental hydrodynamic study of the qiantang river tidal bore. *Journal of Hydrodynamics, Ser. B*, 25(3):481–490, 2013.
- [56] G. Iooss and P. Kirrmann. Capillary gravity waves on the free surface of an inviscid fluid of infinite depth. Existence of solitary waves. *Archive for Rational Mechanics and Analysis*, 136(1):1–19, Dec. 1996.
- [57] R. D. Keane and R. J. Adrian. Optimization of particle image velocimeters. i. double pulsed systems. *Measurement Science and Technology*, 1(11):1202–1215, nov 1990.
- [58] C. E. Keevil, H. Chanson, and D. Reungoat. Fluid flow and sediment entrainment in the Garonne River bore and tidal bore collision. *Earth Surface Processes and Landforms*, 40(12):1574–1586, July 2015.
- [59] R. R. Kerswell. Secondary instabilities in rapidly rotating fluids: inertial wave breakdown. *Journal of Fluid Mechanics*, 382:283–306, 1999.
- [60] M. Klein, T. Seelig, M. V. Kurgansky, A. Ghasemi V, I. D. Borcia, A. Will, E. Schaller, C. Egbers, and U. Harlander. Inertial wave excitation and focusing in a liquid bounded by a frustum and a cylinder. *Journal of Fluid Mechanics*, 751:255–297, July 2014.

- [61] J. J. Koblitz. Azimuthal flow associated with inertial wave resonance in a precessing cylinder. *Journal of Fluid Mechanics*, 319(-1):387–406, July 1996.
- [62] M. V. Kurgansky, T. Seelig, M. Klein, A. Will, and U. Harlander. Mean flow generation due to longitudinal librations of sidewalls of a rotating annulus. *Geophysical & Astrophysical Fluid Dynamics*, 46:1–21, Jan. 2020.
- [63] R. Lagrange, C. Eloy, F. Nadal, and P. Meunier. Instability of a fluid inside a precessing cylinder. *Physics of Fluids*, 20(8):081701–4, Aug. 2008.
- [64] R. Lagrange, P. Meunier, F. Nadal, and C. Eloy. Precessional instability of a fluid cylinder. *Journal of Fluid Mechanics*, 666:104–145, Jan. 2011.
- [65] L. Landau and E. Lifshitz. *Fluid Mechanics: Course of Theoretical Physics. Vol. 6*. Pergamon Press, 1987.
- [66] M. Landrini and P. Tyvand. Generation of water waves and bores by impulsive bottom flux. In *Practical Asymptotics*, pages 131–170. Springer, 2001.
- [67] M. Le Bars, D. Cébron, and P. Le Gal. Flows Driven by Libration, Precession, and Tides. *Annual Review of Fluid Mechanics*, 47(1):163–193, Jan. 2015.
- [68] M. Le Bars, S. Le Dizès, and P. Le Gal. Coriolis effects on the elliptical instability in cylindrical and spherical rotating containers. *Journal of Fluid Mechanics*, 585:323, Aug. 2007.
- [69] T. G. Lepelletier and F. Raichlen. Nonlinear Oscillations in Rectangular Tanks. *Journal of Engineering Mechanics*, 114(1):1–23, Jan. 1988.
- [70] Y. Li, D.-Z. Pan, H. Chanson, and C.-h. Pan. Real-time characteristics of tidal bore propagation in the Qiantang River Estuary, China, recorded by marine radar. *Continental Shelf Research*, 180:48–58, June 2019.
- [71] C. Lin, M.-J. Kao, J.-M. Yuan, R. V. Raikar, W.-Y. Wong, J. Yang, and R.-Y. Yang. Features of the flow velocity and pressure gradient of an undular bore on a horizontal bed. *Physics of Fluids*, pages 1–28, Apr. 2020.
- [72] Y. Lin, J. Noir, and A. Jackson. Experimental study of fluid flows in a precessing cylindrical annulus. *Physics of Fluids*, 26(4):046604–21, Apr. 2014.
- [73] J. M. Lopez and F. Marques. Nonlinear and detuning effects of the nutation angle in precessionally forced rotating cylinder flow. *Physical Review Fluids*, 1(2):023602, June 2016.

- [74] J. M. Lopez and F. Marques. Rapidly rotating precessing cylinder flows: forced triadic resonances. *Journal of Fluid Mechanics*, 839:239–270, Jan. 2018.
- [75] P. Lubin, H. Chanson, and S. Glockner. Large Eddy Simulation of turbulence generated by a weak breaking tidal bore. *Environmental Fluid Mechanics*, 10(5):587–602, Jan. 2010.
- [76] W. V. R. Malkus. An experimental study of global instabilities due to the tidal (elliptical) distortion of a rotating elastic cylinder. *Geophysical & Astrophysical Fluid Dynamics*, 48(1-3):123–134, 1989.
- [77] W. V. R. Malkus and F. A. Waleffe. Transition from order to disorder in elliptical flow: A direct path to shear flow turbulence. In A. V. Johansson and P. H. Alfredsson, editors, *Advances in Turbulence 3*, pages 197–203, Berlin, Heidelberg, 1991. Springer Berlin Heidelberg.
- [78] R. Manasseh. Breakdown regimes of inertia waves in a precessing cylinder. *Journal of Fluid Mechanics*, 243(-1):261, 1992.
- [79] C. Marks, R. Sondergaard, M. Wolff, and J. Estevadeordal. PIV Investigation of a Highly-Loaded LPT Blade Using a Curved Laser Sheet. In *47th AIAA Aerospace Sciences Meeting including The New Horizons Forum and Aerospace Exposition*, page n10, Reston, Virginia, June 2009. American Institute of Aeronautics and Astronautics.
- [80] F. Marques and J. M. Lopez. Precession of a rapidly rotating cylinder flow: traverse through resonance. *Journal of Fluid Mechanics*, 782:63–98, Oct. 2015.
- [81] K. Martins, P. Bonneton, F. Frappart, G. Detandt, N. Bonneton, and C. Blenkinsopp. High Frequency Field Measurements of an Undular Bore Using a 2D LiDAR Scanner. *Remote Sensing*, 9(5):462–14, May 2017.
- [82] P. Matisse. History of kalliroscope. <http://www.paulmatisse.com/history>, Last accessed on 2020-08-10.
- [83] P. Matisse and M. Gorman. Neutrally buoyant anisotropic particles for flow visualization. *Physics of Fluids*, 27(4):759–3, 1984.
- [84] A. D. McEwan. Inertial oscillations in a rotating fluid cylinder. *Journal of Fluid Mechanics*, 40(03):603, 1970.
- [85] A. D. McEwan. Degeneration of resonantly-excited standing internal gravity waves. *Journal of Fluid Mechanics*, 50(03):431, 1971.

- [86] L. Messio, C. Morize, M. Rabaud, and F. Moisy. Experimental observation using particle image velocimetry of inertial waves in a rotating fluid. *Experiments in fluids*, 44(4):519–528, Oct. 2007.
- [87] P. Meunier. Soft Mixer: toward geoinspired bioreactors. *Soft Mixer: toward geoinspired bioreactors (submitted to J. Fluid Mech.)*, Mar. 2020.
- [88] P. Meunier, C. Eloy, R. Lagrange, and F. Nadal. A rotating fluid cylinder subject to weak precession. *Journal of Fluid Mechanics*, 599:357, Mar. 2008.
- [89] R. A. Meyers. *Encyclopedia of complexity and systems science*. Springer, 2009.
- [90] D. Mitrović, M. Zeppelzauer, and C. Breiteneder. Chapter 3 - features for content-based audio retrieval. In *Advances in Computers: Improving the Web*, volume 78 of *Advances in Computers*, pages 71 – 150. Elsevier, 2010.
- [91] J. Mougel, D. Fabre, and L. Lacaze. Waves in Newton’s bucket. *Journal of Fluid Mechanics*, 783:211–250, Oct. 2015.
- [92] C. L. Nikias and M. R. Raghuveer. Bispectrum Estimation - a Digital Signal-Processing Framework. *Proceedings of the IEEE*, 75(7):869–891, July 1987.
- [93] H. Ockendon, J. R. Ockendon, and A. D. Johnson. Resonant sloshing in shallow water. *Journal of Fluid Mechanics*, 167(-1):465–15, Apr. 1986.
- [94] J. R. Ockendon and H. Ockendon. Resonant surface waves. *Journal of Fluid Mechanics*, 59:397–413, 1973.
- [95] C.-h. Pan, B.-Y. Lin, and X.-Z. Mao. Case study: Numerical modeling of the tidal bore on the Qiantang River, China. *Journal of Hydraulic Engineering-Asce*, 133(2):130–138, Feb. 2007.
- [96] J. S. Park and J. M. Hyun. Review on open-problems of spin-up flow of an incompressible fluid. *Journal of Mechanical Science and Technology*, 22(4):780–787, May 2008.
- [97] J. Pedlosky. *Waves in the Ocean and Atmosphere*. Introduction to Wave Dynamics. Springer Science & Business Media, Apr. 2013.
- [98] D. H. Peregrine. Calculations of the development of an undular bore. *Journal of Fluid Mechanics*, 25(2):321–330, 1966.

- [99] M. Raffel, C. E. Willert, F. Scarano, C. J. Kähler, S. T. Wereley, and J. Kompenhans. *Particle Image Velocimetry. A Practical Guide*. Springer, Cham, Apr. 2018.
- [100] C. Rodda. *Gravity wave emission from jet systems in the differentially heated rotating annulus experiment*. Cuvillier Verlag, 2019.
- [101] C. Rodda, I. D. Borcia, P. Le Gal, M. Vincze, and U. Harlander. Baroclinic, Kelvin and inertia-gravity waves in the barostat instability experiment. *Geophysical & Astrophysical Fluid Dynamics*, 112(3):175–206, Apr. 2018.
- [102] G. Rousseaux, J.-M. Mougenot, L. Chatellier, L. David, and D. Callaud. A novel method to generate tidal-like bores in the laboratory. *European Journal of Mechanics-B/Fluids*, 55:31–38, 2016.
- [103] F. Schultz-Grunow. *Theoretische und experimentelle Beiträge zur Grenzschichtströmung*, volume 684. Westdeutscher Verlag, 1956.
- [104] T. Seelig. *Inertial wave propagation, focusing and mean flow excitation: theory and experiments*. PhD thesis, Cuvillier Verlag Göttingen, Sept. 2014.
- [105] M. Selmi and T. Herbert. Resonance phenomena in viscous fluids inside partially filled spinning and nutating cylinders. *Physics of Fluids*, 7(1):108–120, Jan. 1995.
- [106] E. Sozer and M. Greenberg. The time-dependent free surface flow induced by a submerged line source or sink. *Journal of Fluid Mechanics*, 284:225–237, 1995.
- [107] M. D. Su, X. Xu, J. L. Zhu, and Y. C. Hon. Numerical simulation of tidal bore in Hangzhou Gulf and Qiantangjiang. *International Journal for Numerical Methods in Fluids*, 36(2):205–247, 2001.
- [108] J. K. Sveen. An introduction to matpiv v. 1.6.1. *Preprint series. Mechanics and Applied Mathematics available: <http://urn.nb.no/URN:NBN:no-27806>*, 2004.
- [109] J. K. Sveen and E. A. Cowen. Qualitative Imaging Techniques and Their Application to Wavy Flows. In *PIV and Water Waves*, pages 1–49. WORLD SCIENTIFIC, Oct. 2004.
- [110] R. Thompson. Diurnal tides and shear instabilities in a rotating cylinder. *Journal of Fluid Mechanics*, 40(4):737–751, Mar. 1970.

- [111] W. Thomson. XXIV. Vibrations of a columnar vortex. *The London, Edinburgh, and Dublin Philosophical Magazine and Journal of Science*, 10(61):155–168, 1880.
- [112] A. Treske. Undular bores (favre-waves) in open channels - Experimental studies. *Journal of Hydraulic Research*, 32(3):355–370, Jan. 1994.
- [113] G. K. Vallis. *Atmospheric and Oceanic Fluid Dynamics. Fundamentals and Large-scale Circulation*. Cambridge University Press, Nov. 2006.
- [114] M. Velarde and A. Nepomnyashchy. Solitons in viscous flows. In *Dissipative Solitons: From Optics to Biology and Medicine*, pages 1–21. Springer, 2008.
- [115] P. D. Weidman. Measurement techniques in laboratory rotating flows. In *Advances in fluid mechanics measurements*, pages 401–534. Springer, 1989.
- [116] J. E. Wesfreid. Scientific biography of henri Bénard (1874–1939). In *Dynamics of Spatio-Temporal Cellular Structures*, pages 9–37. Springer, 2006.
- [117] D. S. Wilks. *Statistical Methods in the Atmospheric Sciences*. Academic Press, 2011.
- [118] W. Xu and U. Harlander. Inertial mode interactions in a rotating tilted cylindrical annulus with free surface. pages 1–21, Sept. 2020.
- [119] K. Zhang and X. Liao. *Theory and Modeling of Rotating Fluids. Convection, Inertial Waves and Precession*. Cambridge University Press, Cambridge, 2017.

## Acknowledgement

Throughout the writing of this dissertation, I have received a great deal of support and assistance.

First of all, I would like to express my sincere gratitude to my supervisor, Prof. Uwe Harlander, for the continuous support of my PhD study and related research. His precious guidance helped me in all the time of research and writing of this thesis. I appreciate all his patience, insightful feedback, and immense knowledge for making me really enjoying my PhD time. It has been an honor to be his PhD student.

My sincere thanks also go to Ion Dan Borgia and Rodica Borgia, who provided me the opportunity to join the project for the research about undular bores, which broadened my research field and enriched my scientific experience. It was a pleasant time working with them and the research has been an important part of the thesis.

I would like to thank Patrice Meunier and Patrice Le Gal for fruitful scientific discussions.

It has been a great time for working in the Department of Aerodynamics and Fluid Mechanics of BTU Cottbus-Senftenberg and I would like to thank all my colleagues. Torsten Seelig provided precious support and helped me quickly learn the skills for the experiment at the beginning of my PhD. Costanza Rodda is a great officemate and friend and provided me a lot of help. I had a wonderful time working with her. I appreciate the technical supports from Ludwig Stapelfeld, Robin Stöbel, Vilko Ruoff and Heinz-Jörg Wengler.

I would like to thank Costanza Rodda, Peter Szabo, Ion Dan Borgia and Rodica Borgia for reading the proof and giving useful corrections.

I gratefully acknowledge the funding sources that made my Ph.D. work possible. I was funded by the Graduate Research School (GRS) of Brandenburg University of Technology Cottbus-Senftenberg as part of the cluster "Stochastic methods for fluid flow and transport processes". My work is also financially supported by the DFG program HA 2932/8-2.

Last but not the least, I would like to thank my parents and my wife for supporting me spiritually throughout writing this thesis and my life in general.

